2010

LAMINAR-TURBULENT TRANSITION FOR ATTACHED AND SEPARATED FLOW

Qian Zhang

University of Kentucky, zqian@engr.uky.edu

Click here to let us know how access to this document benefits you.

ABSTRACT OF DISSERTATION

Qian Zhang

The Graduate School

University of Kentucky

2010

LAMINAR-TURBULENT TRANSITION FOR
ATTACHED AND SEPARATED FLOW

_____

ABSTRACT OF DISSERTATION
_____

A dissertation submitted in partial fulfillment of the
requirements for the degree of Doctor of Philosophy in the
College of Engineering
at the University of Kentucky

By
Qian Zhang

Lexington, Kentucky

Director: Dr. Vincent R. Capece, Associate Professor of Mechanical Engineering

Paducah, Kentucky

2010

ABSTRACT OF DISSERTATION

LAMINAR-TURBULENT TRANSITION
FOR ATTACHED AND SEPARATED FLOW

A major challenge in the design of turbomachinery components for aircraft gas turbine engines is high cycle fatigue failures due to flutter. Of particular concern is the subsonic/transonic stall flutter boundary which occurs at part speed near the stall line. At these operating conditions the incidence angle is large and the relative Mach number is high subsonic or transonic. Viscous effects dominate for high incidence angles.

In order to predict the flutter phenomena, accurate calculation of the steady and unsteady aerodynamic loading on the turbomachinery airfoils is necessary. The development of unsteady aerodynamic models to predict the unsteady forces and moments acting on turbomachine airfoils is an area of fundamental research interest. Unsteady Reynolds Averaged Navier-Stokes (RANS) models have been developed to accurately account for viscous effects. For these Reynolds averaged equations turbulence models are needed for the Reynolds stress terms. A transition model is also necessary. The transition onset location is determined by a transition onset model or specified at the suction peak. Usually algebraic, one or two-equation or Reynolds stress turbulence models are used. Since the Reynolds numbers in turbomachinery are large enough to guarantee the flow is turbulent, suitable transition and turbulence models are crucial for accurate prediction of steady and unsteady separated flow.

The viscous flow solution of compressor airfoils at off-design conditions is challenging due to flow separation and transition to turbulent flow within separation bubbles. Additional complexity arises when the airfoils are vibrating as is encountered in stall flutter. In this investigation calculations are made of a transonic compressor airfoil in steady flow and with the airfoils oscillating in a pitching motion about the mid-chord at 0° and 10° of chordal incidence angle, and correlated with experiments conducted in the NASA GRC Transonic Flutter Cascade. To model the influence of flow transition on the steady and unsteady aerodynamic flow characteristics, the Solomon, Walker, and Gostelow (SWG) transition model is utilized. The one-equation Spalart-Allmaras model is used to model turbulence. Different transition onset models including fixed onset are implemented and compared for the two incidence angle cases. At each incidence angle, the computational model is compared to the experimental data

for the steady flow case and also for pitching oscillation at a reduced frequency of 0.4. The 10° incidence angle case has flow separation over front 40% of the airfoil chord. The operating conditions considered are an inlet Mach number of 0.5 and a Reynolds number of 0.9 Million.

KEYWORDS: Flutter, High Cycle Fatigue, Turbulence model, Transition model, Computational Fluid Dynamics

<div style="margin-left: 40%;">

Qian Zhang

——————————————————

Student's Signature

May 7, 2010

——————————————————

Date

</div>

LAMINAR-TURBULENT TRANSITION
FOR ATTACHED AND SEPARATED FLOW

By

Qian Zhang

Dr. Vincent R. Capece
Director of Dissertation

Dr. James M. McDonough
Director of Graduate Studies

May 7, 2010
Date

RULES FOR THE USE OF DISSERTATIONS

Unpublished dissertations submitted for the Doctor's degree and deposited in the University of Kentucky Library are as a rule open for inspection, but are to be used only with due regard to the rights of the authors. Bibliographical references may be noted, but quotations or summaries of parts may be published only with the permission of the author, and with the usual scholarly acknowledgements.

Extensive copying and publication of the thesis in whole or in part also requires the consent of the Dean of the Graduate School of the University of Kentucky.

A library that borrows this thesis for use by its patrons is expected to secure the signature of each user.

Name   Date

_____

_____

_____

_____

_____

_____

_____

_____

_____

_____

DISSERTATION

Qian Zhang

The Graduate School

University of Kentucky

2010

LAMINAR-TURBULENT TRANSITION FOR
ATTACHED AND SEPARATED FLOW

_____

DISSERTATION

_____

A dissertation submitted in partial fulfillment of the
requirements for the degree of Doctor of Philosophy in the
College of Engineering
at the University of Kentucky

By
Qian Zhang

Lexington, Kentucky

Director: Dr. Vincent R. Capece, Associate Professor of Mechanical Engineering

Paducah, Kentucky

2010

I dedicate my dissertation to my loving parents,
Zugong Zhang and Xiuyan Li,
my dear wife, Fengjuan Wang,
and my dearest daughter, Grace J. Zhang.
Your love and encouragement are the greatest impetus for me to go ahead.

ACKNOWLEDGEMENTS

TABLE OF CONTENTS

LIST OF TABLES

LIST OF FIGURES

LIST OF SYMBOLS

C Blade chord

C/S Cascade solidity

C_f Skin friction coefficient

C_M Moment coefficient

C_L Lift coefficient

C_p First harmonic pressure coefficient, $P_1/\left(\rho_{in}V_{in}{}^2\alpha'_1\right)$

$\overline{C}_p$ Steady pressure coefficient, $\left(P-P_{in}\right)/\left(0.5\rho_{in}V_{in}{}^2\right)$

ΔC_p^I Imaginary part of pressure difference coefficient

C_W Work coefficient

f Blade oscillation frequency

h Blade span

k Reduced frequency, $\omega C/2V_{in}$

M Inlet Mach number or moment

$\overline{M},M_R,M_I$ Moment amplitude, real part, imaginary part

P Airfoil steady surface pressure

P_1 First harmonic surface pressure

P_{in} Cascade steady inlet pressure

P_{exit} Cascade steady exit pressure

Re_C Chordal Reynolds number, $\rho_{in}V_{in}C/\mu_{in}$

Re_{ref}	Reference Reynolds number, inlet Reynolds number
Re_x	Reynolds number at x location
S	Spacing between airfoils
u, v	x, y Cartesian velocity components
u^+	Non-dimensional tangential velocity to the wall
y^+	Non-dimensional normal distance to the wall
u_{tang}	Tangential velocity along the streamwise direction
V_{in}	Inlet velocity
$\tilde{w}$	Work impulse
W	Work-per-cycle
x	Coordinate along the chord
$x_{t,ss}$	Transition onset location on suction surface
$\alpha, \bar{\alpha}$	Incidence angle and incidence angle amplitude
α_1'	First harmonic of blade pitching motion
γ	Specific heat ratio
η	Blade to blade direction, computational coordinates
Θ	Stagger angle
μ_{in}	Cascade inlet dynamic viscosity
μ_w	Surface dynamic
ν_w	Surface kinematic viscosity, μ_w / ρ_w

ξ	Streamwise direction, computational coordinates
ρ_{in}	Cascade inlet density
ρ_w	Surface density
σ	Interblade phase angle
τ_w	Surface skin friction, $\mu \dfrac{\partial u_{\tan g}}{\partial y}\bigg|_w$
ω	Frequency of oscillation in $^{rad}/_{sec}$

Chapter 1   Introduction

1.1   Background

After more than a hundred years of research, fluid dynamic problems related to instability, transition and intermittency are still poorly understood. It is well known that the boundary layer that grows on the surface of any body is at first laminar. As the flow proceeds downstream from the leading edge, the laminar boundary layer is replaced by a more rapidly growing and thicker turbulent layer. In between, there is a region of transition from one to the other.

The stability of laminar shear flows and the transition to turbulence has fundamental importance to the study of fluid motions. It is known that, in general, transition can be induced by the following factors: surface roughness, free stream turbulence, surface curvature, pressure gradient, surface temperature, Reynolds number, Mach number, acoustic radiation, and injection or suction of fluid at the wall. Because there are so many complex factors that can affect transition, no satisfactory theory for the transition process has been found so far, and the origin of turbulence still remains an unsolved problem in fluid mechanics.

A major challenge in the design of turbomachinery components for aircraft gas turbine engines is high cycle fatigue failures due to flutter. Of particular concern is the subsonic/transonic stall flutter boundary which occurs at part speed near the stall line (Figure 1.1). At these operating conditions the incidence angle is large and the relative Mach number is high subsonic or transonic. Viscous effects dominate for these operating conditions.

For flows in turbomachinery, flow field can be determined fundamentally through direct numerical simulation (DNS), large eddy simulation (LES) or Reynolds Averaged Navier-Stokes (RANS) solvers.   DNS and LES are currently not practical for realistic

Reynolds numbers at this time due to their large computational costs. Thus, for design purposes it is more feasible to combine existing RANS solvers to solve the engineering problems.

In order to predict the flutter phenomena, accurate calculation of the steady and unsteady aerodynamic loading on the turbomachinery airfoils is necessary. A transition model is also necessary. The transition onset location is determined by a transition onset model or specified at the suction peak. Usually algebraic, one or two-equation or Reynolds stress turbulence models are used. Since the Reynolds numbers in turbomachinery are large enough to guarantee the flow is turbulent, suitable transition and turbulence models are crucial for accurate prediction of steady and unsteady separated flow.

The viscous flow solution of compressor airfoils at off-design conditions is challenging due to flow separation and transition to turbulent flow within separation bubbles. Additional complexity arises when the airfoils are vibrating as is encountered in stall flutter.

Figure 1.1 Schematic compressor map showing possible flutter regions

1.2 Literature review

Emmons[1] was the first to propose a description of the transition region in a

boundary layer, which states that transition occurs through "islands" of turbulence surrounded by laminar flow, or spots. Experiments of Mitchner[2], Schubauer and Klebanoff[3], Tani and Hama[4], Hama et al.[5] and others have shown that the transition phenomenon in a boundary layer is characterized by the intermittent appearance of turbulent spots, which move downstream with the fluid. The mechanics of spot generation and growth is still not completely clear. Experimental observations with flow visualization techniques suggest that the amplification of Tollmein-Schlichting waves becomes associated at some stage with the concentration of vorticity along discrete lines, and then subsequently distort into vortex loops in the boundary layer. The vortex loops go through a process of distortion and extension finally resulting in the creation of 'spots' of turbulence. Once those spots are created, they are swept along with the mean flow, growing laterally as well as axially with laminar flow in their trail. The spots originate in a random fashion and increasingly overlap as they enlarge during their spreading downstream, finally covering the entire plate and ending in fully turbulent motion. The spots passage on the surface results in alternating laminar and turbulent flow.

The key variable during transition is the 'intermittency' factor γ_I, which may be defined as the fraction of time that the flow is turbulent at any point. Flow at zero pressure gradient over a flat plate is the classical case most studied in detail. For this case when transition occurs naturally or due to a disturbing media, it causes the spots to appear at some distance downstream. The spots grow in a mostly linear manner, sweeping 'turbulent wedges' on the plate. During the initial period, the spot growth is non-linear, and envelopes of spot growth show a characteristic curved shape. Experimental studies by Mitchner [2], Schubauer & Klebanoff[3] demonstrate that the existence of turbulent spots in boundary layer flow has a fundamental role in the mechanics of boundary layer transition and may also play a part in the breakdown of laminar motion in general.

Emmons[1] describes the transition from laminar to turbulent as follows: "Viscosity builds a laminar boundary layer completely covering the given body (this may

include regions of separation). This boundary layer is disturbed (in space, time, frequency, and amplitude) by random motions carried in by the fluid from the free stream, carried in through the fluid as sound waves, produced in the boundary layer by surface irregularities, or produced by the vibrations of the plate. Each of these disturbances amplifies or damps as it moves along the surface. The sum total of these disturbances is to be visualized as disturbing the calm of the laminar boundary layer in the same way as random waves disturb the calm of the sea."

Narasimha[6] reviewed the transition process and turbulent spots in a variety of flows and showed that the most appropriate non-dimensional breakdown rate parameter (spot formation rate) is of the form $N = n\sigma\theta_t^3 / \nu$.

Chen and Thyson[7] found that the key factor to control flow transition in the transition zone appears to be the spot formation rate. Moreover, the spot formation rate depends not only on the transition Reynolds number but also on the Mach number. They used the turbulent spot theory of Emmons[1] to develop a transition flow model which purported to allow for the influence of pressure gradient on the intermittency distribution and transition length.

The Chen and Thyson[7] model has been used by Ekaterinaris et al[8] and van Dyken et al[9] in a thin layer RANS code for transition calculations for steady and oscillating airfoils. An adjustment of the Chen-Thyson transition constant was necessary to get better correlation with experimental data since the basis of this constant was on pressure gradient free flow. Computations were performed on separation bubbles for a NACA0012 airfoil.

Solomon, Walker, and Gostelow[10] developed a new method for calculating intermittency in transitional boundary layers with changing pressure gradients. The new model (SWG) calculated the transition length as a function of pressure gradient and free-stream turbulence level. It showed that the local pressure gradient parameter has a significant effect on turbulent spot spreading angles and propagation velocities (and

4

hence transition length). This new method continuously adjusts the spot growth parameters in response to changes in the local pressure gradient and seems to be less sensitive to errors in predicting the start of the transition zone. The transitional flow length has been successfully demonstrated for typical turbine airfoil test cases.

Sanz and Platzer[11] implemented the SWG transition model into an upwind-biased Navier-Stokes code to simulate laminar-turbulent transition in the boundary layer. Although the SWG model was developed for transition in attached flow, it was incorporated in their Navier-Stokes code to predict laminar separation bubbles. Varying both spot generation rate and transition onset can give results ranging from no separation to bubbles of about 5% chord length to full stall. The transition onset location and spot generation rate must be provided by detailed experimental measurements of the transition process inside the separation bubbles. This work only has limited unsteady data, which compare the lift loop of a fully-turbulent with a transition solution.

In Sanz and Platzer's[12] work, five different transition models (Solomon, Walker and Gostelow[10], Abu-Ghannam and Shaw[13], Mayle[14], Calvert[15], Choi and Kang[16]) were incorporated into a thin-layer Navier-Stokes code. It was found that none of the models predicted the measured bubbles very well, although most of them gave reasonable results as long as transition is predicted to occur within the bubble. Only the Abu-Ghannam and Shaw model was inferior due to the excessively long transition zone predicted by this model. It was also found that the location of transition onset is a key parameter. If transition onset is predicted to occur too far downstream, the computed flow field exhibits periodic vortex shedding. This work emphasized steady flow only.

Sanz and Platzer[17] showed that besides the transition model, other parameters like the discretization scheme of the turbulence model or the flow solver have a comparably large influence on the results. This work focused on the different flow solvers and turbulence models combined with either SWG (Solomon et al.[10]) or SIM (Simple) transition model in which transition is modeled by setting the transition onset and the

transition length and assuming an exponential function according to Narasimha.[6] It was shown that most transition models derived for attached flows can only be used in a limited range for separated-flow transition because they tend to become unstable. The computation of long laminar separation bubbles tends to lead to oscillations over time. Constant time stepping should be applied if the solution oscillates over time. If the laminar or transitional zone is set too long, the solution shows very strong oscillations caused by shedding and reforming of the separation bubbles.

Thermann, Müller, and Niehuis[18] studied two cases by applying the transition criterion of Mayle[14] and the transition model of Walker et al.[19] for separated-flow transition, and also the criterion of Sieger et al.[20] and the model of Solomon et al.[10] for attached flow. The results show that the shock-induced laminar separation bubble on the suction side and the resulting pressure plateau can be predicted with the transitional computation. Although the combined method shows better results, it is still not good when compared with the experimental data. The boundary layer development can be improved when applying correlation-based transition models. This work focused on the separated steady flow transition.

Suzen et al.[21] developed a transition model by combining the models of Steelant and Dick[22] and Cho and Chung.[23] It solved a transport equation for the intermittency factor to predict the transitional boundary layer flow under low-pressure turbine airfoil conditions. Prediction compared with experimental data of a separated and transitional boundary layer under low pressure turbine airfoil conditions involves two different Reynolds numbers, Re=300,000 and Re=50,000 and two freestream turbulence intensities, $Tu = 7\%$ and $Tu = 0.2\%$ (Hultgren and Volino[24], Tu stands for Free Stream Turbulence Intensity). The new transport model not only can reproduce the experimentally observed streamwise variation of the intermittency in the transition zone, but also provides a realistic cross-stream variation of the intermittency profile. Detailed comparisons with experiments are made for pressure coefficients, velocity, intermittency and turbulent

6

kinetic energy profiles. Overall, good agreement with the experimental data is obtained. Separated and transitional boundary layer for steady flow was predicted in this work.

Since the majority of transition models depend on boundary layer parameters, Menter et al.[25] proposed a new method, which combines correlation-based methods with general transport equations that depend on local variables. The model was based on a transport equation for a generalized intermittency variable and was formulated without the use of integral boundary layer parameters (e.g. momentum thickness, boundary layer thickness). It was coupled with the SST turbulence model and tested against a series of two dimensional test cases. The results show a fairly good agreement with the experimental data. The formulation was a first step towards a general framework for correlation-based transition models. Additional calibration is required for flows with pressure gradients.

Menter et al.[26] developed a new correlation-based transition model based strictly on local variables. It is compatible with modern CFD approaches such as unstructured grids and massive parallel execution. The model is based on two transport equations, one for intermittency, and one for the transition onset criteria in terms of momentum thickness Reynolds number. A significant number of test cases have been used to validate the transition model for turbomachinery and aerodynamic applications. The authors believe that the current formulation is a significant step forward in engineering transition modeling, as it allows the combination of correlation-based transition models with general purpose CFD codes.

De Palma[27] provided an accurate and efficient methodology for computing turbulent and transition flows by solving the compressible RANS equations with an EASM (Explicit Algebraic Stress Model) and k-ω turbulence closure. Furthermore, the transition model of Mayle for separated flow was combined with this turbulence model. It was found that when the k-ω EASM without transition model was employed, the separation bubble could be predicted only for low inlet turbulence intensities ($Tu < 1\%$).

When combined with the Mayle's transition model, the bubble was detected in all of the investigated ranges of the inlet turbulence intensities (0.8%<Tu<7.1%). Better agreement between the numerical and the experimental data was found for low-medium levels of Tu.

Langtry and Sjolander[28] developed a new transition model to predict the onset of transition under the influence of freestream turbulence intensity, pressure gradient and flow separation. The model is based on Van Driest and Blumer's concept of vorticity Reynolds number and has been calibrated for use with the Menter SST turbulence model. In all test cases, the agreement with experiment was good and the model appears to be as accurate at predicting the onset of transition as the available empirical correlations. Of particular note was the ability of the model to predict the combined effect of freestream turbulence intensity and Reynolds number on the reattachment point of a separation bubble.

Recently Whitlow et al.[29] used a three dimensional RANS code and a two dimensional RANS code (NSTRANS) with the Solomon et al[10] transition model to predict the flow for the NASA-GRC Transonic Flutter Cascade (TFC) airfoil. Steady flow computations were performed for both the low and large incidence angle cases for which surface pressure measurements are available. Distinct leading edge separation bubbles were predicted for each incidence angle. In particular, for the large incidence case, improved correlation with the measurements was exhibited compared to the fully turbulent calculations. Only fixed transition onset model was considered in this work.

1.3 Objectives

The objective of this research is to investigate the influence of transition on a transonic compressor airfoil by solving the compressible RANS equations coupled with SWG transition model and Spalart-Allmaras turbulence model. Also, the effects of different transition onset models are investigated. Transition predictions of SWG model for an inlet Mach number of 0.5 are compared with the experimental data for attached

and separate flow condition. The NASA-GRC-TFC airfoil is used in this research effort.

Unsteady pressure distribution prediction of the NASA-GRC TFC are also performed on NASA GRC Transonic Flutter Cascade to quantify the influence of transition for an inlet Mach number of 0.5 with reduced frequency of 0.4. The influence of transition onset models on the unsteady pressure distribution and work impulse are investigated.   The Reynolds number for each of the cases was 0.9 Million.

In order to conduct the computations above, the one-equation Spallart-Allmaras turbulence model and Solomon, Walker and Ghostlow transition model are implemented into the NPHASE code. Also, various transition onset models are incorporated with the SWG transition model to investigate the effect of the transition onset location in the transitional flow calculations.

Chapter 2   Airfoil Geometries and Grid Generation

2.1   NASA/P&W Airfoil Geometry

The experimental data used in this investigation were generated in the NASA Glenn Research Center Transonic Flutter Cascade (TFC). In this facility an exhaust system drew atmospheric air through honeycomb into a smoothly contracting inlet section; test section Mach numbers up to 1.15 were possible.   Downstream of the inlet was a rectangular duct that contained the nine airfoil test section.   Adjustable tailboards downstream of the test section were used to match the cascade exit flow angle. This facility has the unique capability of oscillating the nine airfoils simultaneously at a specified interblade phase angle using a high-speed cam driven system at frequencies as high as 550 Hz.   Further facility details can be found in Buffum and Fleeter.[30]

The experiments quantified the effects of separation and reduced frequency on the airfoil unsteady aerodynamic response (Buffum et al.[31], [32]).   The oscillating airfoil experiments were conducted at an interblade phase angle of 180°.   The experimental data used in this investigation were acquired at an inlet Mach number of 0.5 with a chordal Reynolds number of 0.9 Million for high and low incidence angle conditions.

In the experiment side wall suction was used to reduce the boundary layer thickness entering the cascade test section.   The tailboards also formed scoops to reduce the upper and lower wall boundary layers. The steady surface static pressure was measured at 52% (mid-span), 35%, and 17.5% span.   The chordwise distribution of the steady surface static pressure coefficients at the different spanwise locations for the high incidence condition were identical except for the point closest to the leading edge at 17.5% span, which was slightly higher.   To visualize the flow, and oil-pigment mixture on the airfoil suction surface was used in the experiment, which indicated at the high incidence angle condition that the boundary layer was separated from the leading edge to

10

40% chord. The extent of the separated flow region decreased to 7% chord at the endwalls. Based on the experimental results two dimensional simulations were pursued at the cascade mid-span.

In addition to the steady surface static pressure measurements, the surface time-dependent pressure distribution was also measured using miniature flush mounted pressure transducers at mid-span. Due to the small thickness of the airfoil in the leading edge and trailing edge regions, steady and time-dependent pressure instrumentation was installed only between 6 and 95% of the airfoil chord.

During the course of the experiment, some of the miniature pressure transducers failed. These failures are indicated by missing data points at 60 and 65% chord for the oscillating airfoil experiments. For the unsteady pressure distribution values, 95% confidence intervals of ±5% are estimated (Buffum et al.[32]).
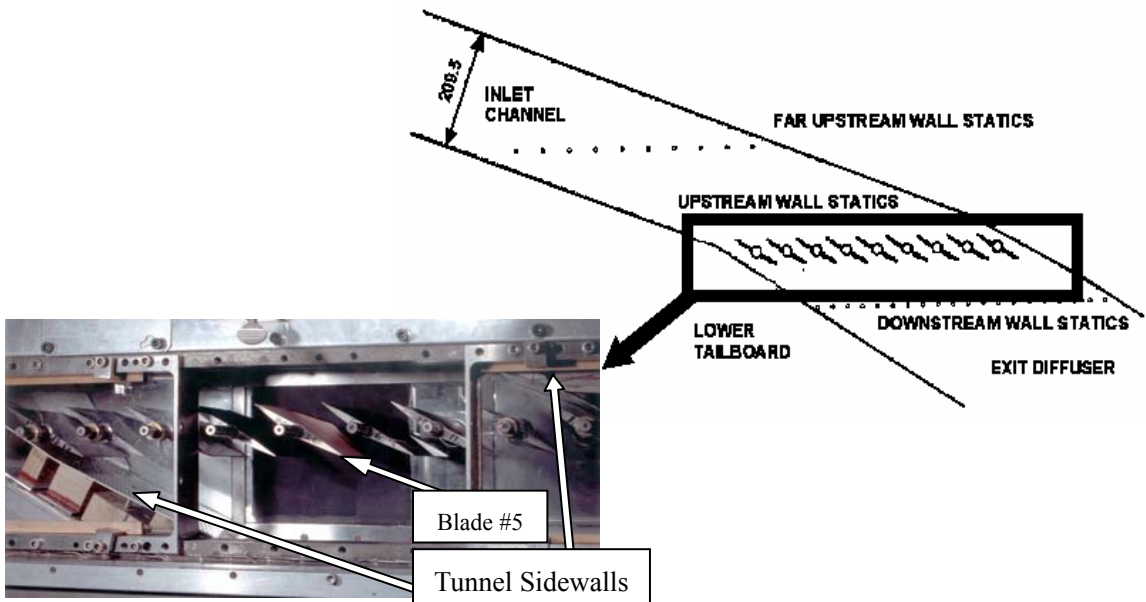
Figure 2.1 Experimental Facility

The airfoil used in the NASA-TFC has a cross-section similar to that found in the tip region of low aspect ratio fan blades. The loading levels, solidity, and stagger angle are consistent with current design practice. The airfoil cascade parameters are presented in Table 2.1, and Figure 2.2 illustrates the geometry.

Table 2.1 Airfoil and cascade parameters

Chord, C	8.89 cm
Maximum thickness, t_{max}	0.048 C
Maximum thickness location, x_{max}	0.625 C
Leading edge camber angle, θ^*	-6.2°
Number of airfoils	9
Stagger angle, Θ	60°
Solidity, C/S	1.52
Pitching axis (x_{pitch}, y_{pitch})	(0.5 C, -0.017 C)
Blade span, h	9.59 cm

Cascade geometry
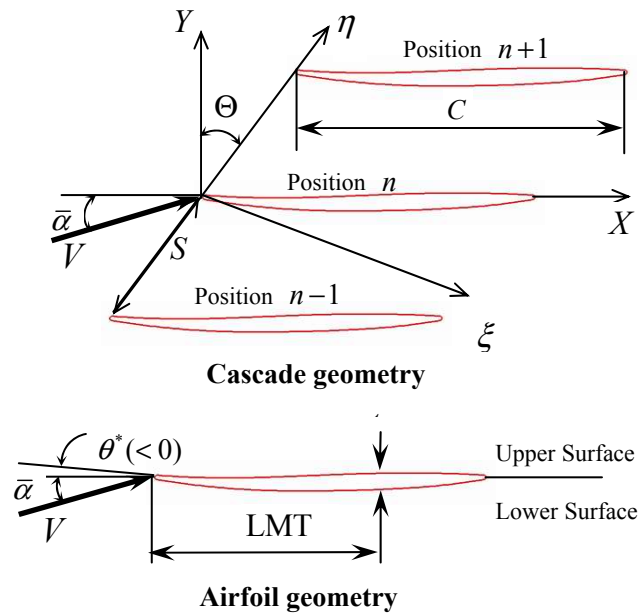
Airfoil geometry

Figure 2.2 Airfoil and cascade geometry

2.2 Grid Generation

The grid used to discretize the computational domain in this study has a sheared

H-mesh topology. The two dimensional grid was generated using Pointwise, which was developed by Pointwise Inc. It is capable of geometry modeling, structured, unstructured, and hybrid meshing, and interfaces to all the popular solver formats. More information can be found on their website.

2.2.1 Flat Plate Grids

The flat plates were modeled as a cascade with zero stagger angle and a solidity of 0.1. Two different size grids were used in the calculations. The coarse grid had 161 points in the flow direction and 60 points normal to the plate. A refined grid with 321 grid points in the flow direction and 120 points normal to the plate was also used. Figure 2.3 shows a typical flat plate used in the computation. The different boundaries and airfoil surfaces are shown in the figure. The grid topology is given in Table 2.2 and Δs represent the first grid distance to the wall.

Table 2.2 Flat plate grids topology

Grid Size	Δs	Inlet and Exit Boundaries from the leading edge	y^+	S/C
161x60	1.677e-6	2C, 3C	0.119	10
321x120	8.335e-7	2C, 3C	1.69E-002	10
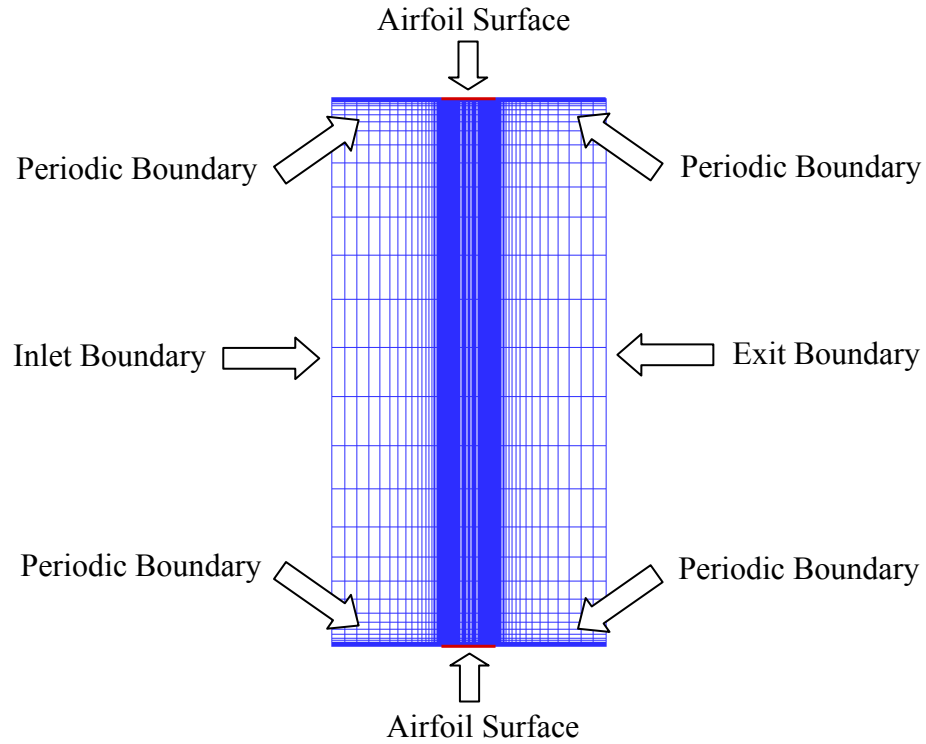
Figure 2.3 Flat plate grid (161x60)

2.2.2 NASA/P&W airfoil Grids

Two-dimensional grid 221x121 is used with 221 grid in the axial direction and 121 grid in the circumferential direction. Computations also performed on 361x161 grid and 421x201 grid to establish grid independency. The grids topology is in Table 2.3 and Δs represent the first grid distance to the wall.

Table 2.3 NASA/P&W airfoil grids topology

Grid Size	Δs	Inlet and Exit Boundaries from the leading edge	y^+	S/C
221x121	1.0e-5	2C, 3C	0.394	0.65789
361x161	1.0e-5	2C, 3C	0.389	0.65789
421x201	1.0e-5	2C, 3C	0.386	0.65789

The non-dimensional distance to the wall parameter y^+ is used to show how well the grids are within the boundary layer. Usually y^+ less than 1 is a good indication that there is sufficient grid being set within the boundary layer. As seen in Figure 2.4, y^+ is less than 2.5 for 221x121 and 361x161 grid for the whole airfoil, while y^+ is less than 1 for the 421x201 grid.
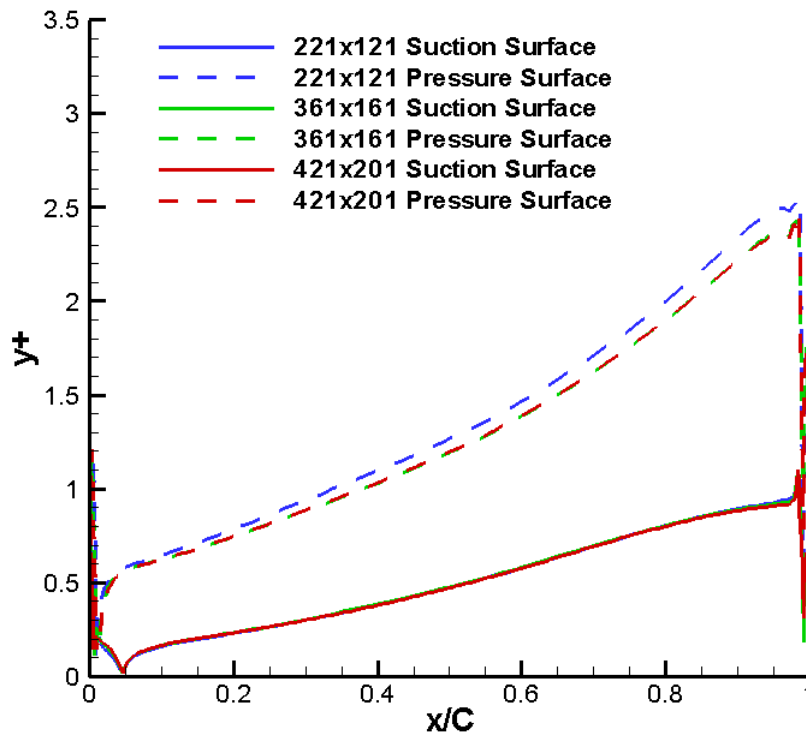
Figure 2.4 Non-dimensional distance to the wall along the airfoil surface

Figure 2.5 depicts the airfoil section of the grid. The grid uses 361 points in the axial and 161 points in the circumferential direction. This grid had a first point off the airfoil of approximately 1×10^{-5} as shown in Table 2.3, yielding y+ values less than 1. The upstream far field computational boundary was two chords upstream of the leading edge, and the downstream far field boundary was two chords downstream of the trailing edge. Figure 2.6 is the leading edge region of this grid.

15
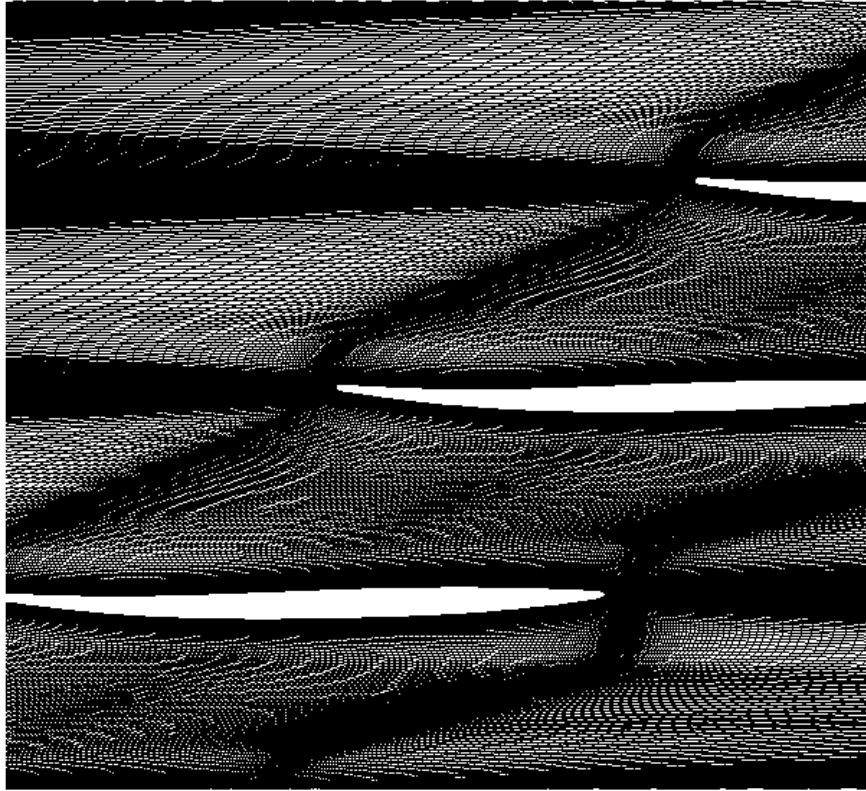
Figure 2.5 Sheared H-mesh (361x161) used for the steady and unsteady flow simulations
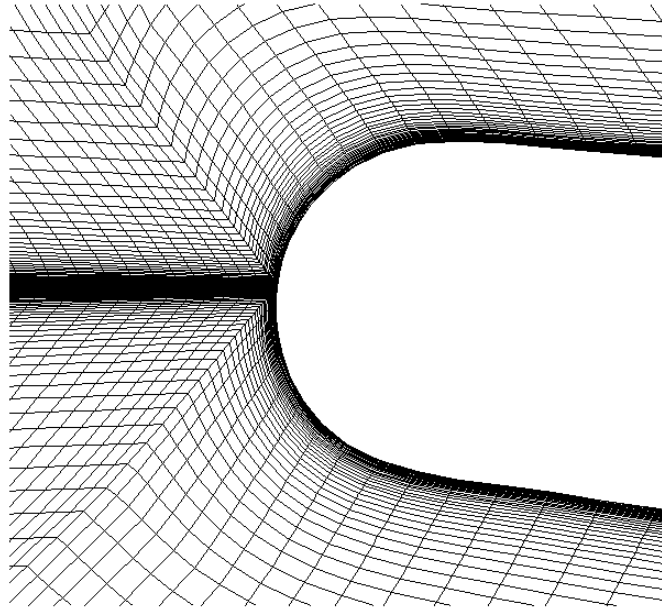
Figure 2.6 Leading edge region of the sheared H-mesh (361x161)

Chapter 3   Transition and Turbulence Models

Since laminar to turbulent flow transition is one of the most important phenomena in fluid flows, the accurate prediction of transition is particularly important for gas turbine engines where the onset and extent of transition can have a significant effect on the performance of the turbomachinery airfoils. Hence, accurate prediction of transition is very important to the design of turbomachinery.

Recently, studies have been conducted to improve the capability of computational fluid dynamics (CFD) codes. Navier-Stokes codes are used to calculate fully laminar or fully turbulent flows with reasonable accuracy. If the transition prediction from laminar to turbulent flow could be incorporated into the existing CFD codes this would greatly enhance their capabilities.

For flows in turbomachinery, transition is mostly caused by Bypass Transition, which is influenced by the high turbulence intensity outside the boundary layer from the upstream blade rows. Transition can be determined fundamentally through direct numerical simulation (DNS) or large eddy simulation (LES). DNS and LES are currently impractical for use in a design environment due to their large computational costs. Thus, for design purposes it is more feasible to combine existing Reynolds Averaged Navier-Stokes (RANS) solvers with a suitable transition model. In these models an intermittency factor multiplied by the turbulent eddy viscosity accounts for the transition region between laminar and turbulent flow.

But for the computational power nowadays, DNS and LES are not practical to perform a simulation on a complex flow field.

For the RNS based solvers with transition model, there are two main methods for modeling this type of transition in CFD. The first approach is to use two-equation low-Reynolds number turbulence models, depending on their ability to predict the transition onset and length. Since there is a relation between the viscous sublayer

formulation and the transition prediction, the models can not be calibrated independently. The change in the transition formulation would affect the fully turbulent solution. This method is favored for unstructured codes. Unfortunately, without further modifications these models tend to predict the onset of transition far too early, do not have the proper sensitivity to strong pressure gradients, and do not predict transition well in separated flows. Hence, these models are unreliable when used in transition simulations.

The second method is to calculate the laminar solution and integrate the boundary layer quantities to obtain the momentum thickness Reynolds number (Re_θ) at stream-wise locations. The momentum thickness Reynolds number is then used to predict the onset of transition based on an empirical correlation. Once the starting location of transition has been determined a turbulence model is turned on and the subsequent flow development is calculated. The intermittency factor is used to describe the intermittent laminar-turbulent flow behavior during transition. The intermittency factor is zero in the laminar region and gradually increases to one in the fully turbulent region. This approach can give sufficiently accurate results and is favored by industry models. However, the method is very hard to be implemented into unstructured codes because it is difficult to determine a proper integration strategy for the boundary layer quantities.

Since the second method needs to calculate the momentum thickness Reynolds numbers and compare with the critical value from the correlation, it is not easy to finish. The difficulty is that the boundary layer edge is not well defined and the integration will depend on the algorithm of search method.

3.1   Transition over a flat plate

An example of transition phenomena of flow over a flat plate is given in the following section. When flow passes a flat plate, at each point of the laminar boundary layer there is assumed to be a certain critical amplitude (and perhaps critical frequency range) which, when exceeded by a disturbance, is able to cause the oriented vorticity of

the laminar flow to be replaced by the confused motion of turbulence, just as the waves of the ocean break into white caps. As the ocean waves approach the shore, their amplitudes (and frequency) change, so that at random points the wave tips break. Similarly, in the laminar boundary layer the amplitude and frequency of disturbances and the critical conditions change with the distance from the leading edge. From time to time at various points, the boundary-layer disturbances "break", and the flow becomes locally turbulent and a turbulent spot has been created. From this spot, the confusion grows in all directions. Thus, the flow at any point on the body will be laminar part of the time and completely turbulent for the remainder.

The overall picture of the transition process in quiet flow past a smooth flat plate consists of the following processes:

1. Stable laminar flow near the leading edge
2. Unstable two-dimensional Tollmien-Schlicliting waves
3. Development of three-dimensional unstable waves and hairpin eddies
4. Vortex breakdown at regions of high localized shear
5. Cascading vortex breakdown into fully three-dimensional fluctuations
6. Formation of turbulent spots at locally intense fluctuations
7. Coalescence of spots into fully turbulent flow

These phenomena are sketched on an idealized flat-plate flow in Figure 3.1.
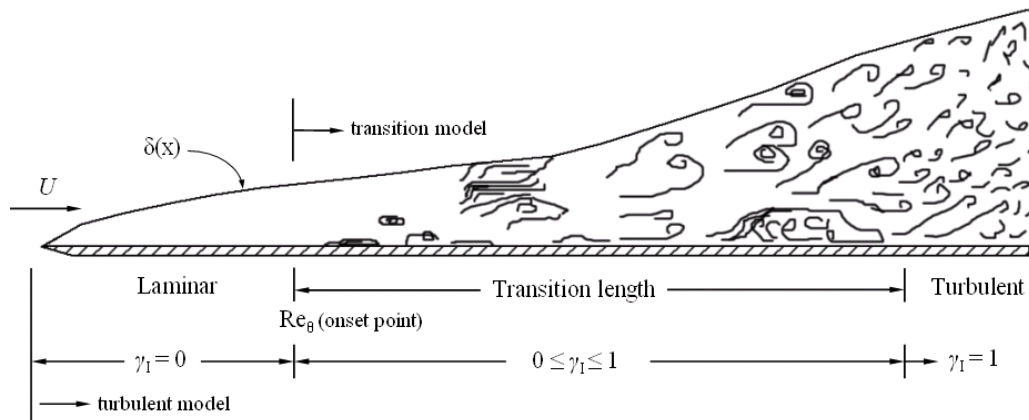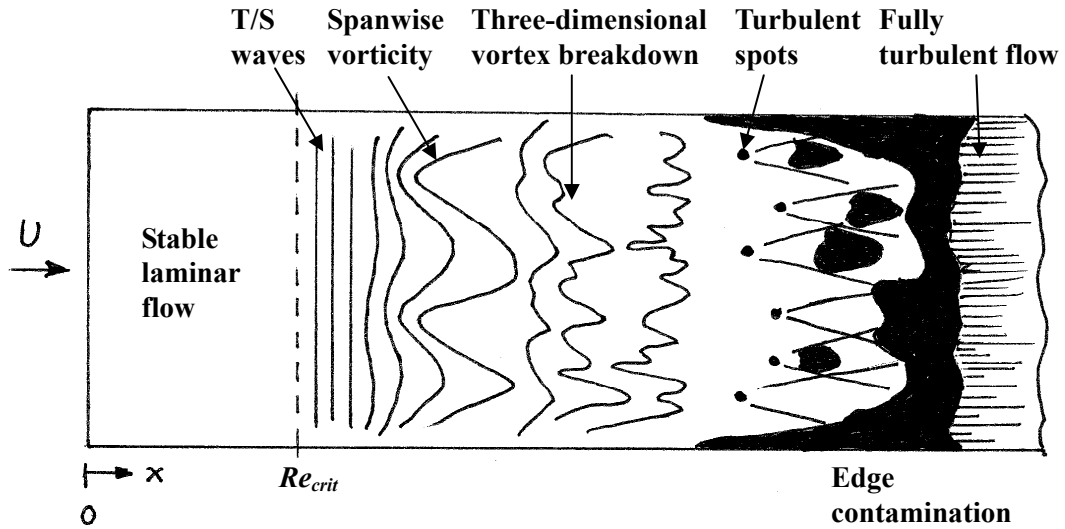
Figure 3.1 Idealized sketch of transition process on a flat plate (Schlichting[35])

3.2   Transition Modes

The flow near the surfaces can be either laminar or turbulent even though the flow in gas turbines is highly turbulent and unsteady. It is generally accepted that when stream-wise distance Reynolds number passes 350,000 natural transition occurs and the laminar region starts transition into a turbulent region. Generally, transition modes involve natural transition, bypass transition, and separated flow transition. In order to precisely calculate the losses and heat transfer on different components in the gas turbine engine, the prediction of transition is necessary (Mayle[14]).

21

Natural Transition involves three stages: (1) A laminar boundary layer becomes linearly unstable beyond a critical momentum thickness Reynolds number at which Tollmien-Schlichting waves start to grow. (2) Transition occurs after the waves become nonlinear and inviscid mechanisms come into play and result in three-dimensional disturbances (Klebanoff et al.[36]). (3) Turbulent spots are born (Emmons [1]) and grow in the surrounding laminar layer until they eventually coalesce into a turbulent boundary layer (Mayle[14]).

Bypass Transition occurs when there is a high level of free-stream turbulence (usually larger than 1%). The first two stages of the natural transition process can be completely bypassed so that turbulent spots are produced directly within the boundary layer. This type of transition commonly happens in gas turbines engines (Mayle[14]).

Separated-Flow Transition may occur in the shear layer of the separated flow as a result of the inviscid instability mechanism, when a laminar boundary layer separates. In this situation due to the strong mixing by the turbulent flow, the shear layer may reattach. This reattachment forms a laminar-separation/turbulent-reattachment bubble on the surface (Mayle [14]). In gas turbines, separation induced transition can also occur around the leading edge of an airfoil if the leading edge radius is small enough. This occurs mostly in compressors and low-pressure turbines. A schematic of a transitional separation bubble is shown in Figure 3.2.
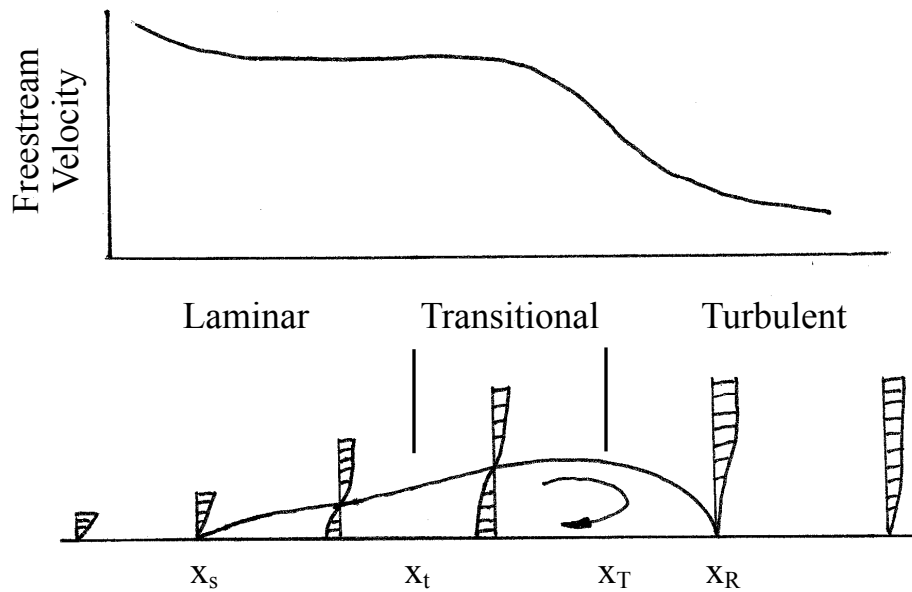
Figure 3.2 Velocity distribution over a separation bubble (Malkiel and Mayle[37]).

Relaminarization is the transition from turbulent to laminar flow. It is possible if the flow is strongly accelerated. Many articles define and explain the reversion of a turbulent flow to the laminar state, and this phenomenon is also referred as inverse or reverse transition, or relaminarization. The most obvious mechanism for the occurance of relaminarization is dissipation. When the Reynolds number goes down in a turbulent flow (e.g., by enlarging a duct or by branching a channel flow), the viscous dissipation may exceed the production of turbulent energy, and the flow may revert to a quasi-laminar state. The acceleration on the trailing edge pressure side of most airfoils and on the leading edge suction side of most turbines is large enough to cause reverse transition (Mayle[14]). There are not many experimental data on reverse transition but it is known that when the acceleration parameter, $K = \upsilon/U^2$ (dU/dx), is greater than about 3×10^{-6} (Mayle[14]). Also, it is possible for a relaminarized boundary layer to transition back to turbulent flow if the acceleration becomes small enough (i.e. $K < 3 \times 10^{-6}$).

3.3   Transition Models

There are two main parts to computing transitional flows in RANS codes: 1) determining the transition onset point, and 2) predicting the length of the transition zone. Current turbulence models are not able to perform these two tasks reliably. Hence, the approach taken in this research is to use a transition onset model to determine the transition onset location and a transition model to predict the transition zone length. Within the transition zone the intermittent behavior of the transitional boundary layer will be incorporated into existing turbulence models by using an intermittency factor. Once calculated, the intermittency factor is multiplied by the turbulent eddy viscosity to get an effective eddy viscosity.

$$\mu_{eff}(x, y) = \gamma_I(x)\mu_T(x, y) \qquad (3.1)$$

The effective viscosity is then used in the place of the turbulent eddy viscosity. The turbulent viscosity is calculated by using the Spalart-Allmaras [39] turbulence model.

The turbulence model is applied starting at the leading edge of the airfoil. In the laminar region, the intermittency factor is set to zero. In the transitional region, the intermittency factor varies between 0 and 1 and is determined by the transition length model. The turbulent flow region has an intermittency factor of 1. The intermittency factor is only a function of x which is the non-dimensional airfoil surface coordinates not a function of any other parameters. This entire process is shown schematically in Figure 3.3, which depicts a flat plate airfoil for illustrative purposes.

For this transition model, the intermittency function has only streamwise dependency; normal-to-wall effects are not considered for transition in this model since the flow parameters change more severely in the streamwise direction than in the normal direction. However, from an implementation point of view, the model is quite easy to use, and can be combined with any turbulence model.

24
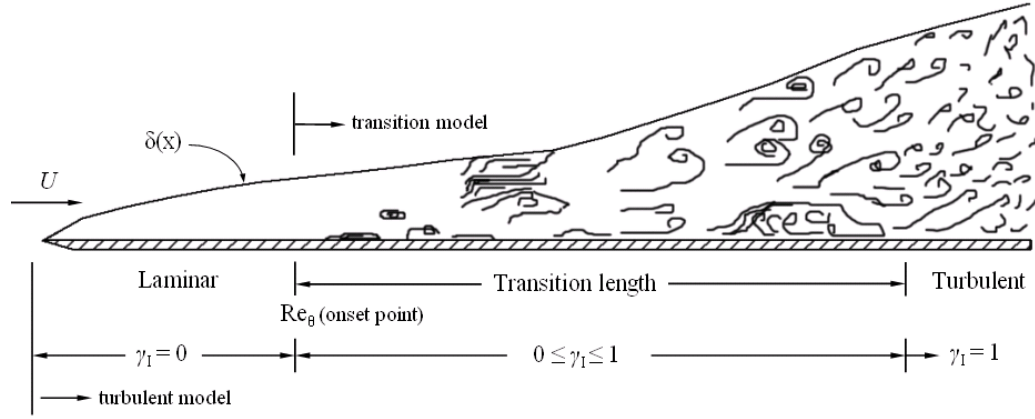
Figure 3.3 Schematic diagram illustrating the development of a turbulent boundary layer from an initially laminar boundary layer

A brief description of the Solomon, Walker and Gostelow[10] (SWG) transition model is presented below.

3.3.1 Solomon, Walker, and Gostelow Model

Solomon, Walker, and Gostelow[10] (SWG) developed a transition model that includes rapidly changing pressure gradients, and is based on the previous work of Narasimha[6], Chen and Thyson[7], and Gostelow et al[40]. It showed that the local pressure gradient parameter has a significant effect on the turbulent spot spreading angles and propagation velocities, which are very important for turbomachinery flows.

In the SWG transition model, the spot generation rate is determined using the dimensionless breakdown rate parameter proposed by Narasimha[6]

$$N = n\sigma\theta_t^3 / \nu \qquad\qquad (3.2)$$

where

n spot generation rate, $m^{-1}s^{-1}$

σ spot propagation parameter (dimensionless)

$$\sigma = 0.03 + (0.37 /(0.48 + 3.0\exp(52.9\lambda_\theta)))$$

θ_t momentum thickness at transition onset

25

λ_θ pressure gradient parameter, $(\theta^2/v)(dU/dx)$

U local free-stream velocity

Instead of using tangential velocity profile criteria ($0.99u_{tang}$) , the tangential velocity gradient is more suitable to find the boundary edge. Since the tangential velocity gradient along the normal direction to the wall changes greater within the boundary layer than outside the boundary layer, the boundary layer edge at a certain location, x, along the airfoil is determined by search from the mid-channel of the flow field to the airfoil surface where the following criteria is met,

$$\frac{du_{tang}}{ds_n} \geq 0.005 \max\left(\frac{du_{tang}}{ds_n}\right) \tag{3.3}$$

u_{tang} tangential velocity along the normal direction of the airfoil surface

s_n normal distance to the airfoil surface

The dimensionless breakdown rate parameter is obtained from the expression below and is dependent on the pressure gradient parameter and turbulence intensity (in %) at the transition onset point.

For $\lambda_\theta \leq 0$

$$N = 0.86 \times 10^{-3} \exp(2.134\lambda_\theta \ln(q) - 59.23\lambda_\theta - 0.564\ln(q)) \tag{3.4}$$

For $\lambda_\theta > 0$

$$N = N_0 \times \exp(-10\sqrt{\lambda_\theta}) \tag{3.5}$$

where N_0 is the value of N at $\lambda_\theta = 0$.

The spreading half-angle and the spot propagation parameter are determined using the relations

$$\alpha = 4 + (22.14/(0.79 + 2.72\exp(47.63\lambda_\theta)))$$
$$\sigma = 0.03 + (0.37/(0.48 + 3.0\exp(52.9\lambda_\theta))) \tag{3.6}$$

where the functional dependence on the local pressure gradient parameter is apparent.

The intermittency function is calculated using

$$\gamma_I = 1 - \exp\left[-n\int_{x_t}^{x} \frac{\sigma}{\tan\alpha} \frac{dx}{U} \int_{x_t}^{x} \tan\alpha\, dx \right] \qquad (3.7)$$

The intermittency function is only being a function of x, the streamwise direction. The SWG model is based on measurements in attached flows. The pressure gradient parameter can assume values that exceed the experimental data range used in the development of this method. When this occurs for adverse pressure gradients the spot generation rate becomes very high, which yields instantaneous transition. In the NPHASE implementation of the SWG model the value of the pressure gradient parameter is limited, i.e., $-0.08 \leq \lambda_\theta \leq 0.1$.

3.3.2 Transition Onset Models

In general, transition length models need a transition onset point. Starting at the transition onset point, a transition length model calculates the transition length and the intermittency function along this length. As part of this study, several transition onset models were investigated. These transition onset models are summarized in Table 3.1 along with the conditions for which they are applicable. Note that Tu is the freestream turbulence intensity and K_t is the maximum absolute value of the acceleration parameter.

Table 3.1 Transition Onset criteria.

Onset Model	Basic Relationship	Conditions
Michel's criteria[41]	$\text{Re}_\theta = 1.174\left[1+\dfrac{22400}{\text{Re}_x}\right]\text{Re}_x^{0.46}$	Attached Flow, $\text{Re} \geq 1 \cdot 10$
Suzen et al.[21]	$\text{Re}_\theta = \dfrac{120+150Tu^{-\frac{2}{3}}}{\tanh\left[4\left(0.3-K_t \cdot 10^5\right)\right]}$	Attached Flow, $Tu \geq 1\%$
Suzen et al.[21]	$\text{Re}_{st} = 874\,\text{Re}_{\theta s}^{0.71}\exp[-0.4Tu]$	Separated Flow
Steelant and Dick[42]	$\text{Re}_\theta = 0.664\sqrt{400094Tu^{-1.38}-105254Tu^{-\frac{7}{8}}}$	Attached Flow
Praisner and Clark[43]	$\text{Re}_{st} = 173\,\text{Re}_s\,\text{Re}_{\theta s}^{-1.227}$	Separated Flow

3.3.3 Instantaneous Transition

The turbulence model is applied starting at the leading edge of the airfoil. In the laminar region, the intermittency factor is set to zero. At the transition onset location, the intermittency factor is set to 1. The transition from laminar to turbulent is instantaneous. Right after the transition onset point, is the turbulent flow region.

3.4 Turbulence Models

Turbulence is one of the key phenomena in fluid dynamics. Turbulent flows occur in many important engineering applications. These flows are extremely complex involving seemingly random and chaotic motions. The physics of these flows is still not fully understood and the structure of turbulent flows is one of the remaining unsolved problems in classical physics.

3.4.1 Direct numerical simulation

The Navier-Stokes equations are the mathematical equations which describe a

fluids motion. It is possible to directly solve the Navier-Stokes equations for laminar flows and for turbulent flows when all of the relevant length scales can be resolved by the grid (Direct numerical simulation).   Direct numerical simulation (DNS) captures all of the relevant scales of turbulent motion, so no model is needed for the smallest scales. However, this approach is extremely expensive for complex problems.   The range of length scales appropriate to the problem is larger than even today's massively parallel computers can model.   Hence, turbulent flow simulations require the need for models to represent the smallest scales of fluid motion.   Large eddy simulations (LES) and the Reynolds averaged Navier-Stokes equations (RANS) formulation, with the k-ε model or the Reynolds stress model, are two techniques for dealing with these scales.

3.4.2   Large eddy simulation

Large eddy simulation (LES) is a technique in which the smaller eddies are filtered and are modeled using a sub-grid scale model, while the larger eddies are simulated. This method generally requires a more refined mesh than a RANS model, but a far coarser mesh than a DNS solution.   But LES method is still very costly and impractical for the problems investigated in this work. Thus, for design purposes it is more feasible to combine existing RANS solvers to solve the engineering problems.

3.4.3   Reynolds stress model

The RANS solver involves using an algebraic equation for the Reynolds stresses which include determining the turbulent viscosity or solving transport equations for determining the turbulent kinetic energy and dissipation. The RANS turbulence models are often referred to by the number of transport equations included, for example the Baldwin-Lomax model is a "Zero Equation" model because no transport equations are solved, Spalart-Allmaras model is a "One Equation" model requiring solve one transport equation, and the k-ε is a "Two Equation" model because two transport equations are

solved. The major challenge is accuracy of turbulence models for simulations of complex turbulent flows. But the development of improved turbulence models has increased in the last decade. Figure 3.4 illustrate the different methods for turbulence simulation now a day. In this work, Spallart-Allmaras model was picked as the turbulent model to perform the fully turbulent simulation.
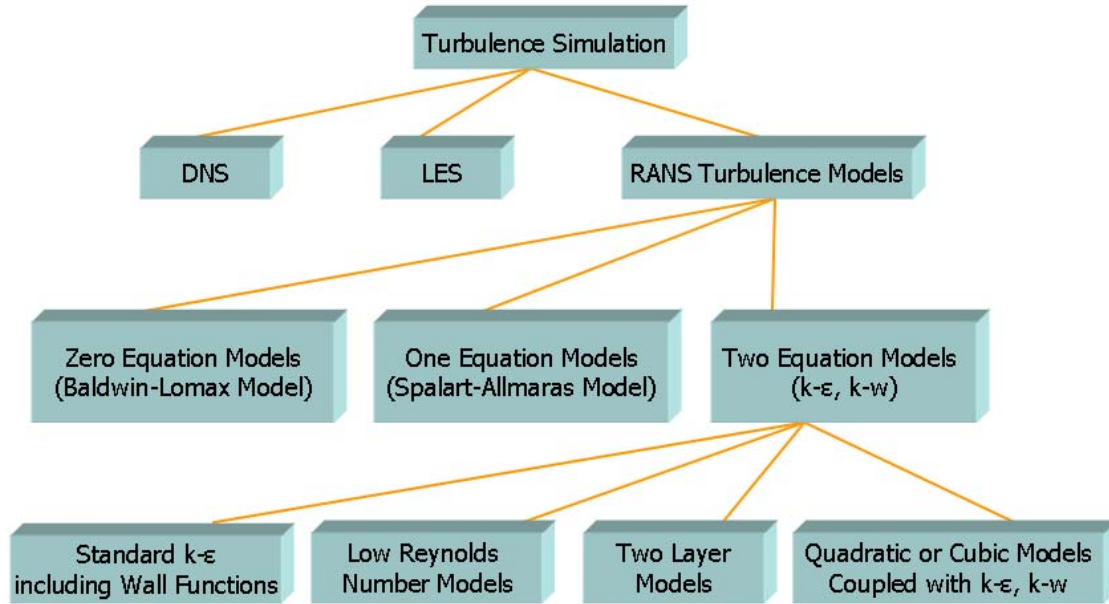
Figure 3.4 Diagram of Turbulence Simulation

3.4.4 Spalart-Allmaras Model

The Spalart-Allmaras model[39] computes the eddy viscosity using a transport equation. In the transport equation an intermediate variable ($\tilde{v}$), is used to compute the eddy viscosity (v_t) through the relation $v_t = \tilde{v} f_{v1}(\chi)$, where $\chi = \tilde{v}/v$, and f_{v1} is a damping function. The intermediate variable, $\tilde{v}$, is computed by the following transport equation,[39]

$$\frac{D\tilde{v}}{Dt} = c_{b1}\left[1 - f_{t2}\right]\tilde{S}\tilde{v} + \frac{1}{\sigma}\left[\nabla \cdot \left((v + \tilde{v})\nabla\tilde{v}\right) + c_{b2}\left(\nabla\tilde{v}\right)^2\right]$$
$$-\left[c_{w1}f_w - \frac{c_{b1}}{\kappa^2}f_{t2}\right]\left[\frac{\tilde{v}}{d}\right]^2 + f_{t1}\Delta U^2 \tag{3.8}$$

where the eddy viscosity is given by

$$v_t = \tilde{v}f_{v1} \qquad f_{v1} = \frac{\chi^3}{\chi^3 + c_{v1}^3} \qquad \chi = \frac{\tilde{v}}{v} \tag{3.9}$$

Various functions and constants appearing in Equation (3.8) are defined as

$$\tilde{S} = S + \frac{\tilde{v}}{\kappa^2 d^2}f_{v2} \tag{3.10}$$

where d is the nearest distance to the wall, κ is the von Karman constant, S is the magnitude of the vorticity, in two-dimensional case

$$S = \sqrt{\left(\frac{\partial u}{\partial y} - \frac{\partial v}{\partial x}\right)^2} \tag{3.11}$$

The function f_w is

$$f_w = g\left[\frac{1 + c_{w3}^6}{g^6 + c_{w3}^6}\right]^{1/6} \tag{3.12}$$

where

$$g = r + c_{w2}(r^6 - r) \qquad r = \frac{\tilde{v}}{\tilde{S}\kappa^2 d^2} \tag{3.13}$$

Large values of r should be truncated to a value of about 10. The function f_{t2} is given by

$$f_{t2} = c_{t3}\exp(-c_{t4}\chi^2) \tag{3.14}$$

and the trip function f_{t1} is

$$f_{t1} = c_{t1}g_t \exp\left[-c_{t2}\frac{\omega_t^2}{\Delta U^2}\left(d^2 + g_t^2 d_t^2\right)\right] \tag{3.15}$$

The following are used in Equation(3.15):

d_t: The distance from the field point to the trip, which is located on the surface.

ω_t: The wall vorticity at the trip.

ΔU: The difference between the velocities at the field point and trip.

g_t: $g_t = \min[0.1, \Delta U / \omega_t \Delta x_t]$, where Δx_t is the grid spacing along the wall at the trip.

The trip term and transition formulation are not used in this work.

The constants used in the equations above are:[39]

$$\sigma = \frac{2}{3} \qquad\qquad c_{b1} = 0.1355 \qquad\qquad c_{b2} = 0.622$$

$$c_{w1} = \frac{c_{b1}}{\kappa^2} + (1 + c_{b2}) / \sigma \qquad\qquad c_{w2} = 0.3 \qquad\qquad c_{w3} = 2$$

$$\kappa = 0.41 \qquad\qquad c_{v1} = 7.1 \qquad\qquad c_{t1} = 1$$

$$c_{t2} = 2 \qquad\qquad c_{t3} = 1.2 \qquad\qquad c_{t4} = 0.5$$

The Spalart-Allmaras turbulence model given by (3.8) can be written as

$$\begin{aligned}
\frac{\partial \tilde{v}}{\partial t} = &-u_j \frac{\partial \tilde{v}}{\partial x_j} + c_{b1}(1 - f_{t2}) S \tilde{v} \\
&+ \frac{1}{\sigma} \frac{\partial}{\partial x_j} \left\{ [v + (1 + c_{b2}) \tilde{v}] \frac{\partial \tilde{v}}{\partial x_j} \right\} - \frac{c_{b2}}{\sigma} \tilde{v} \frac{\partial^2 \tilde{v}}{\partial x_j^2} \\
&- \left\{ c_{w1} f_w - \frac{c_{b1}}{\kappa^2} [(1 - f_{t2}) f_{v2} + f_{t2}] \right\} \left(\frac{\tilde{v}}{d} \right)^2 \\
&+ f_{t1} \Delta U^2
\end{aligned} \qquad (3.16)$$

3.4.4.1 Nondimensional and transformed Spalart-Allmaras turbulence model

The nondimensionalized and transformed form of Equation (3.16) is

$$\frac{\partial \tilde{v}}{\partial \tau} + U \frac{\partial \tilde{v}}{\partial \xi} + V \frac{\partial \tilde{v}}{\partial \eta}$$

$$= \frac{1}{\text{Re}_{ref}} \frac{1}{\sigma} \left\{ \begin{array}{c} \xi_x \dfrac{\partial \alpha}{\partial \xi} + \eta_x \dfrac{\partial \alpha}{\partial \eta} \\[6pt] + \xi_y \dfrac{\partial \beta}{\partial \xi} + \eta_y \dfrac{\partial \beta}{\partial \eta} \\[6pt] + \xi_z \dfrac{\partial \gamma}{\partial \xi} + \eta_z \dfrac{\partial \gamma}{\partial \eta} \end{array} \right\} - \frac{1}{\text{Re}_{ref}} \frac{c_{b2}}{\sigma} \tilde{v} \left\{ \begin{array}{c} \xi_x \dfrac{\partial A}{\partial \xi} + \eta_x \dfrac{\partial A}{\partial \eta} \\[6pt] + \xi_y \dfrac{\partial B}{\partial \xi} + \eta_y \dfrac{\partial B}{\partial \eta} \\[6pt] + \xi_z \dfrac{\partial C}{\partial \xi} + \eta_z \dfrac{\partial C}{\partial \eta} \end{array} \right\}$$

$$+ c_{b1} \left(1 - f_{t2} \right) S \tilde{v} \tag{3.17}$$

$$+ \frac{1}{\text{Re}_{ref}} \left\{ \frac{c_{b1}}{\kappa^2} \left[\left(1 - f_{t2} \right) f_{v2} + f_{t2} \right] - c_{w1} f_w \right\} \left(\frac{\tilde{v}}{d} \right)^2$$

$$+ \text{Re}_{ref} \, f_{t1} \Delta U^2$$

where

$$\alpha = \left[v + \left(1 + c_{b2} \right) \tilde{v} \right] \left(\xi_x \frac{\partial \tilde{v}}{\partial \xi} + \eta_x \frac{\partial \tilde{v}}{\partial \eta} \right) \qquad A = \xi_x \frac{\partial \tilde{v}}{\partial \xi} + \eta_x \frac{\partial \tilde{v}}{\partial \eta}$$

$$\beta = \left[v + \left(1 + c_{b2} \right) \tilde{v} \right] \left(\xi_y \frac{\partial \tilde{v}}{\partial \xi} + \eta_y \frac{\partial \tilde{v}}{\partial \eta} \right) \qquad B = \xi_y \frac{\partial \tilde{v}}{\partial \xi} + \eta_y \frac{\partial \tilde{v}}{\partial \eta}$$

$$\gamma = \left[v + \left(1 + c_{b2} \right) \tilde{v} \right] \left(\xi_z \frac{\partial \tilde{v}}{\partial \xi} + \eta_z \frac{\partial \tilde{v}}{\partial \eta} \right) \qquad C = \xi_z \frac{\partial \tilde{v}}{\partial \xi} + \eta_z \frac{\partial \tilde{v}}{\partial \eta}$$

Equation (3.17) is now written as

$$\frac{\partial \tilde{v}}{\partial \tau} = M + P + D + T \tag{3.18}$$

where

$$M = M^1 + M^2 + M^3 \tag{3.19}$$

$$M^1 = -\left(U \frac{\partial \tilde{v}}{\partial \xi} + V \frac{\partial \tilde{v}}{\partial \eta} \right) \tag{3.20}$$

$$M^2 = \frac{1}{\mathrm{Re}_{ref}} \frac{1}{\sigma} \left\{ \begin{array}{l} \xi_x \dfrac{\partial\left[\nu+(1+c_{b2})\tilde{\nu}\right]\left(\xi_x \dfrac{\partial\tilde{\nu}}{\partial\xi}\right)}{\partial\xi} + \eta_x \dfrac{\partial\left[\nu+(1+c_{b2})\tilde{\nu}\right]\left(\eta_x \dfrac{\partial\tilde{\nu}}{\partial\eta}\right)}{\partial\eta} \\[4ex] +\xi_y \dfrac{\partial\left[\nu+(1+c_{b2})\tilde{\nu}\right]\left(\xi_y \dfrac{\partial\tilde{\nu}}{\partial\xi}\right)}{\partial\xi} + \eta_y \dfrac{\partial\left[\nu+(1+c_{b2})\tilde{\nu}\right]\left(\eta_y \dfrac{\partial\tilde{\nu}}{\partial\eta}\right)}{\partial\eta} \end{array} \right\} \tag{3.21}$$

$$M^3 = -\frac{1}{\mathrm{Re}_{ref}} \frac{c_{b2}}{\sigma} \tilde{\nu} \left\{ \begin{array}{l} \xi_x \dfrac{\partial\left(\xi_x \dfrac{\partial\tilde{\nu}}{\partial\xi}\right)}{\partial\xi} + \eta_x \dfrac{\partial\left(\eta_x \dfrac{\partial\tilde{\nu}}{\partial\eta}\right)}{\partial\eta} \\[4ex] +\xi_y \dfrac{\partial\left(\xi_y \dfrac{\partial\tilde{\nu}}{\partial\xi}\right)}{\partial\xi} + \eta_y \dfrac{\partial\left(\eta_y \dfrac{\partial\tilde{\nu}}{\partial\eta}\right)}{\partial\eta} \end{array} \right\} \tag{3.22}$$

$$P = c_{b1}\left(1-f_{t2}\right)S\tilde{\nu} \tag{3.23}$$

$$D = \frac{1}{\mathrm{Re}_{ref}} \left\{ \frac{c_{b1}}{\kappa^2}\left[\left(1-f_{t2}\right)f_{v2}+f_{t2}\right]-c_{w1}f_w \right\} \left(\frac{\tilde{\nu}}{d}\right)^2 \tag{3.24}$$

$$T = \mathrm{Re}_{ref} \, f_{t1}\Delta U^2 \tag{3.25}$$

The terms $M^{<2>}$ and $M^{<3>}$ can be further regrouped as terms including ξ derivatives and terms involving η derivatives as follow

$$M_{\xi}^{<2>} = \frac{1}{\mathrm{Re}_{ref}} \frac{1}{\sigma} \left\{ \xi_x \dfrac{\partial\left[\nu+(1+c_{b2})\tilde{\nu}\right]\left(\xi_x \dfrac{\partial\tilde{\nu}}{\partial\xi}\right)}{\partial\xi} + \xi_y \dfrac{\partial\left[\nu+(1+c_{b2})\tilde{\nu}\right]\left(\xi_y \dfrac{\partial\tilde{\nu}}{\partial\xi}\right)}{\partial\xi} \right\} \tag{3.26}$$

$$M_\eta^{<2>} = \frac{1}{\text{Re}_{ref}} \frac{1}{\sigma} \left\{ \eta_x \frac{\partial \left[\nu + (1+c_{b2})\tilde{v} \right] \left(\eta_x \frac{\partial \tilde{v}}{\partial \eta} \right)}{\partial \eta} + \eta_y \frac{\partial \left[\nu + (1+c_{b2})\tilde{v} \right] \left(\eta_y \frac{\partial \tilde{v}}{\partial \eta} \right)}{\partial \eta} \right\} \tag{3.27}$$

$$M_\xi^{<3>} = -\frac{1}{\text{Re}_{ref}} \frac{c_{b2}}{\sigma} \tilde{v} \left[\xi_x \frac{\partial \left(\xi_x \frac{\partial \tilde{v}}{\partial \xi} \right)}{\partial \xi} + \xi_y \frac{\partial \left(\xi_y \frac{\partial \tilde{v}}{\partial \xi} \right)}{\partial \xi} \right] \tag{3.28}$$

$$M_\eta^{<3>} = -\frac{1}{\text{Re}_{ref}} \frac{c_{b2}}{\sigma} \tilde{v} \left[\eta_x \frac{\partial \left(\eta_x \frac{\partial \tilde{v}}{\partial \eta} \right)}{\partial \eta} + \eta_y \frac{\partial \left(\eta_y \frac{\partial \tilde{v}}{\partial \eta} \right)}{\partial \eta} \right] \tag{3.29}$$

3.4.4.2 Time Differencing

By using Euler backward differencing, Equation (3.18) is applied at time level n+1. Therefore,

$$\left(\frac{\partial \tilde{v}}{\partial \tau} \right)^{n+1} = M^{n+1} + D^{n+1} + P^n + T^n \tag{3.30}$$

where the trip term and production are treated as a source term evaluated at time level *n*.

3.4.4.3 Time Linearization

The general expression of linearized equation is

$$E^{n+1} = E^n + A\Delta u \tag{3.31}$$

where

$$A = \frac{\partial E}{\partial u}$$

Now the linearization (3.31) provides

$$M^{n+1} = M^n + \frac{\partial M}{\partial \tilde{v}} \Delta \tilde{v} = M^n + \bar{M}\Delta \tilde{v} \tag{3.32}$$

$$D^{n+1} = D^n + \frac{\partial D}{\partial \tilde{v}} \Delta \tilde{v} = D^n + \bar{D} \Delta \tilde{v} \tag{3.33}$$

Now Equation (3.30) can be written as

$$\frac{\Delta \tilde{v}}{\Delta \tau} - \left(\bar{M} + \bar{D} \right) \Delta \tilde{v} = M^n + P^n + D^n + T^n \tag{3.34}$$

or

$$\left[I - \left(\bar{M} + \bar{D} \right) \Delta \tau \right] \Delta \tilde{v} = \left(M^n + P^n + D^n + T^n \right) \Delta \tau \tag{3.35}$$

Recall that, in the development of expressions for M, it was decomposed as M_ξ and M_η. Therefore, the Equation (3.35) can be written as

$$\left[I - \left(\bar{M}_\xi + \bar{M}_\eta + \bar{D} \right) \Delta \tau \right] \Delta \tilde{v} = RHS \tag{3.36}$$

where

$$RHS = \left(M^n + P^n + D^n + T^n \right) \Delta \tau \tag{3.37}$$

I is an identity matrix.

3.4.4.4 Approximate Factorization

By using the approximate factorization method, the two-dimensional Equation (3.36) can be reduced to the following two unidimensional equations

$$\left(I - \Delta \tau \bar{M}_\xi \right) \Delta \tilde{v}^* = RHS \tag{3.38}$$

$$\left[I - \Delta \tau \left(\bar{M}_\eta + \bar{D} \right) \right] \Delta \tilde{v} = \Delta \tilde{v}^* \tag{3.39}$$

3.4.4.5 Initial condition and boundary conditions

The initial condition for $\tilde{v}$ is specified to be 1.341946. The boundary conditions are,

1. At the inflow, $\tilde{v} = 1.341946$, which implies $\mu_T = 0.009$, (CFL3D User's Manual[47])

2. At the solid surface $\tilde{v} = 0$,

3. At the outflow, extrapolation is used,

4. At the periodic boundary, extrapolation is used,

5. For unsteady prediction, the averaged value is used at the block interface.

Chapter 4   Computational Model

Computational fluid dynamics (CFD) is one of the branches of fluid mechanics that uses numerical methods to solve and analyze problems that involve fluid flows. The Navier-Stokes equations are the mathematical equations which describe a fluids motion. Solving the Navier-Stokes equations require lots of computational power. Over the past few decades, many computational models have been developed to solve the Navier-Stokes equations and apply the solutions to engineering problems.

4.1   Navier-Stokes Equations

The Navier-Stokes (NS) equations are briefly summarized this section[48]. The Reynolds Averaged Navier–Stokes (RANS) equations are time-averaged equations of motion for fluid flow. They are used when dealing with turbulent flows. The RANS equations in a stationary frame and using the Boussinesq eddy-viscosity assumption to relate the Reynolds stress and turbulent flux terms to the mean flow variables are defined below,

The conservation of mass equation is given in Equation (4.1)

$$\frac{\partial \rho}{\partial t} + \frac{\partial}{\partial x_j}\left(\rho \bar{U}_j\right) = 0 \tag{4.1}$$

The conservation of momentum equation is given in Equation (4.2)

$$\frac{\partial}{\partial t}\left(\rho \bar{U}_i\right) + \frac{\partial}{\partial x_j}\left(\rho \bar{U}_j \bar{U}_i\right) = -\frac{\partial P^*}{\partial x_i} + \frac{\partial}{\partial x_j}\left\{\mu_{eff}\left(\frac{\partial \bar{U}_i}{\partial x_j} + \frac{\partial \bar{U}_j}{\partial x_i}\right) - \frac{2}{3}\mu_{eff}\frac{\partial \bar{U}_l}{\partial x_l}\delta_{ij}\right\} \tag{4.2}$$

In Equation(4.2), P^* is the sum of the pressure (P) and the $\frac{2}{3}\rho\delta_{ij}k$ term which comes from the eddy viscosity Boussinesq assumption. The two are grouped together because they are both scalar normal stresses.

The effective viscosity is the sum of the laminar and turbulent viscosities,

$$\mu_{eff} = \mu + \mu_T \tag{4.3}$$

4.2 NPHASE

NPHASE was originally developed by the Engineering Research Center at Mississippi State University (Swafford et al.[49]). It is an implicit, cell-centered, finite-volume, compressible turbomachinery flow simulator that solves two-dimensional nonlinear steady and unsteady flow fields for turbomachinery geometries using structured H-grids. It is capable of solving both viscous (using the thin-layer Reynolds Averaged Navier-Stokes equations) and inviscid (Euler) flows.

The computational mesh used in NPHASE is a sheared H-mesh. This structured mesh defines a curvilinear coordinate system, in which coordinate curves lie along the boundaries of the physical domain. NPHASE is executed in a two-step process. First, the steady flow field is determined. Once the steady flow field is determined, the unsteady calculations can be initiated.

Initially, there was no transition model and the Baldwin and Lomax[44] algebraic turbulence model was used for viscous flow computations. In this research effort, the Spalart-Allmaras[39] turbulence model and the Solomon, Walker, and Gostelow[10] transition model have been implemented in the code. Different transition onset models (specified, Michel[41], Suzen et al.[21], Steelant and Dick[42], and Praisner and Clark[43]) have also been added to NPHASE.

Both gust (Ayer and Verdon[50]) and oscillating airfoil unsteady aerodynamics can be calculated. For oscillating airfoil unsteady flow simulations, a time marching method with a deforming computational mesh that uses multiple airfoil passages to satisfy periodicity is used.

More details on the numerical scheme and solution procedures for NPHASE can be found in Swafford et al[49] and Ayer and Verdon.[50]

4.3   Limiting

This section will summarize the limiting used for the SWG and SA models.

1. The SWG model is based on measurements in attached flows. The pressure gradient parameter can assume values that exceed the experimental data range used in the development of this method. When this occurs for adverse pressure gradients the spot generation rate becomes very high, which yields instantaneous transition. In the NPHASE implementation of the SWG model the value of the pressure gradient parameter at transition onset ($\lambda_{\theta t}$) is limited to between -0.08 and 0.1.
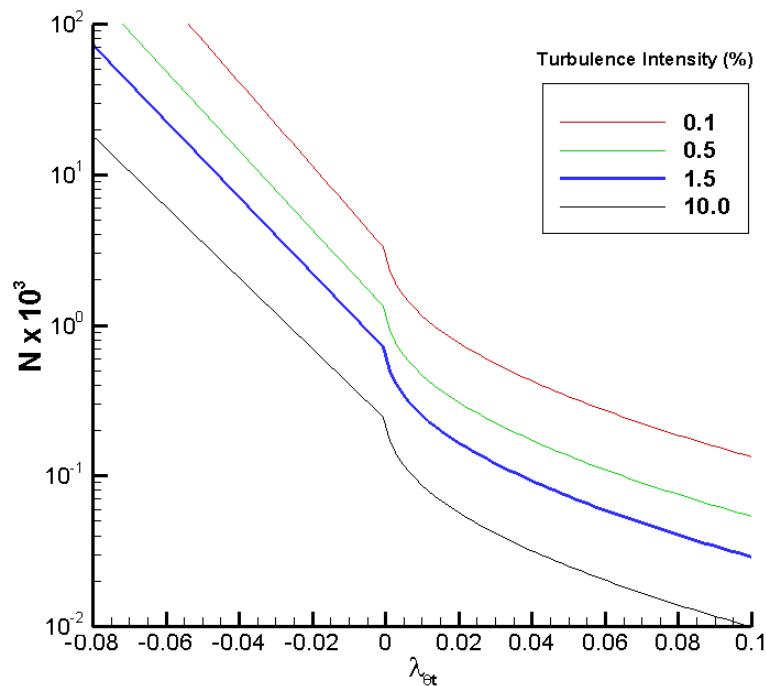
Figure 4.1 Non-dimensional breakdown rate parameter as a function of freestream turbulence and pressure gradient parameter at transition onset

2. The break down parameter is limited to between 10^{-5} and 1.
3. In the Spalart-Allmaras model, the diffusion term, can be written as

$$\frac{1}{\mathrm{Re}_{ref}}\frac{1}{\sigma\Delta\xi_{i,j}}\left\{\begin{array}{l}\xi_{x_{i,j}}\left[\{\psi\xi_x\}_{i+\frac{1}{2},j}\left(\frac{\Delta^n\tilde{v}_{i+1,j}-\Delta^n\tilde{v}_{i,j}}{\Delta\xi_{i+\frac{1}{2},j}}\right)-\{\psi\xi_x\}_{i-\frac{1}{2},j}\left(\frac{\Delta^n\tilde{v}_{i,j}-\Delta^n\tilde{v}_{i-1,j}}{\Delta\xi_{i-\frac{1}{2},j}}\right)\right]\\[4mm]+\xi_{y_{i,j}}\left[\{\psi\xi_y\}_{i+\frac{1}{2},j}\left(\frac{\Delta^n\tilde{v}_{i+1,j}-\Delta^n\tilde{v}_{i,j}}{\Delta\xi_{i+\frac{1}{2},j}}\right)-\{\psi\xi_y\}_{i-\frac{1}{2},j}\left(\frac{\Delta^n\tilde{v}_{i,j}-\Delta^n\tilde{v}_{i-1,j}}{\Delta\xi_{i-\frac{1}{2},j}}\right)\right]\end{array}\right\}$$

$$-\frac{1}{\mathrm{Re}_{ref}}\frac{c_{b2}}{\sigma\Delta\xi_{i,j}}\tilde{v}_{i,j}\left\{\begin{array}{l}\xi_{x_{i,j}}\left[\xi_{x_{i+\frac{1}{2},j}}\left(\frac{\Delta^n\tilde{v}_{i+1,j}-\Delta^n\tilde{v}_{i,j}}{\Delta\xi_{i+\frac{1}{2},j}}\right)-\xi_{x_{i-\frac{1}{2},j}}\left(\frac{\Delta^n\tilde{v}_{i,j}-\Delta^n\tilde{v}_{i-1,j}}{\Delta\xi_{i-\frac{1}{2},j}}\right)\right]\\[4mm]+\xi_{y_{i,j}}\left[\xi_{y_{i+\frac{1}{2},j}}\left(\frac{\Delta^n\tilde{v}_{i+1,j}-\Delta^n\tilde{v}_{i,j}}{\Delta\xi_{i+\frac{1}{2},j}}\right)-\xi_{y_{i-\frac{1}{2},j}}\left(\frac{\Delta^n\tilde{v}_{i,j}-\Delta^n\tilde{v}_{i-1,j}}{\Delta\xi_{i-\frac{1}{2},j}}\right)\right]\end{array}\right\}$$

where $\psi=v+(1+c_{b2})\tilde{v}$. Part of the terms in two-dimensional format are limited as follows:

$$\frac{1}{\mathrm{Re}_{ref}\,\sigma\Delta\xi_{i,j}}\left[\xi_{x_{i,j}}A2(1,1)+\xi_{y_{i,j}}A2(1,2)\right]-\frac{c_{b2}\tilde{v}_{i,j}}{\mathrm{Re}_{ref}\,\sigma\Delta\xi_{i,j}}\left[\xi_{x_{i,j}}A3(1,1)+\xi_{y_{i,j}}A3(1,2)\right]\geq0$$

Similar expressions are obtained for other the diffusion terms. (Details can be found in the Appendix.)

4. In the Spalart-Allmaras model, the nondimensional eddy viscosity μ_t is limited to be less than or equal to 100,000[47], corresponding intermediate variable $\tilde{v}$, is limited to between 10^{-20} and 2000.

5. The left hand side of the destruction was limited to be larger than zero. (Details can be found in the Appendix.)

4.4 Data-Theory Correlation

For the steady flow analysis the skin friction coefficient (C_f) and the steady surface pressure coefficient ($\overline{C}_p$) are defined as,

$$C_f = \tau_w/(0.5\rho_{in}V_{in}^2) \tag{4.4}$$

41

$$\overline{C}_p = (P_{in} - P)/(\rho_{in} V_{in}^2).$$ (4.5)

The expression for the skin friction coefficient (C_f) for the Blasius laminar boundary layer on a flat plate is

$$C_f = \frac{0.664}{\sqrt{\text{Re}_x}}$$ (4.6)

The power-law expression for the skin friction coefficient (C_f) for a turbulent boundary layer on a flat plate is[51]

$$C_f = \frac{0.027}{\text{Re}_x^{1/7}}.$$ (4.7)

Turbulent boundary layer non-dimensional parameters u^+, y^+ are defined as

$$u^+ = \frac{u_{\tan g}}{u_\tau} \qquad y^+ = \frac{y u_\tau}{\nu_w}$$ (4.8)

where $u_\tau = \sqrt{\tau_w / \rho_w}$

$u_{\tan g}$ is the tangential velocity along the streamwise direction,

τ_w is surface skin friction, $\mu \left. \dfrac{\partial u_{\tan g}}{\partial y} \right|_w$

ρ_w is the surface density

ν_w is the surface kinematic viscosity, μ_w / ρ_w

μ_w is the surface dynamic viscosity

From the 1930s, research workers had been attempting to provide a continuous formula for the variation of mean velocity in the vicinity of a smooth surface where, for simple shear flows, $u^+ = f(y^+)$. Immediately next to the wall, in the viscous sub-layer, the variation was assuredly linear and in the fully turbulent region for $y^+ > 30$ a logarithmic variation was accepted. But the region in between called the buffer layer, usually the

piecewise fits was employed to different segments of the region. It was not easy to come up with a single analytical expression for the whole universal velocity profile. Spalding[52] expressed the dimensionless distance y^+ as a function of the dimensional velocity u^+ (instead of the usual expression of writing u^+ in terms of y^+). It did have the correct asymptotic behavior (linear and logarithmic) at very small and very large values of u^+ and did represent the transition layer as well.

The experimental data correlation of Spalding[52] has the form,

$$y^+ = u^+ + e^{-\kappa B}\left[e^{\kappa u^+} - 1 - \kappa u^+ - \frac{\left(\kappa u^+\right)^2}{2} - \frac{\left(\kappa u^+\right)^3}{6} \right] \tag{4.9}$$

where, $B = 5.5$ and $\kappa = 0.4$.

For the unsteady flow analysis the first harmonic amplitude and phase angle using Fourier decomposition yields the unsteady surface pressure coefficient from the simulated unsteady flow field. The first harmonic unsteady surface pressure coefficient is defined in Equation (4.10).

$$C_p(x) = \frac{P_1(x)}{\rho_{in}V_{in}^2\alpha_1'} \tag{4.10}$$

In Equation (4.10) P_1 is the first harmonic surface pressure, and α_1' is the first harmonic of the airfoil pitching motion amplitude.

The unsteady surface pressure difference coefficient is the lower surface unsteady pressure coefficient minus the upper surface unsteady pressure coefficient as shown in Equation (4.11).

$$\Delta C_p(x) = (C_p(x))_{lower} - (C_p(x))_{upper} \tag{4.11}$$

The unsteady aerodynamic moment coefficient for airfoils pitching about mid-chord is defined by Equation (4.12),

$$C_M = \int_0^1 \left(\frac{x_{pitch}}{C} - \frac{x}{C} \right) \Delta C_p \left(\frac{x}{C} \right) d \frac{x}{C}$$ (4.12)

where C is the airfoil chord, and x_{pitch}/C is 0.5.

4.5 Work-per-Cycle and Work Impulse

4.5.1 Work-per-Cycle

The work done on the airfoil by the fluid per cycle of oscillation when the airfoil is oscillating in a pitching (torsion) motion is represented by the cyclic integral of the real part of moment times the real part of the differential pitching angle as shown in the equation below.[53]

$$W = \oint M_R d\alpha_R$$ (4.13)

Assuming sinusoidal torsional motion

$$\alpha = \bar{\alpha} e^{i\omega t},$$ (4.14)

the differentiation of Equation (4.14) gives

$$d\alpha_R = -\bar{\alpha} \sin \omega t\, d(\omega t)$$ (4.15)

where

α is complex,

$\bar{\alpha}$ is a real amplitude,

$\omega = 2\pi f$, and

f is the airfoil oscillation frequency.

Similarly, for the unsteady aerodynamic moment,

$$M = \overline{M} e^{i\omega t} = (\overline{M}_R + i\overline{M}_I)e^{i\omega t}$$ (4.16)

where both M and $\overline{M}$ are complex,

$$M_R = \overline{M}_R \cos \omega t - \overline{M}_I \sin \omega t$$ (4.17)

and $\bar{M}_R$ and $\bar{M}_I$ represents the real and imaginary parts of M, respectively.

Substituting Equation (4.15) and (4.17) into Equation (4.13) and carrying out the integration yields the following:

$$W = \pi \bar{\alpha} \bar{M}_I \tag{4.18}$$

This represents the aerodynamic work being done by the fluid on the airfoil over a cycle of vibration. A positive value indicates an instability. A negative value indicates a stable or damped motion.

4.5.2 Work Impulse

Equation (4.18) can be rewritten in coefficient form by dividing by $(1/2)\rho V^2 C^2$. This yields

$$C_W = \oint C_{M_R} d\alpha_R = \pi \bar{\alpha} C_{M_I} \tag{4.19}$$

where C_{M_I} is the imaginary part of C_M in Equation (4.12). The aerodynamic work-per-cycle is proportional to the imaginary part of the unsteady aerodynamic moment coefficient. $\mathrm{Im}(C_M) < 0$ indicates stability, and $\mathrm{Im}(C_M) > 0$ indicates instability. Hence, through examination of the integrand of the unsteady aerodynamic moment coefficient, localized areas of the airfoil can be identified that contribute to airfoil instability. The integrand of the unsteady aerodynamic moment coefficient is referred to as the Work Impulse ($\tilde{w}$) and defined as

$$\tilde{w}\left(\frac{x}{C}\right) = \left(\frac{x_{pitch}}{C} - \frac{x}{C}\right)\Delta C_p\left(\frac{x}{C}\right). \tag{4.20}$$

This type of information can be used to identify local flow physics with airfoil instability. Furthermore, designers can use this type of information to redesign unstable blades.

Chapter 5   Results

In this work, a flat plate and the NASA Transonic Flutter Cascade airfoil are investigated. Transitional flow simulations are performed as well as the fully turbulent flow calculations.

This investigation utilizes the Spalart-Allmaras[39] (SA) one-equation turbulence model and the Solomon, Walker and Gostelow[10] (SWG) transition model.   To investigate the influence of the transition onset location, three different transition onset models were implemented into the two-dimensional viscous flow solver.

For flat plate airfoil, the verification of the **NPHASE** code was done by solving the classical flat plate laminar, fully turbulent and transitional boundary layer flow. The numerical solutions are validated through the analytical (Blasius) solution and experimental data. The results will be presented on three different grids. Transition predictions will be presented with three transition onset models.   Two-dimensional grids are used with 221 grids in the axial direction and 121 grids in the circumferential direction (221x121).   To establish grid independency, results from the 221x121 grid are compared with results from a 361x161 grid and a 421x201 grid.

For the NASA-TFC GRC airfoil, calculations are made in steady flow and with the airfoils oscillating in a pitching motion about the mid-chord at 0° and 10° of chordal incidence angle, and correlated with experimental data. The operating conditions considered are an inlet Mach number of 0.5 and a Reynolds number of 0.9 Million.

Unsteady data will be presented for a 180° interblade phase angle (σ) and a reduced frequency ($k = \omega C / 2V_{in}$) of 0.4.   For low incidence angle and high incidence angle cases the airfoils are oscillated in a pitching (torsional) motion about the mid-chord at oscillation amplitude of 0.3° and 0.1° respectively.   All data-computation correlations are referenced by the experimental value of the chordal incidence and inlet Mach number.

5.1   Flat Plate Airfoil

Zero pressure gradient flat plate test cases were investigated to help insure that the SA and SWG models were correctly implemented in NPHASE.   Since this is a turbomachinery code, the flat plates were modeled as a cascade with zero stagger angle and a solidity of 0.1.   Calculations are presented for two different size grids. The coarse grid had 161 points in the flow direction and 60 points normal to the plate. Two refined grids with 198 grid points in the flow direction and 109 points normal to the plate, and 321 grid points in the flow direction and 120 points normal to the plate were also considered.

For the transitional flow calculations, solutions were first generated for fully turbulent flow using the SA model. These converged solutions were restarted with the SWG transition model activated to simulate transitional flow. Transition onset was predicted using the Suzen et al.[33] onset model with a turbulence intensity of 2.3% at the transition onset point (experimental value was 3% upstream of the flat plate). The transition calculations were compared to the T3A test case, which was one of a series of transitional flow test cases assembled by Savill[54].

5.1.1   Laminar flow

Laminar flow over a flat plate is a simple flow which has an analytical solution provided by Blasius, as shown in Equation(4.6). As the first step to validate the capability of **NPHASE**, laminar flow calculations were performed on multiple grids to make sure **NPHASE** is capable of resolving laminar portion of the transition flow.

Typically, the convergence of the solution can be determined by monitoring the lift coefficient changes with time step. When the lift coefficient does not change over time, the solution has reached steady state. The lift coefficient and the absolute value of the average density residual convergence history for 321x120 grid are presented in Figure 5.1 and Figure 5.2, respectively. From the figures, it is seen that the density residual is

less than 10^{-8} and the lift coefficient has stabilized. These are indications of a converged solution. These convergence indicators are typical of other grids in the laminar flow study.
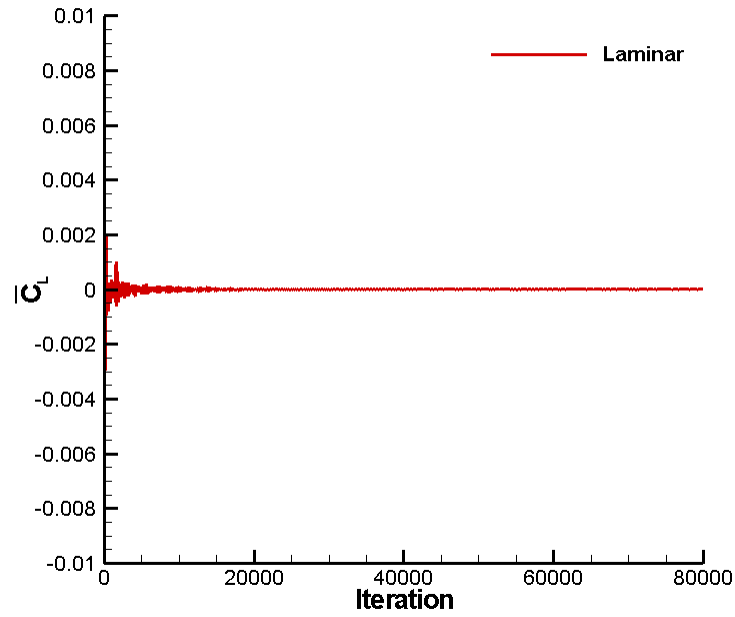
Figure 5.1 Lift coefficient as a function of time step for laminar flow (321x120 Grid)
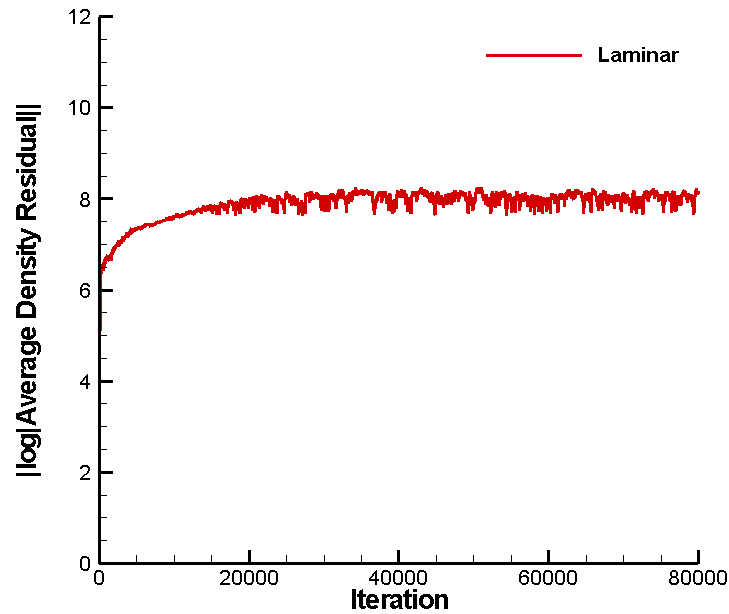
Figure 5.2 Absolute value of the average density residual as a function of time step for

laminar flow (321x120 Grid)

Figure 5.3 and Figure 5.4 show the skin friction coefficient calculation for the laminar flat plate results compared to the Blasius solution. Figure 5.3 shows the pressure surface has the same skin friction coefficient distribution as the suction surface due to the symmetrical geometry. Figure 5.4 shows the calculations performed on three different grids, 161x60, 198x109 and 321x120. As seen, the predictions have exceptional agreement with the Blasius analytical solution. These results indicate the 160x60 grid is sufficient for the computations with favorable computational accuracy and efficiency for this particular case. These results suggest that **NPHASE** is capable of resolving the laminar portion of transitional flow.

Figure 5.3 Flat plate skin friction coefficient prediction for laminar flow (161x60 Grid)
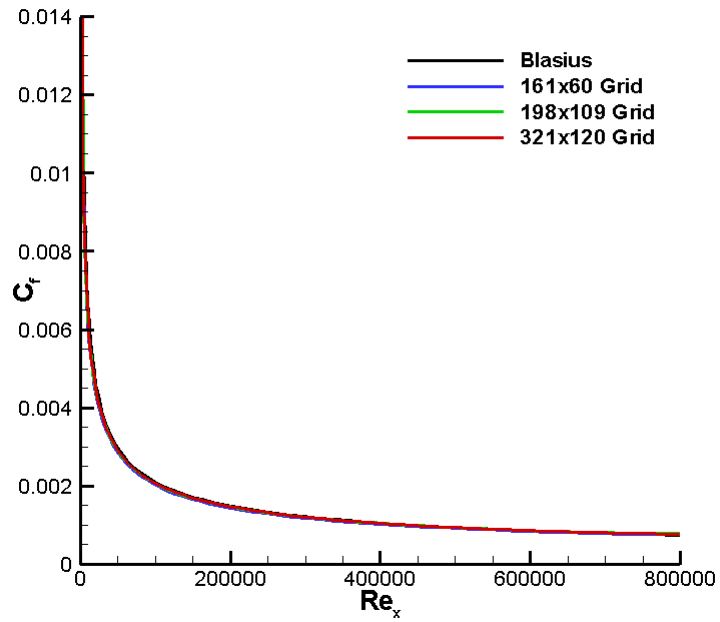
Figure 5.4 Flat plate skin friction coefficient prediction for laminar flow for three

different grid sizes

5.1.2 Turbulent flow

Figure 5.5 and Figure 5.6 present the lift coefficient and the absolute value of the average density residual convergence history for a flat plate with turbulent flow starting at the leading edge. These results indicate the solution has converged to steady state. The convergence history displayed in Figure 5.5 and Figure 5.6 are typical of the behavior exhibited by each grid used in the turbulent flat plate flow study.

Figure 5.5 Lift coefficient as a function of time step for fully turbulent flow (161x60 Grid)
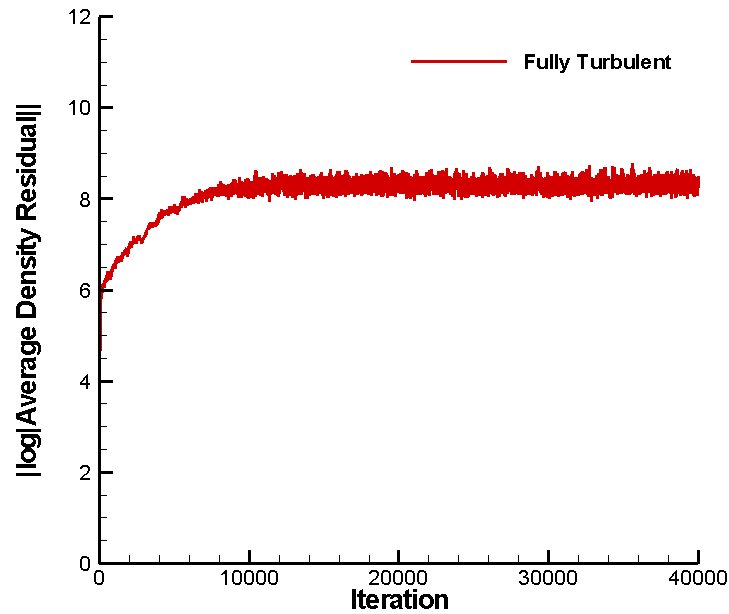
Figure 5.6 Absolute value of the average density residual as a function of time step for

fully turbulent flow (161x60 Grid)

Figure 5.7 illustrates the flat plate turbulent boundary layer non-dimensional u^+, y^+ (defined in Equation(4.8)) velocity profile parameters compared with the experimental data correlation of Spalding[52] (Equation(4.9)) for the three different flat plate grids. Figure 5.7 shows the prediction has very good correlation with the experimental data at the viscous sub-layer and fully turbulent out-layer region. Because of the Spalding correlation expression, the u^+ continues to increase while the numerical solution curves over to a constant value due to its reaching the freesteam region.
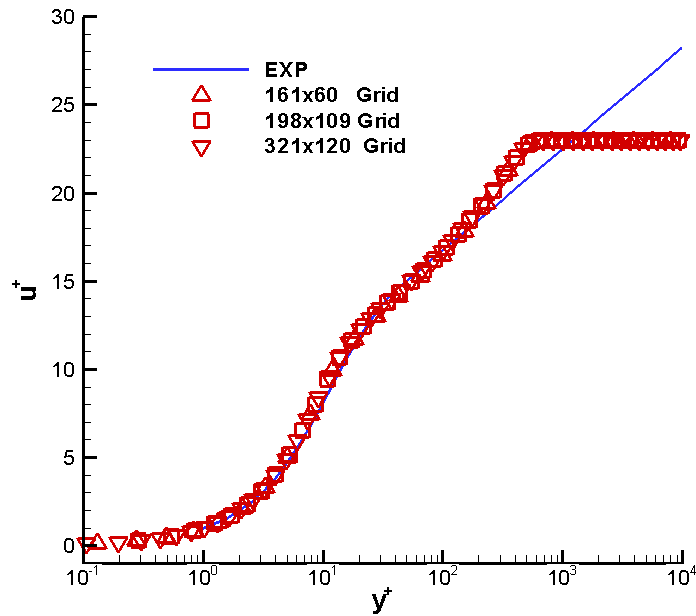
Figure 5.7 Flat plate turbulent boundary layer velocity profile ($Re_x = 720,000$)

The skin friction coefficient prediction of the fully turbulent flat plate results compared with the analytical power law expression (Equation (4.7)) are shown in Figure 5.8 and Figure 5.9. Figure 5.8 shows the pressure surface has the same skin friction coefficient distribution as the suction surface. Figure 5.9 shows the calculations performed on three different grids, 161x60, 198x109 and 321x120. As seen, the simulations slightly underpredict the analytical solution due to the approximation of the analytical expression and the accuracy of the turbulence model at low Reynolds numbers as well as a small Mach number effect for the compressible flow. Except for that, all three grids produce the same results.
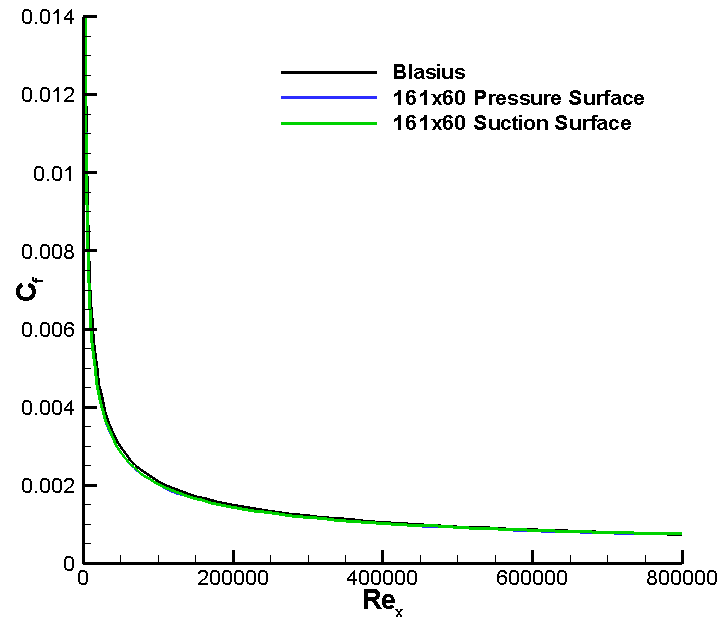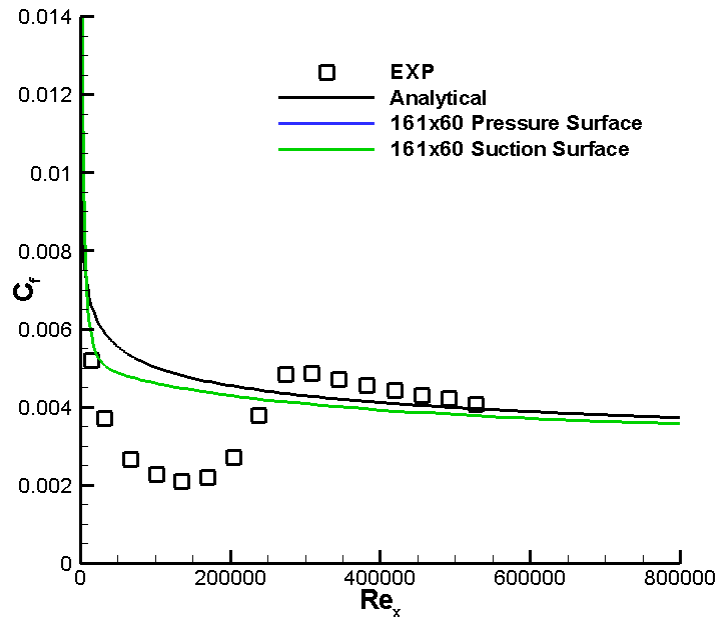
Figure 5.8 Flat plate skin friction coefficient prediction for turbulent flow (161x60 Grid)
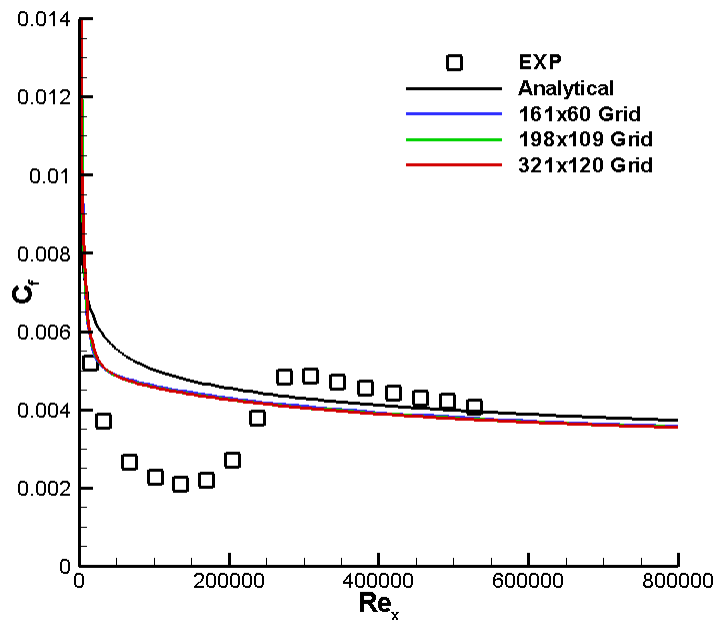
Figure 5.9 Flat plate skin friction coefficient prediction for turbulent flow using three

different grid densities

5.1.3   Transitional flow

The convergence histories for turbulent and transitional flow are displayed in Figure 5.10 and Figure 5.11. The results indicate the solution has converged to steady flow and are typical of the solutions found on all the grid densities used for flat plate transitional flow calculations. The discontinuity between the fully turbulent and transition is generated when the transition computation is restarted from the fully turbulent solution, and a flow field perturbation is introduced to the system by the effect of the intermittency factor. After a short period, the transition density residual is converged to be less than 10^{-8}.
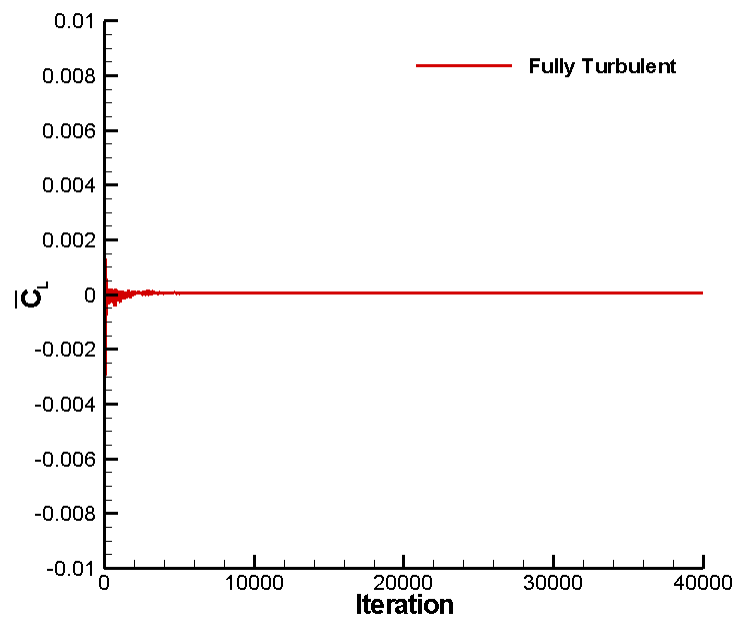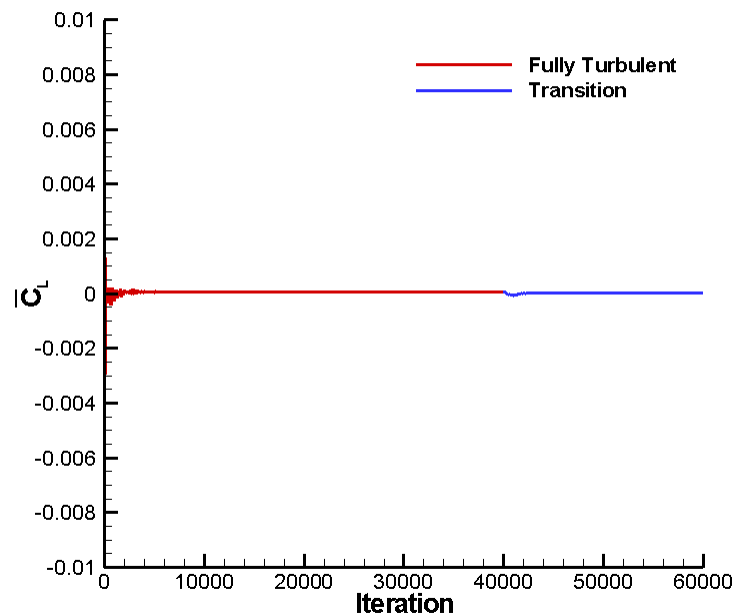

Figure 5.10 Lift coefficient as a function of time step for turbulent and transitional flow
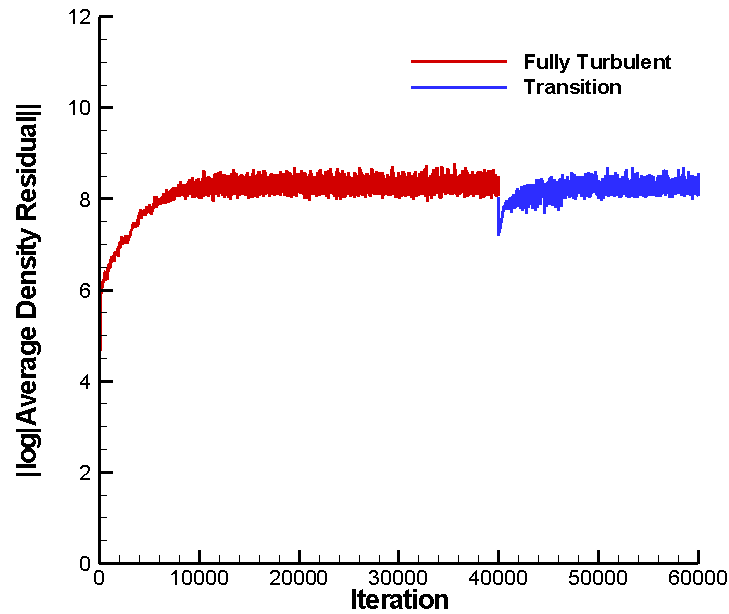
(161x60 Grid)

Figure 5.11 Absolute value of the average density residual as a function of time step for transitional flow (161x60 Grid)

The momentum thickness Reynolds number (Re_θ) as a function of streamwise distance Reynolds number (Re_x) using Steelant and Dick (SD) and Suzen et al.(SH) transition onset models for different grid sizes are shown in Figure 5.12. The momentum thickness Reynolds number for SD and SH onset models agree with the experimental data in the laminar region. After the transition onset location, there is deviation from the experimental data. From Figure 5.12 and Figure 5.13, the Steelant and Dick onset model predicts a transition onset point too close to the flat plate leading edge. The Re_θ value from this correlation is too large for the onset point resulting in earlier transition. The Suzen et al. onset model is better than the Steelant and Dick onset model. The earlier the transition onset location, the quicker the laminar flow will turn into fully turbulent flow, and the shorter the transition length.
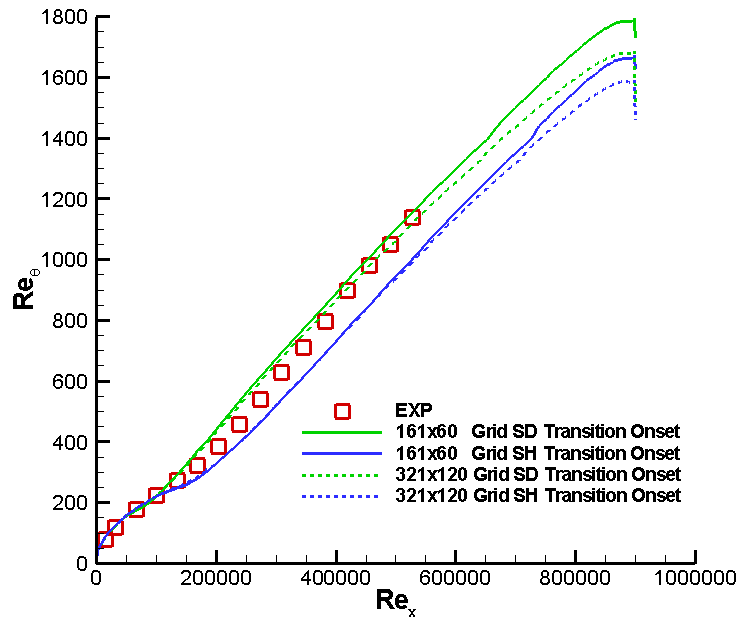
Figure 5.12 Momentum thickness Reynolds number as a function of streamwise distance Reynolds number

Figure 5.13 shows the skin friction coefficient prediction of the transitional flat plate results with Steelant and Dick and Suzen et al. transition onset models on two different grids, 161x60 and 321x120.   As seen, the Steelant and Dick transition onset model predicted the transition onset location earlier than the Suzen et al. onset model, and results in a shorter transition length. The laminar portion, transition onset location, and transition end location are illustrated in Figure 5.13.
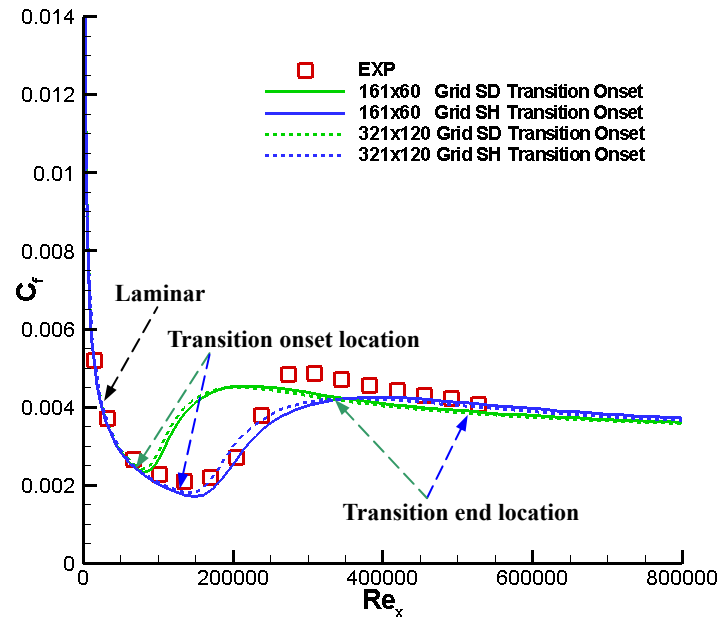
Figure 5.13 Flat plate skin friction coefficient prediction for transitional flow using two different grid densities

Figure 5.14 is an example of the variation of the intermittency function in the transition region of the flat plate for 161x60 and 321x120 grids. The local Reynolds number represents the distance along the plate. The intermittency function is zero for $Re_x < 150,000$ in the laminar flow region. The intermittency function then increases from 0 to 1 as the flow undergoes transition to turbulent flow. After the transition zone, the intermittency function remains as 1 indicating the fully turbulent region. There is only a slight difference between these two grids due to the difference of the grid resolution.
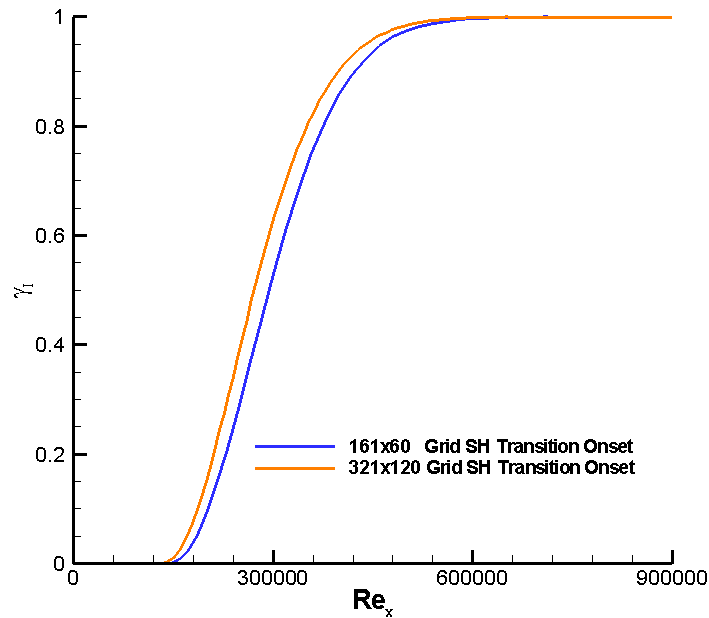
Figure 5.14 An example of the variation of the intermittency function in the transition region of the flat plate

Also the fixed transition onset model is tested with the transition onset location at 12.6% of chord ($Re_x = 113,400$).   The results for this onset location are shown in Figure 5.15.   The local Reynolds number represents the distance along the plate.   The experimental data and the predictions decrease for $Re_x < 113,400$ in the laminar flow region.   The skin friction then increases as the flow undergoes transition to turbulent flow. Downstream of the transition region, the skin friction coefficient decreases with further increase in Re_x as expected for turbulent flow.   Even though there are some experimental data missing in the transition region, the experimental data and computational predictions have the same trends.   The predicted increase in the skin friction, however, does not reach the peak value found for the experimental data. The two computational grids used have excellent agreement with each other.
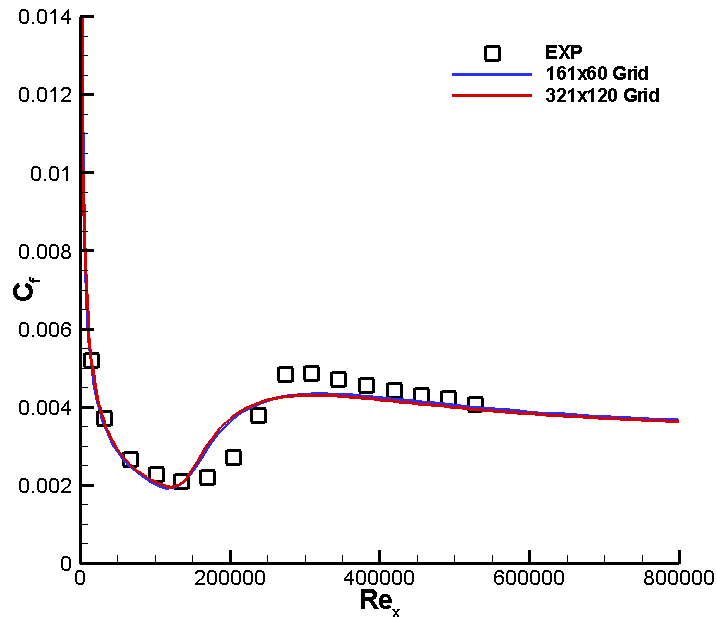
Figure 5.15 Flat plate skin friction coefficient prediction for transitional flow for a fixed transition onset location of $x_t = 0.126C$

5.2 NASA/P&W Airfoil

The airfoil used in this investigation had a cross-section typical of modern high performance low aspect ratio fan or compressor blades in aircraft gas turbine engines. In order to match the inlet Mach number and flow angle, the pressure ratio $(P_{outlet}/P_{inlet,stagnation})$ had to be adjusted. The pressure ratio was varied until the best match was found for the freestream Mach number (0.5) and incidence angle. An example of the procedure to find the pressure ratio is shown in Table 5.1 for the low incidence angle condition.   For this case, the inlet Mach number is 0.5, and the angle-of-attack, $\bar{\alpha}$, is 1°. The pressure ratio was found to be 0.7755220.

Table 5.1 Pressure ratio convergence for NASA/P&W airfoil at the low incidence angle operation condition

Iteration	$Mach_{in}$	$\bar{\alpha}_{input}$	Pressure ratio	$Mach_{out}$	$\bar{\alpha}_{output}$
1	0.5	1.0	0.7759866	0.499915	1.014558
2	0.5	1.0	0.7750000	0.500093	0.984146
3	0.5	1.0	0.7755143	0.500000	0.999978
4	0.5	1.0	0.7755150	0.500001	0.999785
5	0.5	1.0	0.7755142	0.500001	0.999761
6	0.5	1.0	0.7755222	0.500000	1.000007
7	0.5	1.0	0.7755219	0.500000	0.999997
8	0.5	1.0	0.7755220	0.500000	1.000001

Once the pressure ratio is determined and the steady flow field calculated, the unsteady solution sequence for pitching motion can be initiated. In this investigation, the experimental data from Buffum et al.[31] was used.

5.2.1 Steady Turbulent flow ($\bar{\alpha} = 0^\circ$)

The cascade inlet flow angle was not measured in the experiment but quoted as the geometric value determined from the cascade geometry. In order to conduct the computation, the inlet flow angle had to be determined. The cascade inlet flow angle was varied until the best match was found between the steady chordwise pressure coefficient data ($\overline{C_p} = (P_{in} - P)/(\rho_{in} V_{in}^2)$) and the predictions. This resulted in a 1° chordal incidence angle being used in all the presented low incidence angle solutions. Computations were conducted on three grids.   The grid sizes were 221x121, 361x161, and 421x201.   The lift coefficient and the absolute value of the average density residual convergence history are presented in Figure 5.16 and Figure 5.17, respectively, for the 421x201 grid.

Figure 5.16 Low incidence angle lift coefficient as a function of time step for fully

turbulent flow (421x201 Grid)

Figure 5.17 Low incidence angle absolute value of the average density residual
convergence history for fully turbulent flow (421x201 Grid)

From the figures, it is seen that the density residual is less than 10^{-9} and the lift coefficient has stabilized. The results indicate the solution has converged to steady flow and are typical of the solutions found on all the grid densities used for NASA/P&W fully turbulent flow calculations.

Figure 5.18 presents the correlation of the predicted fully turbulent steady surface pressure coefficient with the experimental data. There is good correlation of the predictions with the experimental data. The leading edge region presented in Figure 5.19 shows the 221x121 grid gives a slightly higher pressure coefficient in the suction peak region. The predicted reattachment point for the three grids is given in Table 5.2. For all grids, a small suction surface separation bubble was predicted in the leading edge region. The reattachment point is at 4.1%, 4.8% and 4.3% of chord, respectively. The difference is less than 1%. The separation bubble, which is indicated by the negative value of ρu, can also be seen in the ρu contour plot of Figure 5.20. The separation zone was not measured in the experiment for low incidence angle operating condition.
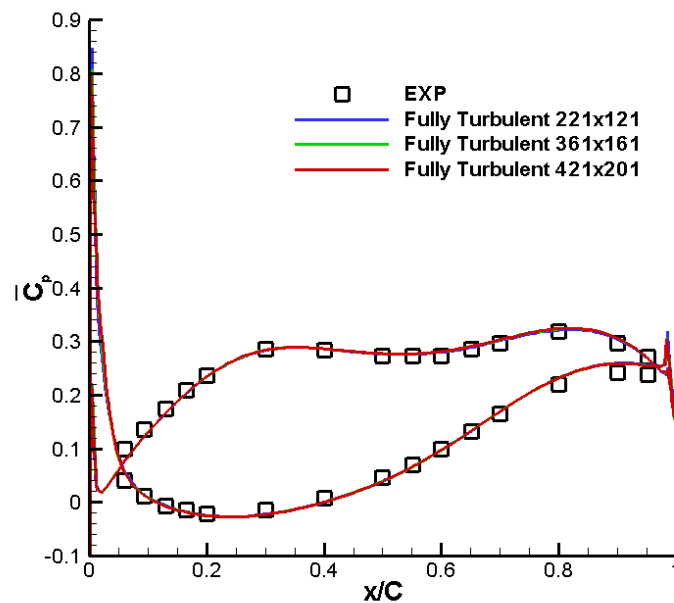
Figure 5.18 Low incidence angle airfoil surface pressure coefficient distribution for fully turbulent flow
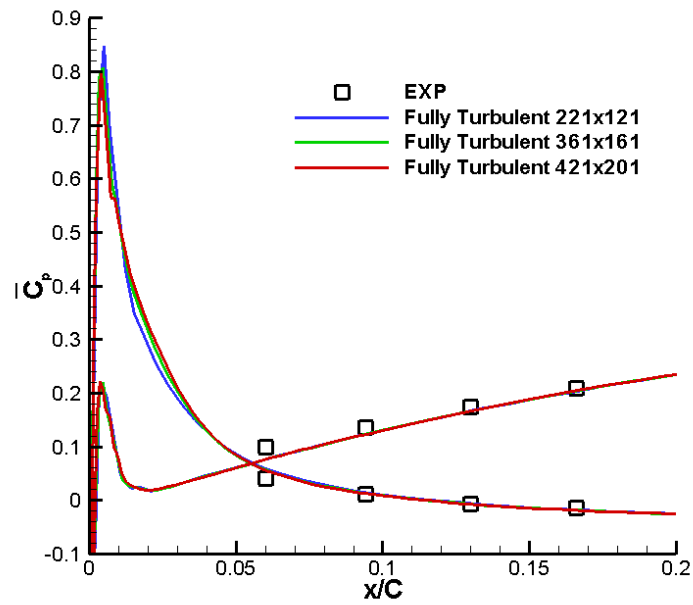
Figure 5.19 Low incidence angle airfoil surface pressure coefficient distribution in the leading edge region for fully turbulent flow
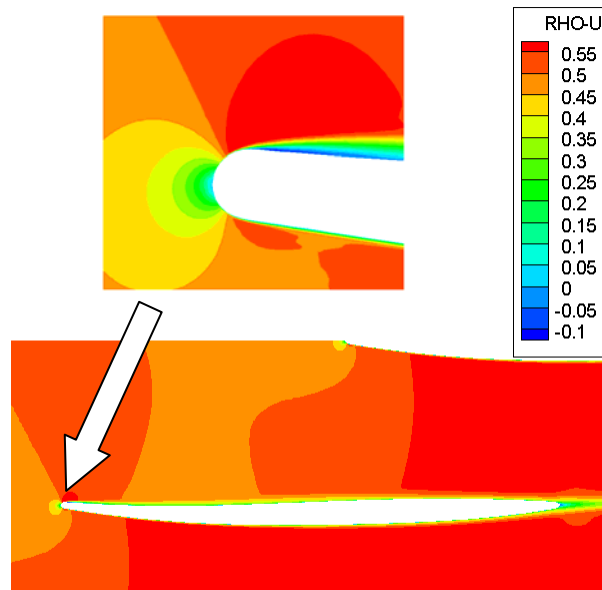
Figure 5.20 Contours of ρu at 0º chordal incidence showing the leading edge separation bubble for fully turbulent flow (361x161 Grid)

5.2.2   Steady Transitional flow ($\bar{\alpha} = 0^\circ$)

Once the steady fully turbulent state is reached, the transition predictions are performed based on the fully turbulent solution with the same chordal incidence angle, pressure ratio, and freestream Mach number. Computations were conducted on the same three grids.   Three transition onset models along with SWG transition model were used in the transitional computation. The transition onset models used were Suzen et al., Praisner and Clark, and the fixed transition onset model. The lift coefficient and the absolute value of the average density residual convergence history combined with the fully turbulent solution are presented in Figure 5.21 and Figure 5.22, respectively.
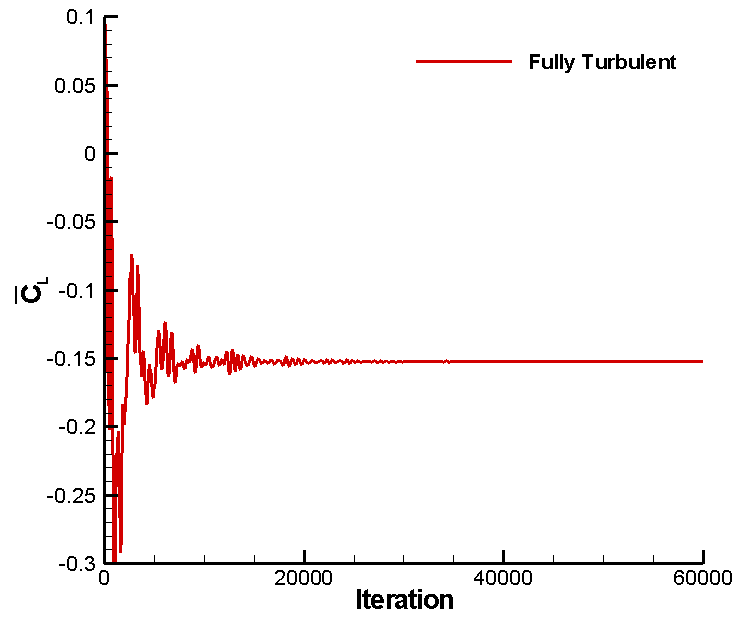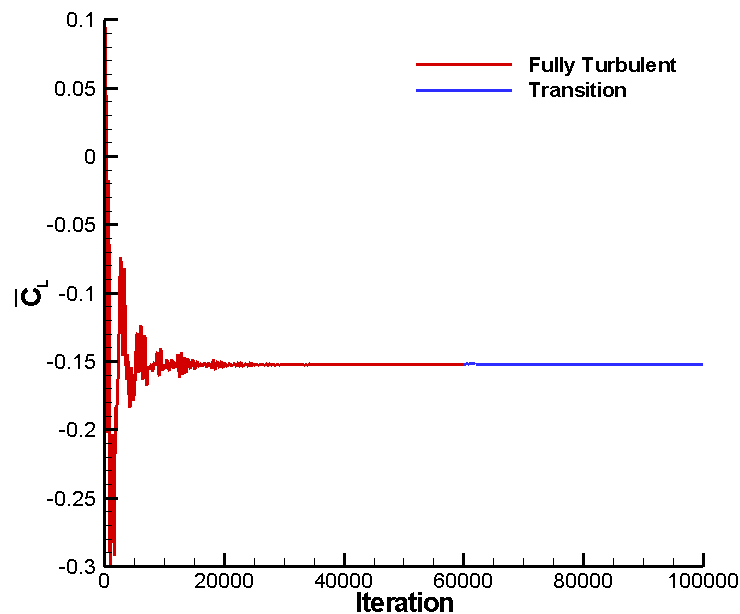

Figure 5.21 Low incidence angle lift coefficient as a function of time step for turbulent and transitional flows (421x201 Grid)
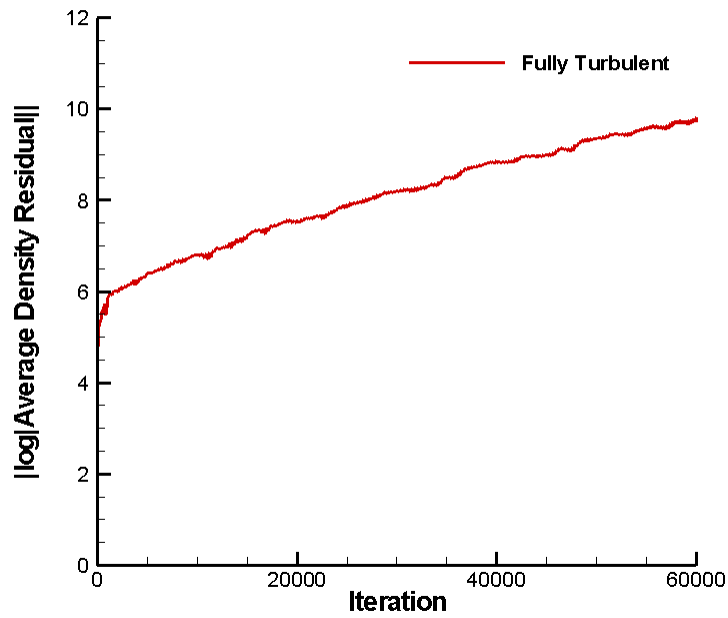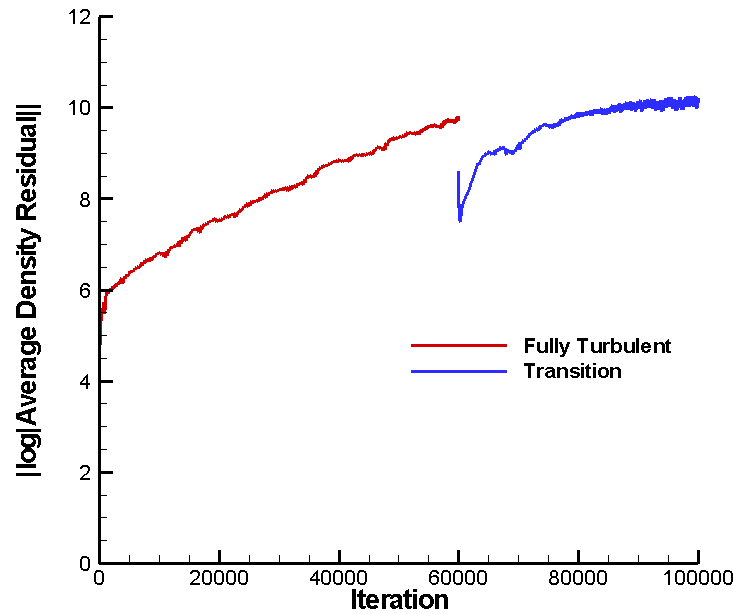
Figure 5.22 Low incidence angle absolute value of the average density residual
convergence history for turbulent and transitional flows (421x201 Grid)

From the figures, it is seen that although there is a discontinuity when the transition computation is restarted from the fully turbulent solution due to the induced flow field perturbation, the transition density residual finally managed to be less than 10^{-10} and the lift coefficient also stabilized. These results indicate that the solution has reached steady state.

Figure 5.23 shows an example of the variation of the intermittency function in the transition region of the NASA-TFC airfoil for the 421x201 grid using the fixed transition onset model with a transition onset location at 1.5% of the chord. From this figure, it is seen that transition starts very close to the leading edge on suction surface of the airfoil, whereas the transition starts further downstream on pressure surface of the airfoil. The intermittency factor grows from 0 to 1 more rapidly on the suction surface than on the pressure surface.
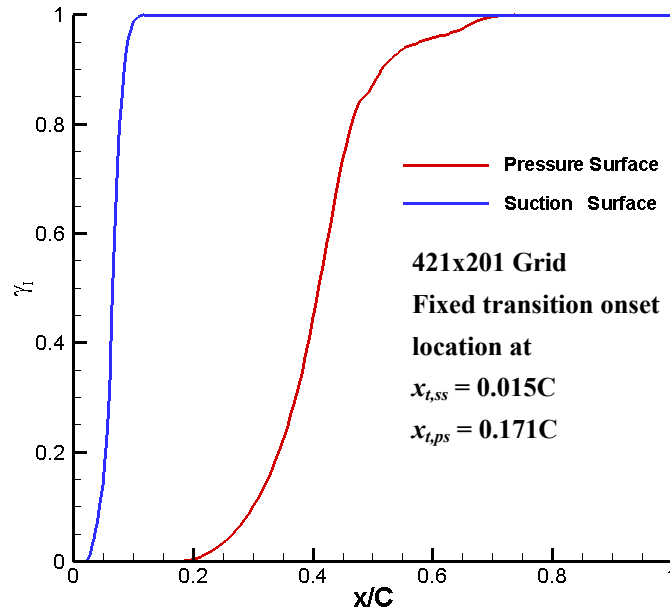
Figure 5.23 An example of the variation of the intermittency function in the transition region of the NASA-TFC airfoil for the low incidence angle condition

Figure 5.24, Figure 5.25 and Figure 5.26 present the correlation of the predicted leading edge region transitional steady surface pressure coefficient with the experimental data. The predicted transition onset point, transition length, separation point, and reattachment point for the three grids are given in Table 5.2 for the transition solution.

Figure 5.24 is the transition solution using Suzen et al.'s transition onset model. For the 361x161 and 421x201 grids, the predicted transition onset points are the same at 2% chord, whereas the transition onset point is at 2.7% of chord for the relatively small size grid. The farther downstream transition onset results in a longer transition length and a smaller pressure coefficient for the pressure plateau as is shown in Table 5.2 and Figure 5.24. Results from the three grids all agree with the experimental data. A small suction surface separation bubble was predicted in the leading edge region. When the experiments were conducted, flow visualization was not done because the pressure distributions did not raise any suspicion of flow separation in the leading edge region.

67

Furthermore, there is no experimental data available in the transition region for the low incidence angle condition, which would indicate whether the transition solutions obtained are better than the fully turbulent solution, due to instrumentation limitations caused by the airfoil thickness in this area. From Figure 5.24, the two larger grids agree with each other.

Figure 5.24 Low incidence angle airfoil surface pressure coefficient distribution for transitional flow using the Suzen et al. transition onset model

Figure 5.25 is the transition solution using the Praisner and Clark transition onset model. Compared with the Suzen et al. transition onset model for the same grid size, the transition onset point starts earlier than the Suzen et al. onset model. So, it results in a shorter transition length. The difference between Suzen et al. transition onset model and Praisner and Clark transition onset model is that Suzen et al. uses turbulence intensity and momentum thickness Reynolds number at separation point to calculate the Reynolds number based on the separation to transition onset length ($\mathrm{Re}_{st} = 874\,\mathrm{Re}_{\theta s}^{0.71}\,\exp[-0.4Tu]$),

while Praisner and Clark use the Reynolds number at separation point and momentum thickness Reynolds number calculate the same parameter ($\mathrm{Re}_{st} = 173 \, \mathrm{Re}_s \, \mathrm{Re}_{\theta s}^{-1.227}$).   It does not include the *Tu* as a parameter. Both of the transition onset models used for the separated flow.   Results from the three grids all agree with the experimental data. The two larger grids (361x161 and 421x201) agree with each other.
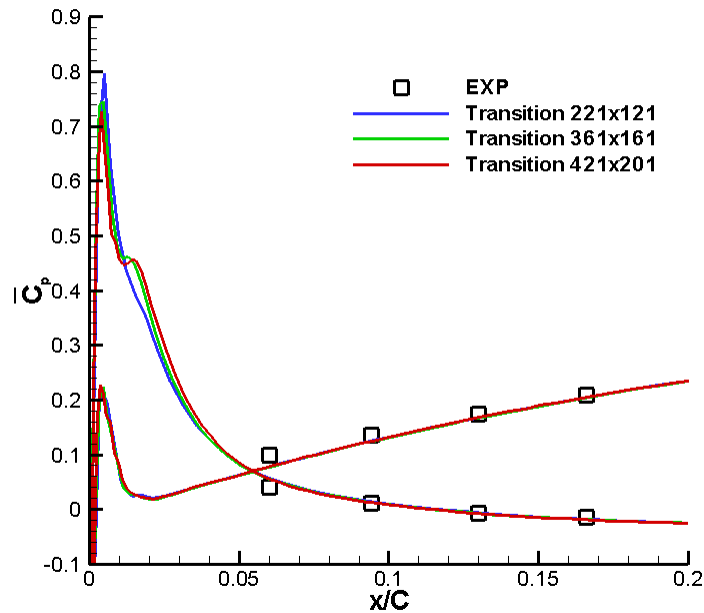
Figure 5.25 Low incidence angle airfoil surface pressure coefficient distribution for transitional flow using the Praisner and Clark transition onset model

Suzen et al. and Praisner and Clark transition onset model results show that if the transition onset location is too close to the leading edge, the transitional pressure coefficient distribution would be more like fully turbulent pressure coefficient distribution. If the transition onset location too far downstream, the solution becomes unstable. From Suzen at al. and Praisner and Clark transition onset model predictions, the solutions were stable with the onset location at 0.02C and 0.013C, respectively (see Table 5.2).

In order to test the fixed transition model on a stable solution, the transition onset location of $x_{t,ss} = 0.015C$ on the suction surface was selected. Figure 5.26 is the transition solution using the fixed transition onset model with transition onset at $x_{t,ss} = 0.015C$ on the suction surface.   The same trend is found for the fixed transition onset model results that the earlier transition onset point generates a shorter transition length. Unstable results were found with the transition onset point larger than 0.03C.   The predicted reattachment point for three grids are very close, as shown in Table 5.2, with the differences within 0.004C.
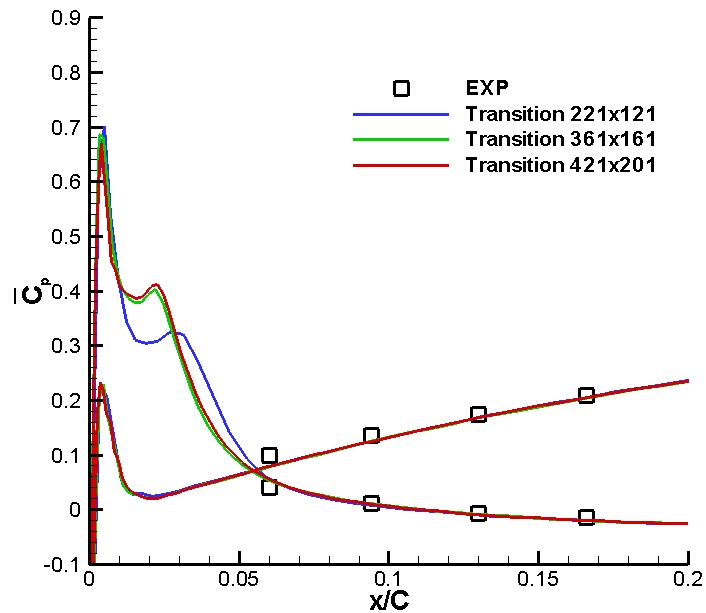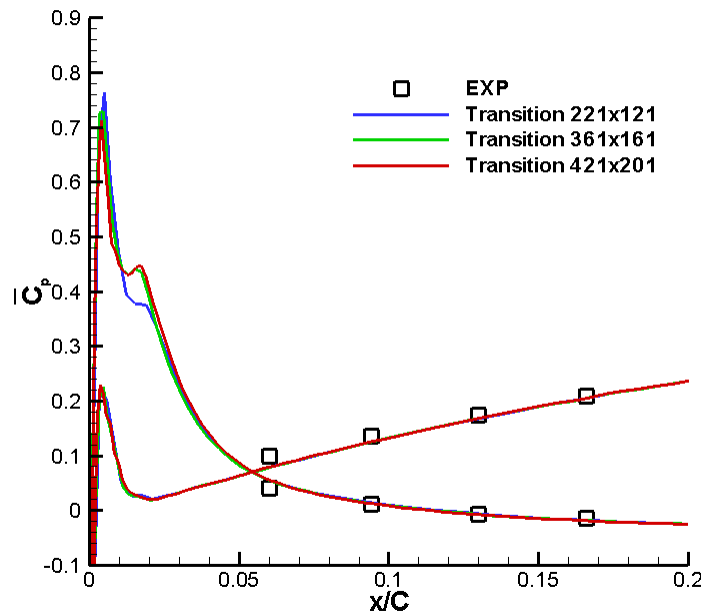

Figure 5.26 Low incidence angle airfoil surface pressure coefficient distribution for transitional flow using the fixed transition onset model with $x_{t,ss} = 0.015C$

As found for the fully turbulent simulations, a small suction surface separation bubble was formed in the leading edge region. The predicted reattachment points for the 221x121, 361x161 and 421x201 grids were 4.1%, 4.3% and 4.3% of chord, respectively.

The ρu contour plots of transitional flow on the 361x161 grid using Suzen et al. transition onset model is shown in Figure 5.27.   As a comparison, leading edge ρu

contour plots showing the separation bubble of fully turbulent and transitional flow using the Suzen et al. transition onset model are shown in Figure 5.28. Although the fully turbulent and transitional flows have almost the same bubble length in the leading edge, the bubble height in transitional flow (0.1% of chord) is higher than it is in fully turbulent (0.04% of chord).
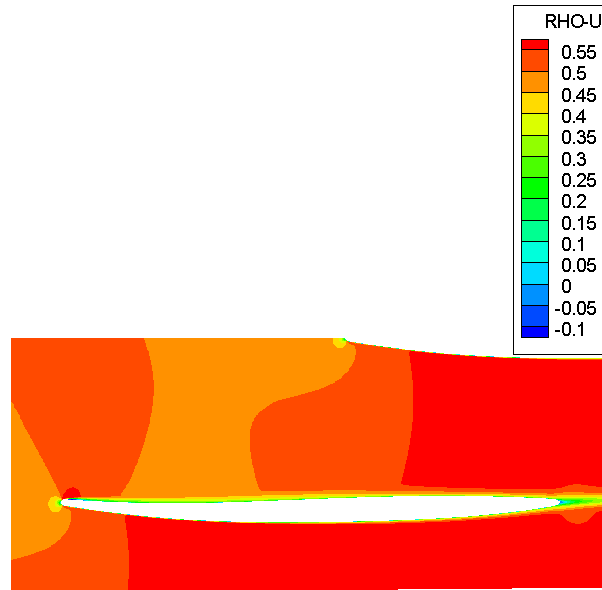
Figure 5.27 Contours of ρu at 0º chordal incidence showing the separation bubble for transitional flow on the 361x161 grid using the Suzen et al. transition onset model
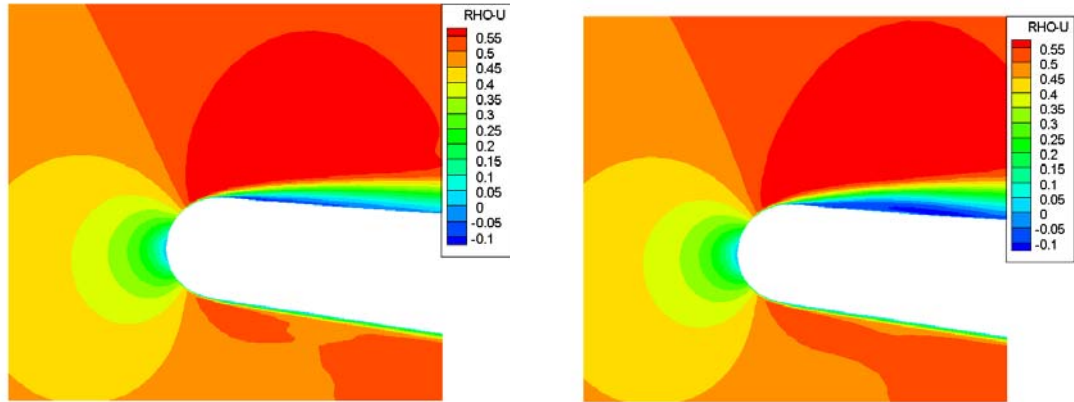
(a) fully turbulent flow   (b) transitional flow

Figure 5.28 Leading edge contours of ρu at 0º chordal incidence showing the separation bubble on the 361x161 grid using the Suzen et al. transition onset model

From all the transition results, it is seen that the transition zone starts and ends within the separation bubble. In the separated flow region, the transition calculations deviated substantially from the turbulent calculation. The separation bubble near the leading edge region results in a change of the pressure gradient. The SWG transition model predicted a pressure plateau in this area while the fully turbulent failed to do so.

On the pressure surface the transition onset model of Steelant and Dick was used. This yielded a transition onset point of 0.25C. For the fixed transition point investigation, the pressure surface transition onset point was set to 0.17C. The changes made to the suction surface transition onset point did not have any effect on the pressure surface pressure coefficient. Moreover, no significant change in the pressure coefficient on the pressure surface was observed for the change in the pressure surface transition onset location. The pressure distribution for transitional flow on the pressure surface is very similar to the fully turbulent solution. But the solution was very sensitive to transitional flow in suction surface separation bubble.

Table 5.2 Fully turbulent and SWG transition parameters for the low incidence angle condition

Transition Onset Model	$x_{ss,t}$	Transition Length	Separation Point	Reattachment Point
None, Fully Turbulent				
221x121	NA	NA	0.007C	0.041C
361x161	NA	NA	0.010C	0.048C
421x201	NA	NA	0.006C	0.043C
Suzen et al.				
221x121	0.027C	0.026C	0.007C	0.041C
361x161	0.020C	0.010C	0.006C	0.043C
421x201	0.020C	0.011C	0.006C	0.043C
Praisner and Clark				
221x121	0.011C	0.020C	0.007C	0.041C
361x161	0.013C	0.009C	0.006C	0.043C
421x201	0.013C	0.010C	0.006C	0.043C
Fixed Transition				
221x121	0.015C	0.021C	0.011C	0.045C
361x161	0.015C	0.007C	0.010C	0.048C
421x201	0.015C	0.008C	0.010C	0.052C

5.2.3 Steady Turbulent flow ($\bar{\alpha} = 10^{\circ}$)

The cascade inlet flow angle was varied until the best match was found between the steady chordwise pressure coefficient data and the predictions. This resulted in a 7.5° chordal incidence angle being used in all the presented high incidence angle solutions. Also, the pressure ratio ($P_{outlet}/P_{inlet, stagnation}$) was varied until the best match was found

for the freestream Mach number (0.5) and incidence angle. Computations were conducted on the same three grids used for the low incidence angle condition. The lift coefficient and the absolute value of the average density residual convergence history are presented in Figure 5.29 and Figure 5.30, respectively, for the 421x201 grid.

Figure 5.29 High incidence angle lift coefficient as a function of time step for fully turbulent flow (421x201 Grid)

Figure 5.30 High incidence angle absolute value of the average density residual

convergence history for fully turbulent flow (421x201 Grid)

Flow visualization at midspan in the cascade indicated the flow was separated from the leading edge to about 40% of chord. The predicted reattachment point for the three grids is given in Table 5.3, which includes the results for the transitional flow calculations.

Figure 5.31 presents the correlation of the predicted fully turbulent steady surface pressure coefficient with the experimental data. The pressure distribution on the suction surface deviates from the experimental data near the leading region. Other than that, there is good correlation of the predictions with the experimental data. The leading edge region in Figure 5.32 shows the 221x121 grid gives a slightly higher pressure coefficient in the suction peak region.

A large suction surface separation bubble was calculated to form in the leading edge region. For the 221x121, 361x161 and 421x201 grids, the flow separates almost at the same place (0.5%, 0.5% and 0.4% of chord) and reattaches at 41.6%, 43.2% and 44%

75

of chord, respectively. The high incidence angle case has a larger separation bubble than the low incidence angle case. The separation bubble can also be seen in the *ρu* contour plot of Figure 5.33. There was no separation bubble predicted on the pressure surface.
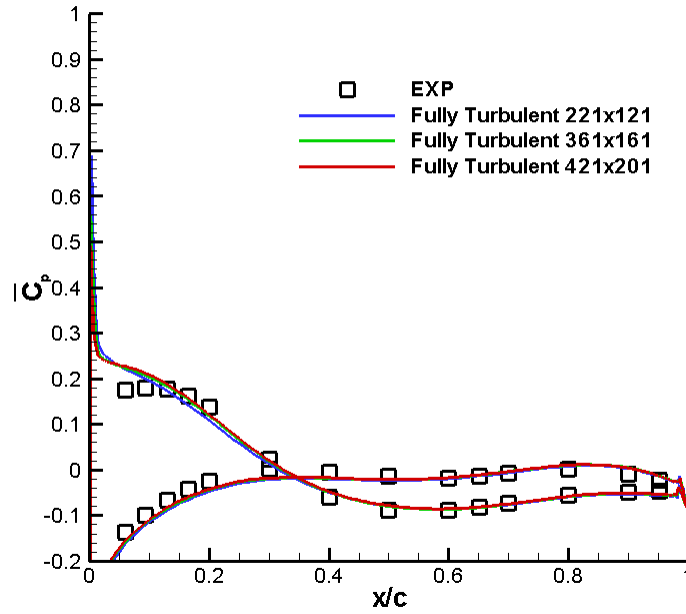
Figure 5.31 High incidence angle airfoil surface pressure coefficient distribution for fully turbulent flow

Figure 5.32 High incidence angle airfoil surface pressure coefficient distribution in the
leading edge region for fully turbulent flow
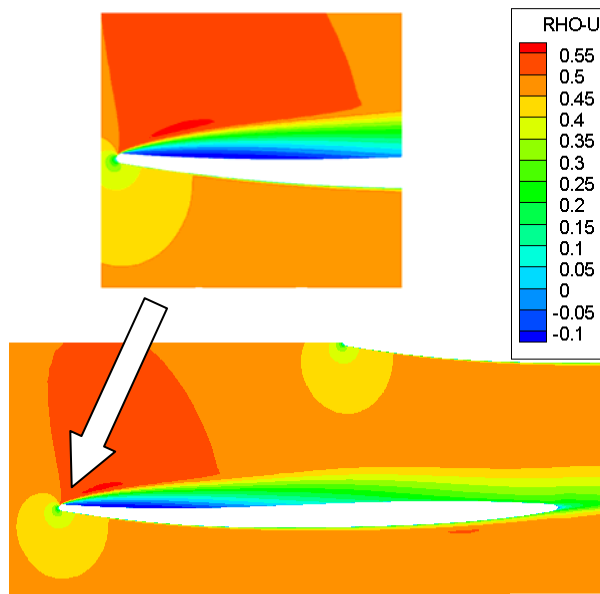
Figure 5.33 Contours of ρu at 10º chordal incidence showing the separation bubble for
fully turbulent flow (361x161 Grid)

5.2.4   Steady Transitional flow ($\bar{\alpha} = 10^o$)

The transition predictions were performed based on the fully turbulent solution with the same chordal incidence angle pressure ratio and freestream Mach number. Computations were conducted on the same three grids.   Three transition onset models along with the SWG transition model were used in the transitional computation. The transition onset models used in this investigation were Suzen et al., Praisner and Clark, and specified x/C location. The lift coefficient and the absolute value of the average density residual convergence history combined with the fully turbulent solution are presented in Figure 5.34 and Figure 5.35, respectively.
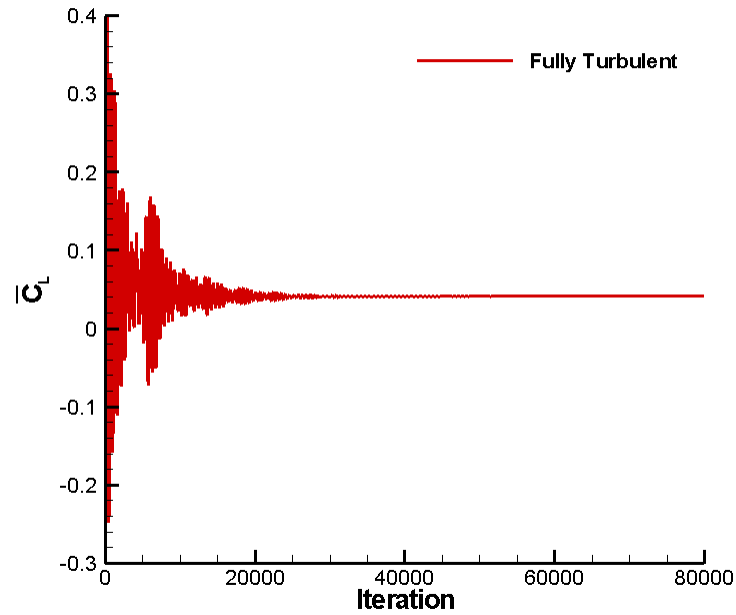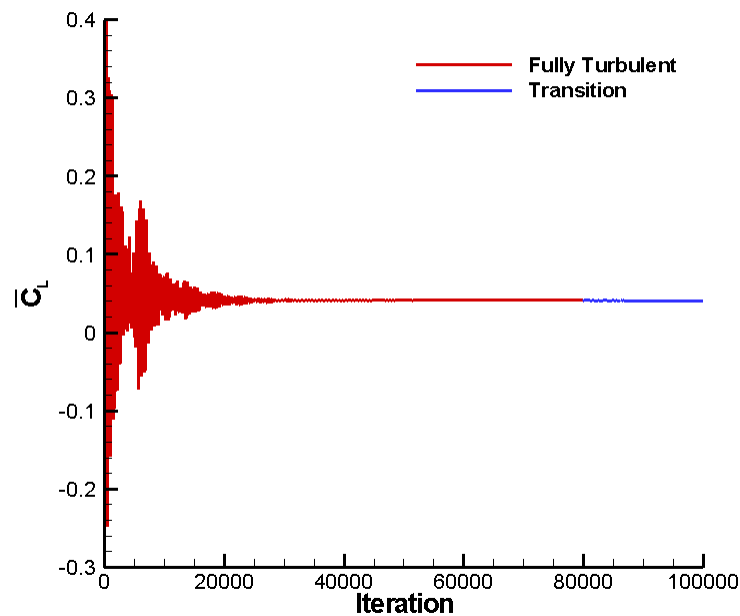

Figure 5.34 High incidence angle lift coefficient as a function of time step for turbulent and transitional flows (421x201 Grid)
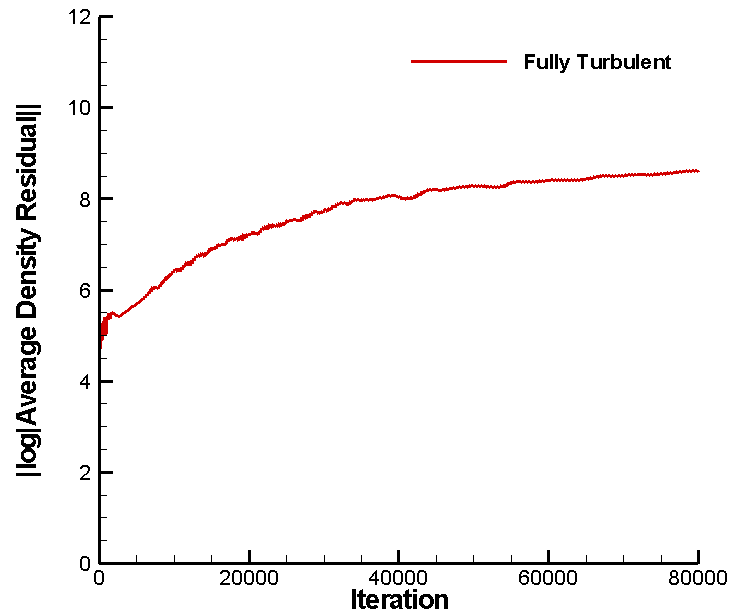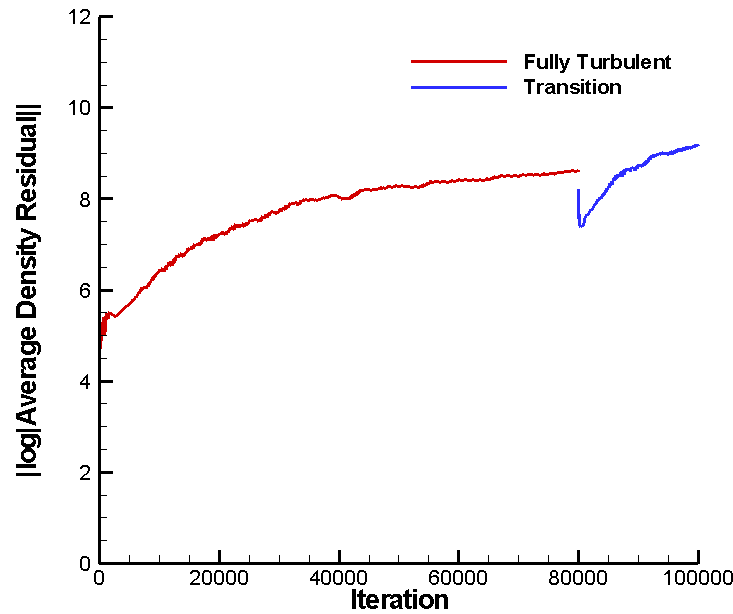
Figure 5.35 High incidence angle absolute value of the average density residual

convergence history for turbulent and transitional flows (421x201 Grid)

From the figures, the transition computation is restarted from the fully turbulent solution. After a discontinuity from the fully turbulent due to the induced flow field perturbation, the transition density residual is stabilized at less than 10^{-9} and the lift coefficient also stabilized. These results indicate the solution has converged.

Figure 5.36 and Figure 5.37 present the correlation of the predicted transitional steady surface pressure coefficient using the Suzen et al. transition onset model with the experimental data. For the 221x121, 361x161 and 421x201 grids, the predicted transition onset point is at 2.2%, 2% and 1.6% of chord, respectively. The differences are less than 1%. The farther downstream transition onset point yields a longer transition length and a smaller pressure coefficient for the pressure plateau as is shown in Table 5.3. The predicted reattachment point for the 221x121, 361x161 and 421x201 grids is at 41.6%, 43.2% and 44% of chord, respectively. The pressure plateau length is less than the

pressure plateau length exhibited by the experimental data. The calculated pressure plateau is also higher than the experimental data.

Figure 5.36 High incidence angle airfoil surface pressure coefficient distribution for transitional flow using the Suzen et al. transition onset model

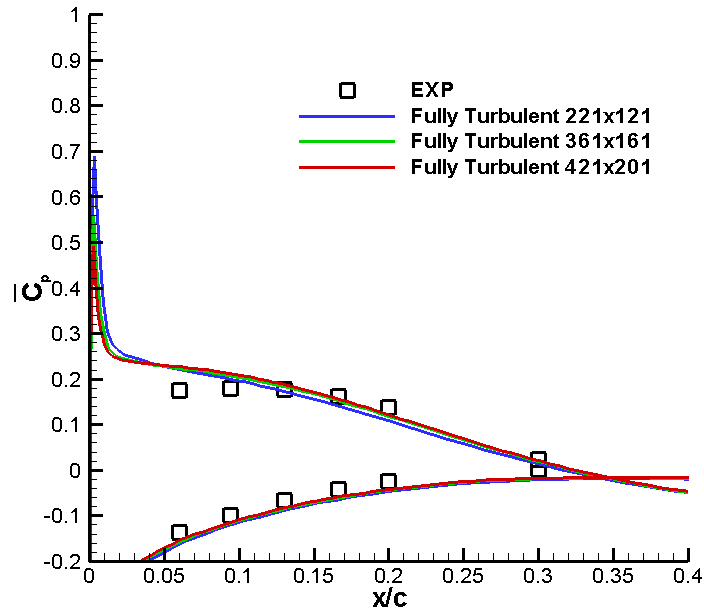Figure 5.37 High incidence angle airfoil surface pressure coefficient distribution in the leading edge region for transitional flow using the Suzen et al. transition onset model

Figure 5.38 and Figure 5.39 is the transition solution with Praisner and Clark transition onset model. Compared with Suzen et al. transition onset model for the same grid size, the transition onset point starts earlier than the Suzen et al. onset model and has a shorter transition length which are also shown in Table 5.3. The same trend is found for the fixed transition onset model predictions, as will be discussed later.

The SWG transition model with the Praisner and Clark transition onset model does not show much difference from the fully turbulent predicted pressure coefficient.   This is a result of the transition onset point being close to the leading edge and the transition region not extending very far into the separation zone.
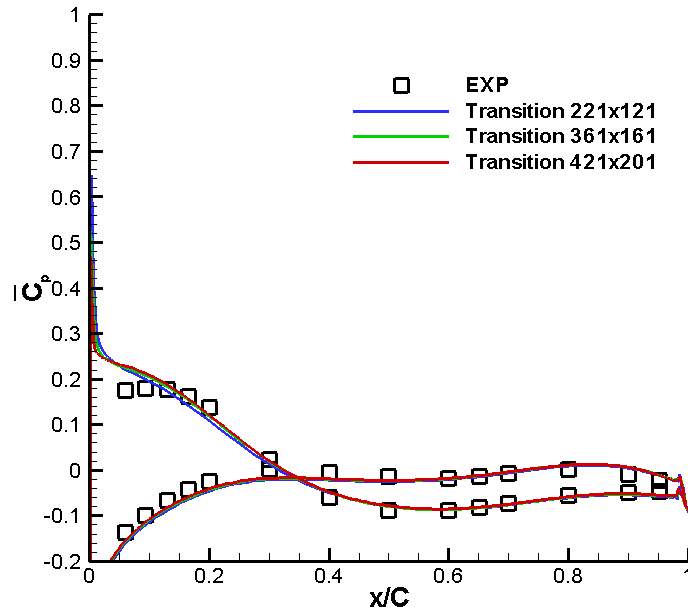
Figure 5.38 High incidence angle airfoil surface pressure coefficient distribution for transitional flow using the Praisner and Clark transition onset model

Figure 5.39 High incidence angle airfoil surface pressure coefficient distribution in the leading edge region for transitional flow using the Praisner and Clark transition onset model

To test the effects of transition onset location two fixed transition onset locations were picked at 3% and 3.5% of the chord, which is deeper in the separation bubble as shown in Figure 5.40, Figure 5.41, Figure 5.42, and Figure 5.43. This resulted in a reduction in the suction peak and the formation of a pressure plateau, which can be seen more clearly in Figure 5.44. The same trend of transition onset point starting earlier resulting in a shorter transition length was also found in fixed transition onset model predictions. Oscillatory solutions were obtained when the transition onset point was too deep inside the separation bubble ($x_{t,ss} > 0.035C$).
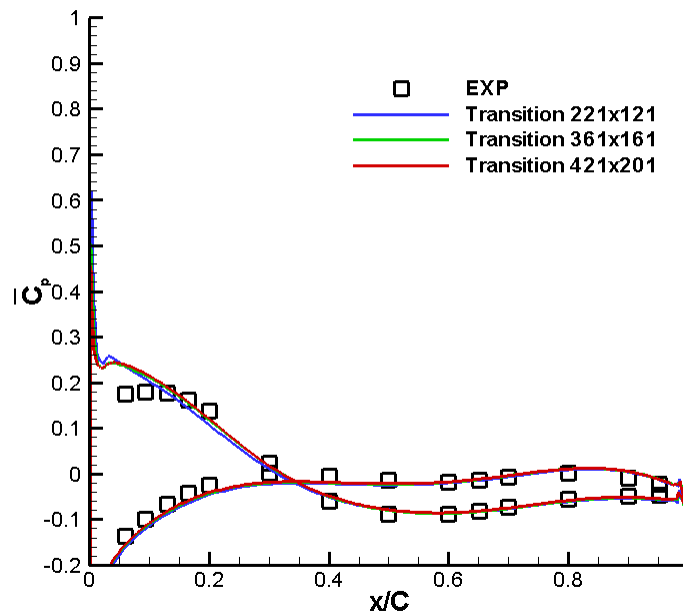
Figure 5.40 High incidence angle airfoil surface pressure coefficient distribution for transitional flow using the fixed transition onset model with $x_{t,ss} = 0.03C$
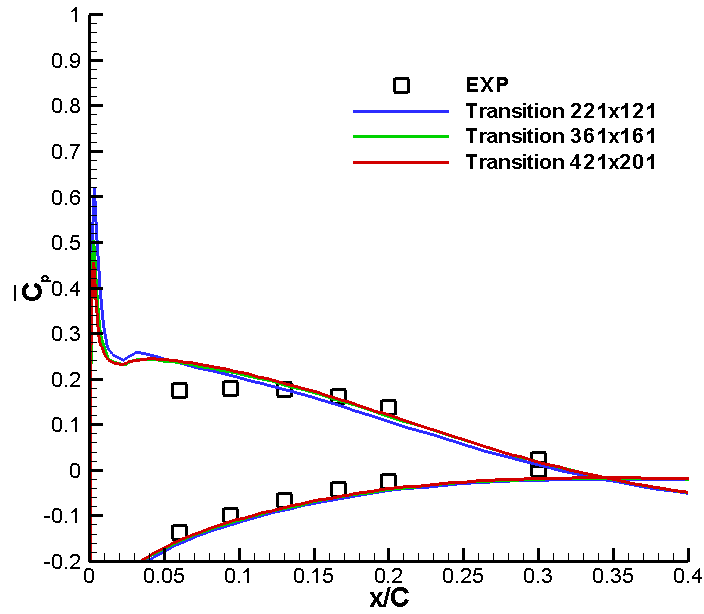
Figure 5.41 High incidence angle airfoil surface pressure coefficient distribution in the leading edge region for transitional flow using the fixed transition onset model with $x_{t,ss} = 0.03C$
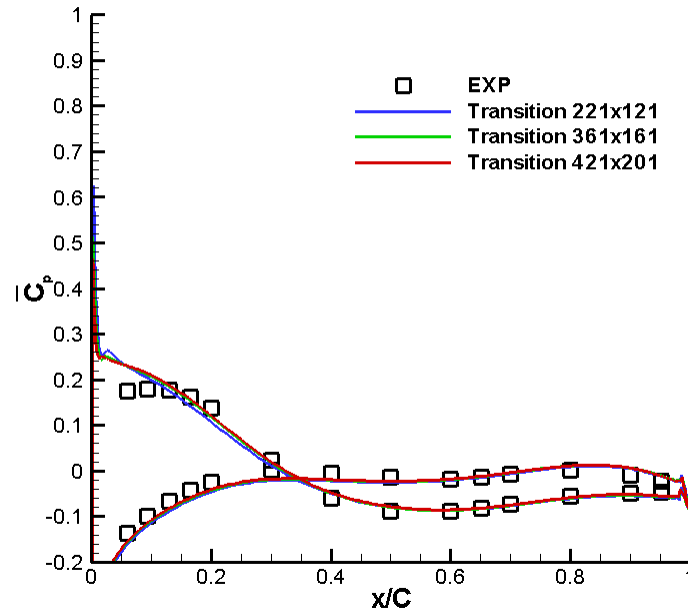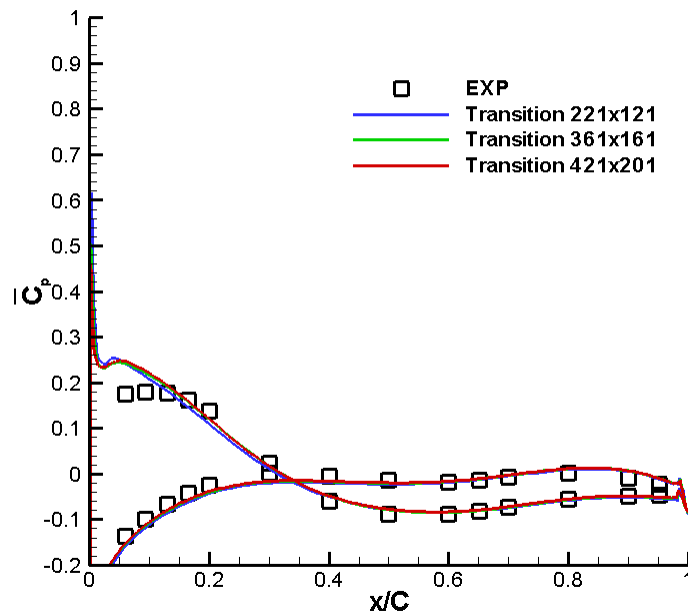

Figure 5.42 High incidence angle airfoil surface pressure coefficient distribution for transitional flow using the fixed transition onset model with $x_{t,ss} = 0.035C$
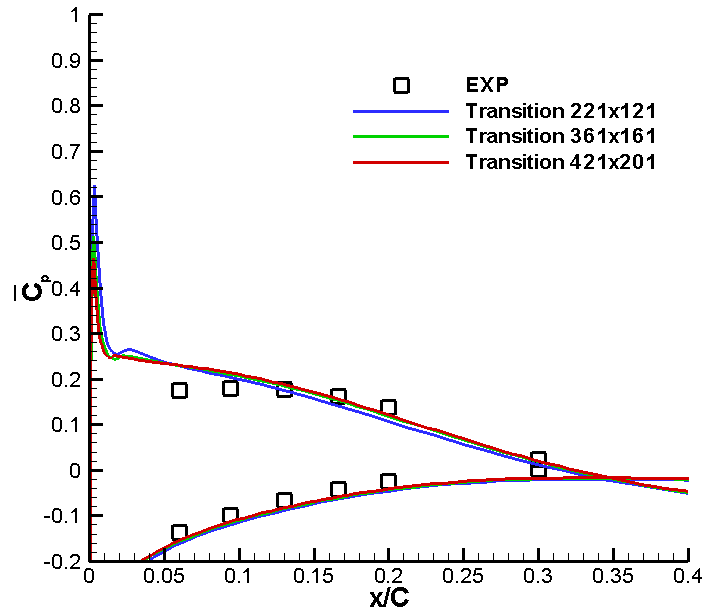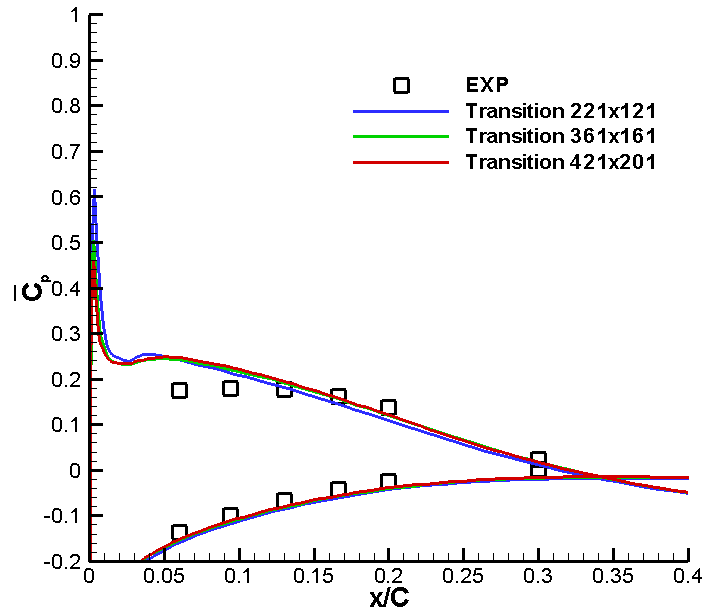
Figure 5.43 High incidence angle airfoil surface pressure coefficient distribution in the leading edge region for transitional flow using the fixed transition onset model with $x_{t,ss}$ = 0.035C

Figure 5.44 shows the fully turbulent pressure distribution compared with the transition model results for different transition onset models. Fix transition case 1 represents the transitional flow using the fixed transition onset model with $x_{t,ss}$ = 0.03C, and fix transition case 2 represents the transitional flow using the fixed transition onset model with $x_{t,ss}$ = 0.035C. The suction peak in the transitional predictions are lower than the fully turbulent results and there is a formation of a pressure plateau, which can also clearly be seen in Figure 5.45.
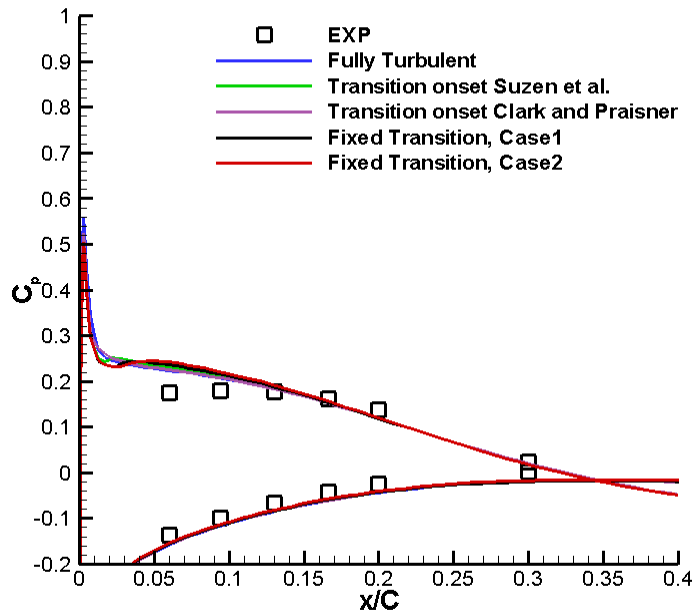
Figure 5.44 High incidence angle airfoil surface pressure coefficient distribution leading edge region for transitional flow on the 361x161 grid
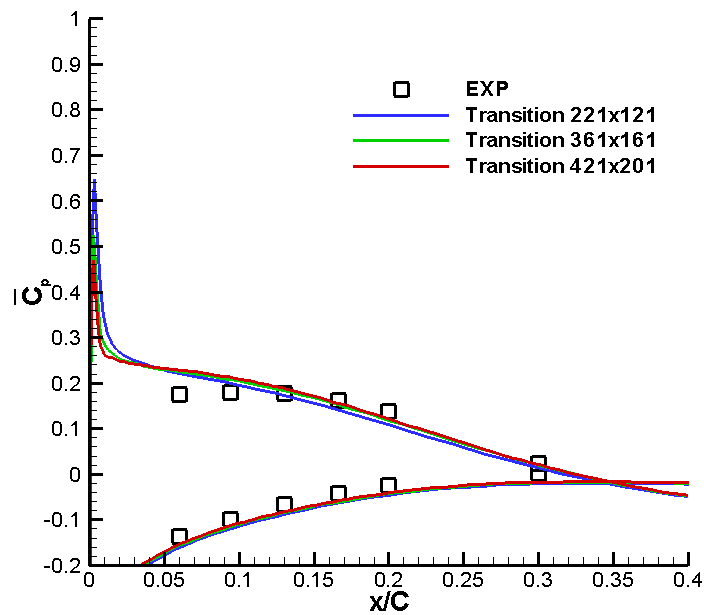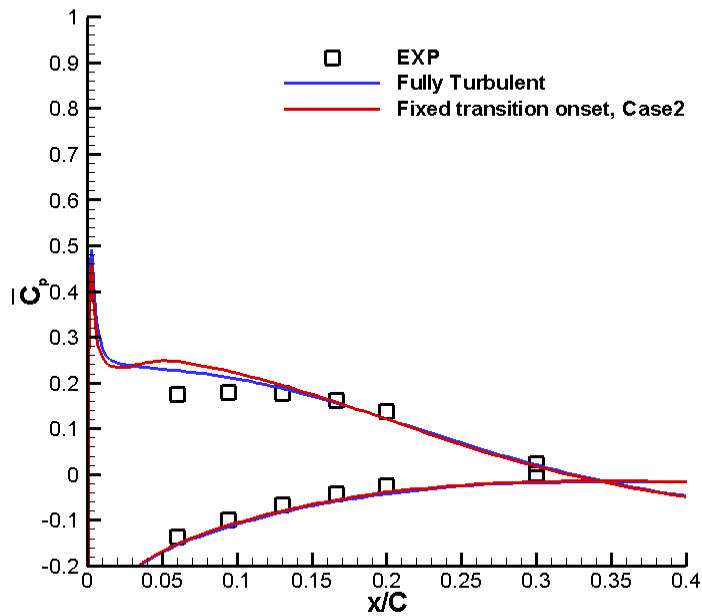

Figure 5.45 High incidence angle airfoil surface pressure coefficient distribution leading edge region for transitional flow on the 421x201 grid

The high incidence angle case has a much larger separation bubble than the low incidence angle case on the suction surface. For almost all transition onset models (Suzen et al., Praisner and Clark, and Fixed transition case1), the predicted reattachment point for the 221x121, 361x161 and 421x201 grids is at 41.6%, 43.2% and 44% of chord, respectively. The separation bubble can also be seen in ρu contours plot of Figure 5.46 and Figure 5.47. As a comparison of fully turbulent and transitional flow, the leading edge ρu contour plots are presented in Figure 5.47. The fully turbulent and transitional flows have almost the same bubble length and height, the bubble height in transitional flow is 1.5% of chord and is 1.4% of chord for fully turbulent flow.
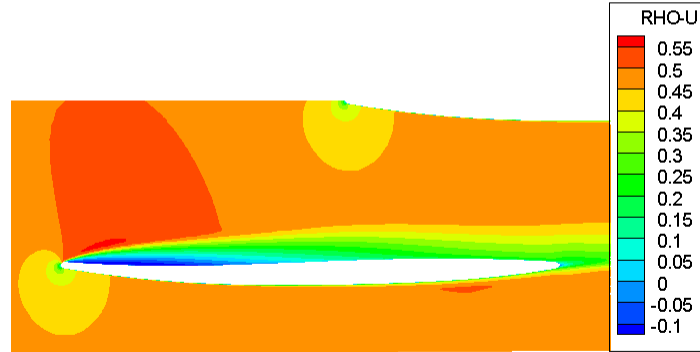
Figure 5.46 Contours of ρu at 10º chordal incidence showing the separation bubble for transitional flow on the 361x161 grid using the Suzen et al. transition onset model
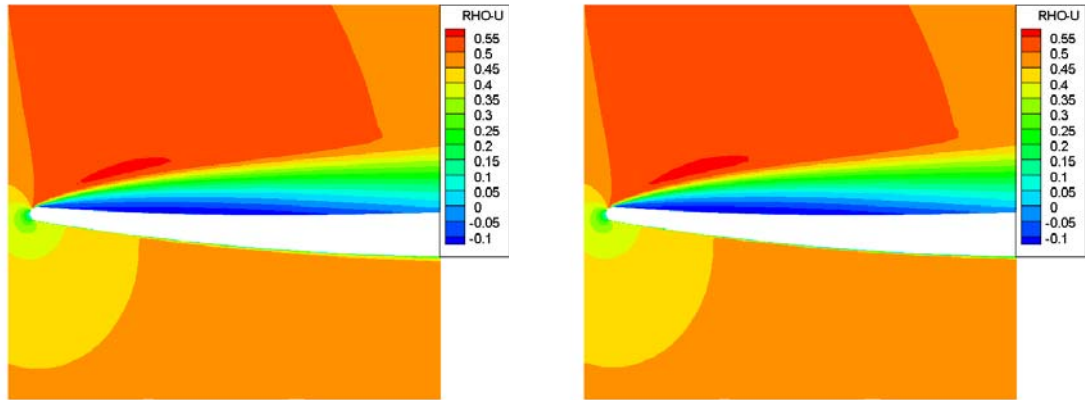
(a) fully turbulent flow   (b) transitional flow

Figure 5.47 Leading edge contours of ρu at 10° chordal incidence showing the separation bubble on the 361x161 grid using the Suzen et al. transition onset model

From all the transition result, it is seen that the transition zone starts and ends within the separation bubble. The SWG calculations are not much different than the fully turbulent results.   The calculations do show a trend close to the leading edge which is promising.   SWG transition model combined with the fixed transition onset model with $x_{t,ss} = 0.035C$ has the best correlation with the experimental data. The suction peak for the fully turbulent solution is the highest. The lowest suction peak occurs for the largest transition length.   The NASA/P&W at high incidence angle condition has a much larger separation bubble than the low incidence angle condition.   The SWG model show promising results in that a pressure plateau is forming but it is smaller than exhibited by the experimental data.   No effort was made to change any of the modeling coefficients within the SWG model.   The SWG transition model does not perform better because it not suitable for highly separated flows which exceed its data base.

The predicted transition onset point, transition length, separation point, and reattachment point for the three grids are given in Table 5.3 for the transition solution.

Table 5.3 Fully turbulent and SWG transition parameters for the high incidence angle condition

Transition Onset Model	$x_{ss,t}$	Transition Length	Separation Point	Reattachment Point
None, Fully Turbulent				
221x121	NA	NA	0.011C	0.422C
361x161	NA	NA	0.011C	0.439C
421x201	NA	NA	0.010C	0.447C
Suzen et al.				
221x121	0.022C	0.019C	0.011C	0.422C
361x161	0.020C	0.013C	0.011C	0.439C
421x201	0.016C	0.007C	0.010C	0.447C
Praisner and Clark				
221x121	0.010C	0.017C	0.011C	0.433C
361x161	0.010C	0.012C	0.011C	0.439C
421x201	0.013C	0.007C	0.010C	0.447C
Fixed Transition, Case 1				
221x121	0.030C	0.017C	0.011C	0.422C
361x161	0.030C	0.013C	0.011C	0.439C
421x201	0.030C	0.008C	0.010C	0.447C
Fixed Transition, Case 2				
221x121	0.035C	0.018C	0.011C	0.422C
361x161	0.035C	0.012C	0.011C	0.0439C
421x201	0.035C	0.008C	0.010C	0.441C

5.2.5   Unsteady Turbulent flow ($\bar{\alpha} = 0^\circ$)

The unsteady simulation was performed with a reduced frequency of 0.4, Reynolds number of 0.9 Million, and an inlet Mach number of 0.5. The oscillation amplitude is 0.3°. The oscillation amplitude in the experimental data is 1.2°. Higher oscillation amplitude in the calculation resulted in an unstable solution. There was grid overlap causing negative volumes in the computation. This was related to the high grid quality required to resolve the flow field in the leading edge region and the grid distortion method used by the flow solver. The unsteady fully turbulent flow computation was performed on the same three grids used for the steady flow calculations. Figure 5.48 presents the NPHASE predicted work-per-cycle. The results indicate that the work-per-cycle is constant after the second oscillation cycle and there are small differences in the work-per-cycle with the selected grid size.
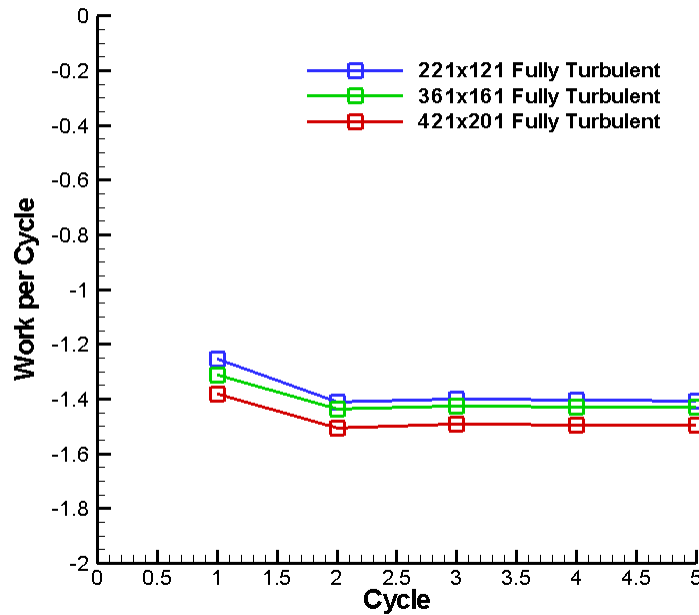
Figure 5.48 Low incidence angle work per cycle for fully turbulent flow (M = 0.5, k = 0.4, $\bar{\alpha} = 0^\circ$, σ = 180°)

For the unsteady flow computation, C_m converges to a sinusoidal type wave shape as shown in Figure 5.49, which is typical of the behavior exhibited by each grid used in the unsteady turbulent flow study. This indicates the solution was stabilized.
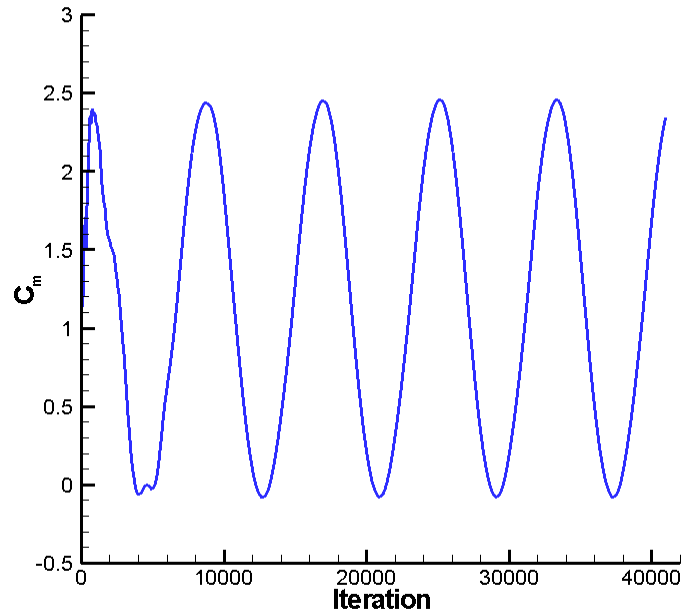
Figure 5.49 Low incidence angle time dependent moment coefficient for fully turbulent flow (361x161 Grid, M = 0.5, k = 0.4, $\bar{\alpha}$ = 0º, σ = 180º)

The first harmonic pressure coefficients are shown in Figure 5.50. The pressure surface response is dominated by $Re(C_p)$ forward of midchord. All solutions appear to overlap for the different grids. The suction surface pressure coefficients are affected by the separation with slightly larger pressure fluctuations over the first quarter of the airfoil. The predictions show excellent trendwise agreement with the experimental data. However, the imaginary part of the pressure surface is a bit underpredicted. On the suction surface, there are small differences between the different grids. The real part of the pressure distribution has a lower value with the denser grid. This is the reason for the slight differences in work-per-cycle. Also, solutions indicate a small grid dependency where separation bubble is located.

91
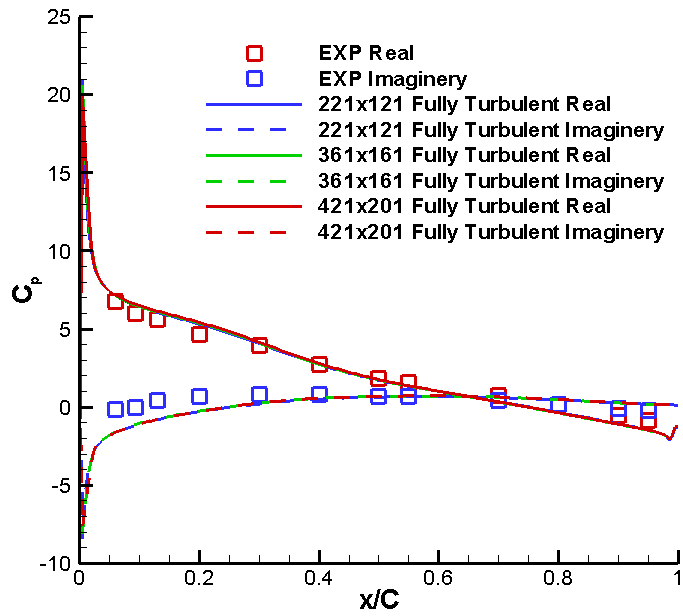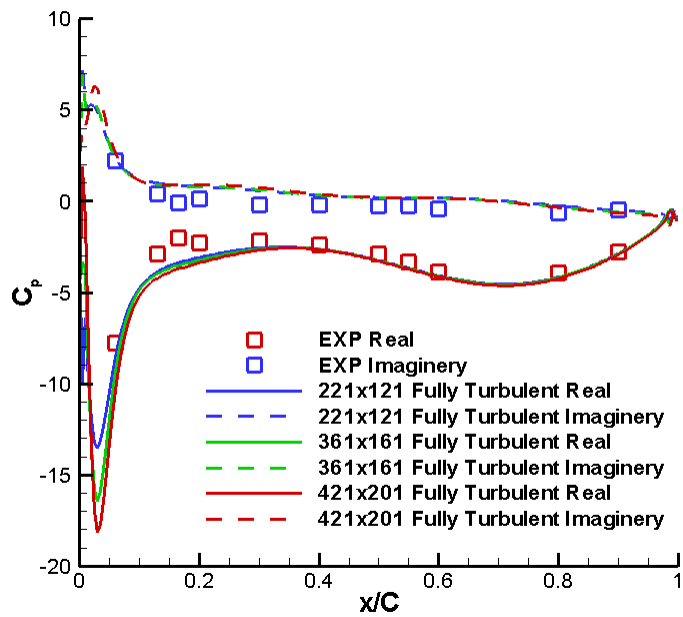
(a) Pressure Surface

(b) Suction Surface

Figure 5.50 Low incidence angle airfoil surface unsteady pressure coefficient

distribution for fully turbulent flow (M = 0.5, k = 0.4, $\bar{\alpha}$ = 0º, σ = 180º)

The Work Impulse parameter shown in Figure 5.51, can be used to indicate areas of airfoil instability. Also, it can be used to identify local flow physics with airfoil instability. Furthermore, designers can use this type of information to redesign unstable blades. In the vicinity of the leading edge, the attached flow contributes to stability. However, in the region varying from 10 to 40% chord, the attached flow is destabilizing. The predictions are seen to have good trendwise agreement with the experimental data. However, the calculations do underpredict the chordwise work function in the leading edge region.
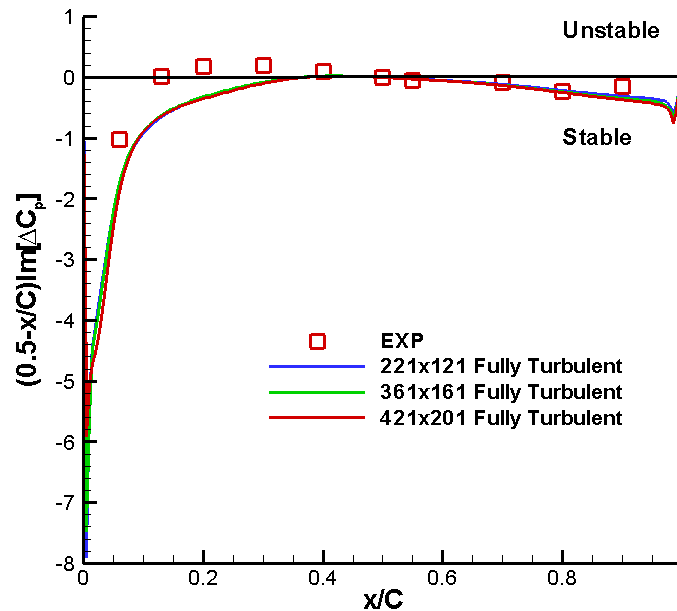
Figure 5.51 Low incidence angle work impulse for fully turbulent flow (M = 0.5, k = 0.4, $\bar{\alpha} = 0º$, σ = 180º)

5.2.5.1 Cycle study

The effect of different oscillation cycles is investigated for the low incidence angle case. The grid size of 361x161 was used for this study. Figure 5.52 and Figure 5.53 present the NPHASE predicted unsteady pressure coefficient distribution and Work

Impulse for five cycles and ten cycles. The oscillation amplitude is 0.3º. These results indicate that the differences between five cycles and ten cycles negligible. Furthermore, for this flow condition five oscillation cycles is sufficient for the unsteady simulations.
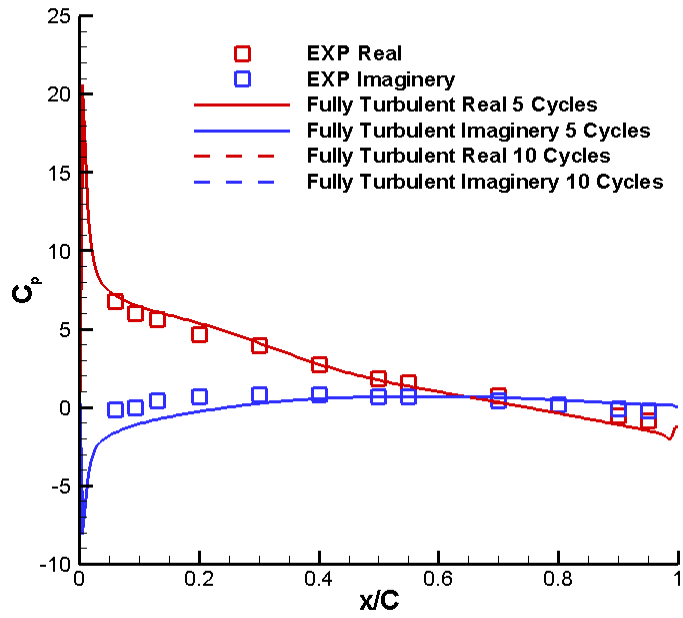
(a) Pressure Surface
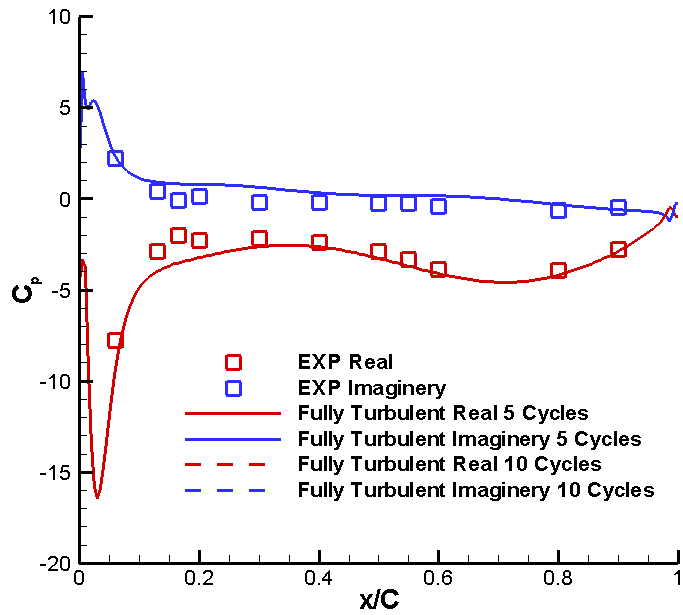
(b) Suction Surface

Figure 5.52 Effect of oscillation cycles on low incidence angle airfoil surface unsteady pressure coefficient distribution for fully turbulent flow (M = 0.5, k = 0.4, $\bar{\alpha}$ = 0º, σ = 180º)

95

For the work impulse, although both computational predictions are slightly below the experimental data, they all exhibit good trendwise agreement as displayed in Figure 5.53. The work impulse for five cycles and ten cycles is the same.

Figure 5.53 Effect of oscillation cycles on low incidence angle work impulse for fully turbulent flow (M = 0.5, k = 0.4, $\bar{\alpha}$ = 0º, σ = 180º)

5.2.5.2 Time step study

The effect of time step was investigated for the low incidence angle case. The grid size of 361x161 was used for this study. The oscillation amplitude was 0.3º. Figure 5.54 presents the NPHASE predicted work-per-cycle for 8192 points-per-cycle and 16384 points-per-cycle. These results indicate that the work-per-cycle is constant after the second oscillation cycle and there are negligible differences in the work-per-cycle with time-step for the values selected. Furthermore, for this flow condition 8192 points-per-cycle is sufficient for the unsteady simulations.
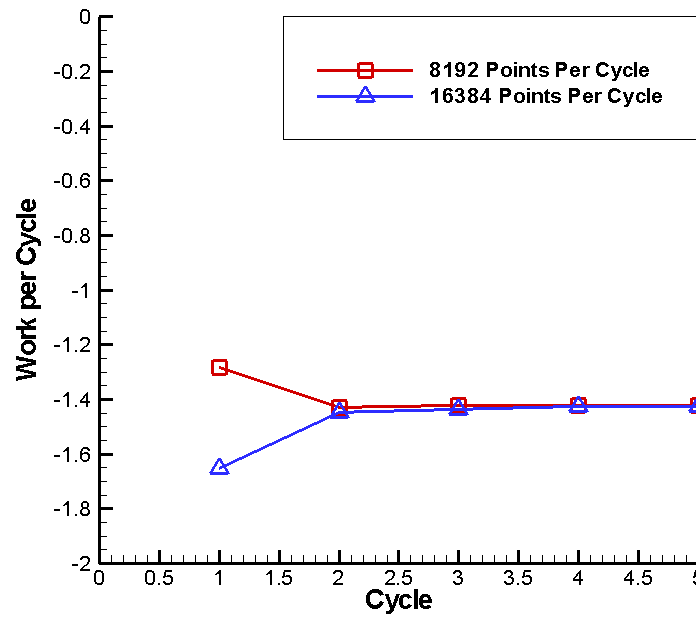
Figure 5.54 Effect of time step on the low incidence angle work-per-cycle for fully

turbulent flow (M = 0.5, k = 0.4, $\bar{\alpha}$ = 0º, σ = 180º)

Figure 5.55 presents the NPHASE predicted unsteady pressure coefficient distribution for 8192 points-per-cycle and 16384 points-per-cycle. Both results are the same.
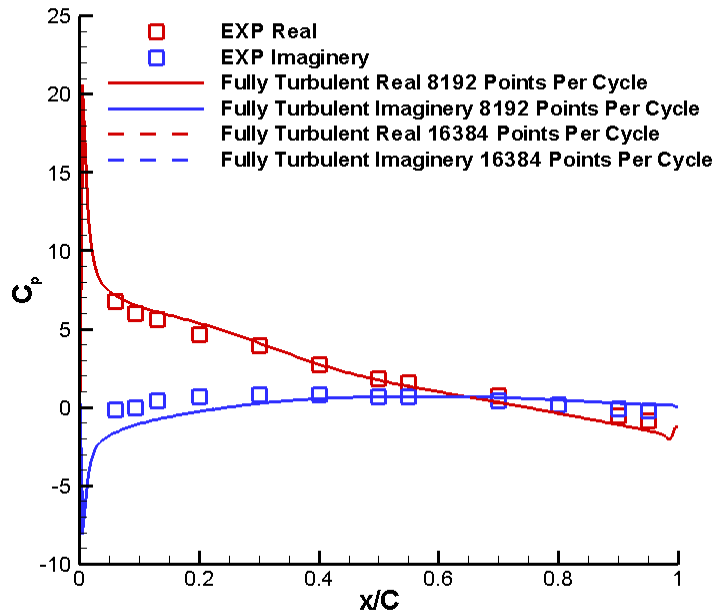
(a) Pressure Surface
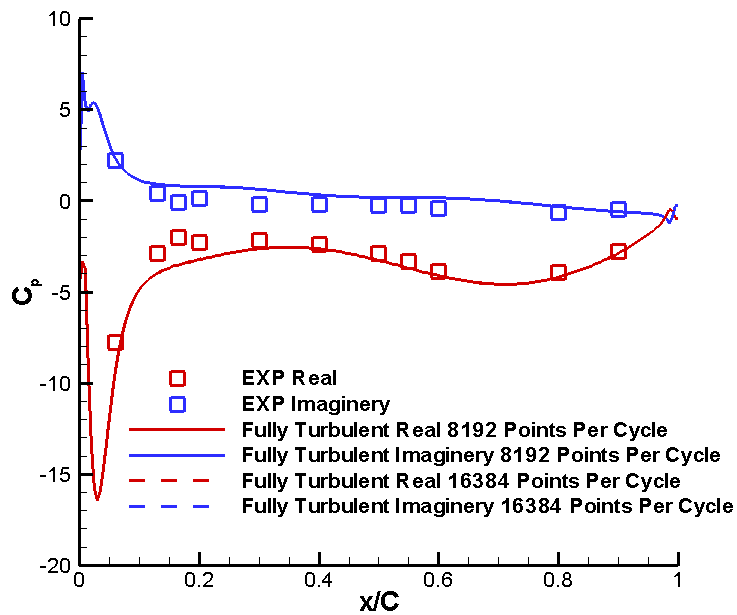
(b) Suction Surface

Figure 5.55 Effect of time step on the low incidence angle airfoil surface unsteady pressure coefficient distribution for fully turbulent flow (M = 0.5, k = 0.4, $\bar{\alpha}$ = 0º, σ = 180º)

Although both computational predictions are slightly below the experimental data, the two different points per cycle exhibit good trendwise agreement as shown in Figure 5.56. The work impulse for 8192 points-per-cycle and 16384 points-per-cycle are the same.
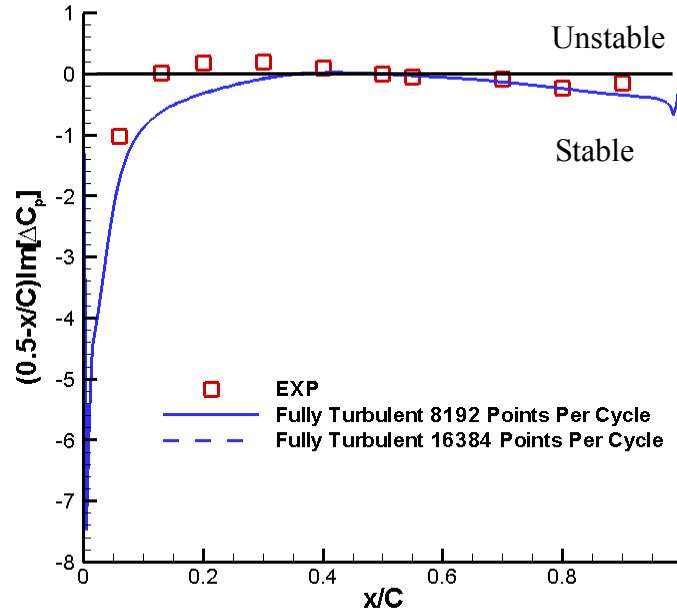
Figure 5.56 Effect of time step on low incidence angle work impulse for fully turbulent flow (M = 0.5, k = 0.4, $\bar{\alpha} = 0°$, σ = 180°)

5.2.5.3 Oscillation amplitude study

The effect of oscillation amplitude was also investigated for the low incidence angle case. The grid size of 361x161 was used for this study. Figure 5.57 and Figure 5.58 present the NPHASE predicted unsteady pressure coefficient distribution and work impulse for oscillation amplitudes of 0.3º, 0.15º and 0.075º. There is no difference among the three oscillation amplitude on pressure surface. On the suction surface, only small differences among the three oscillation amplitude was found in the leading edge region. The oscillation amplitude at 0.3º was used for all other calculations for the low incidence angle unsteady turbulent flow and transitional flow study.
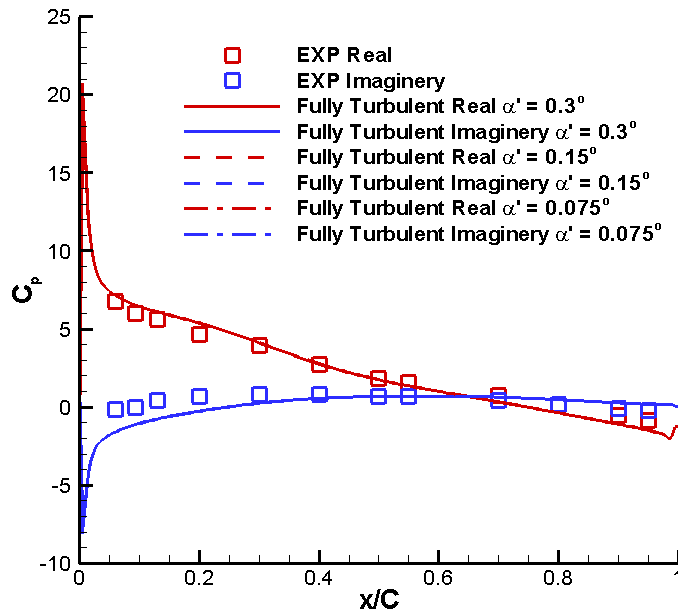
(a) Pressure Surface
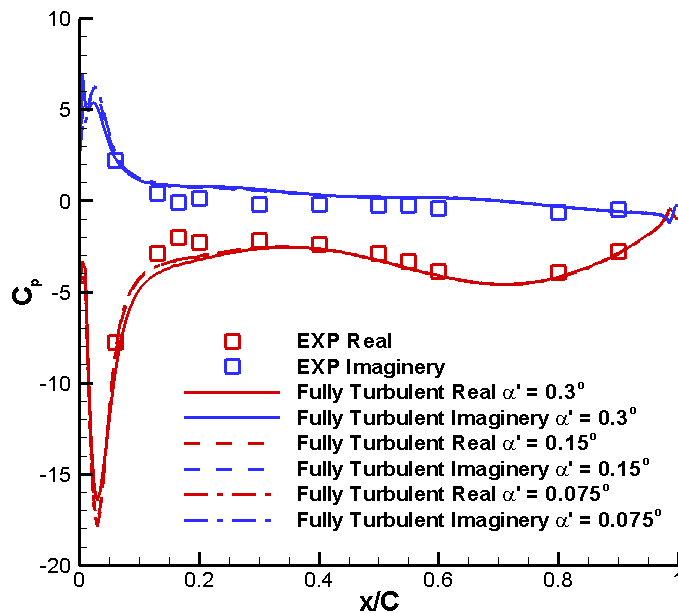
(b) Suction Surface

Figure 5.57 Effect of oscillation amplitude on the low incidence angle airfoil surface unsteady pressure coefficient distribution for fully turbulent flow (M = 0.5, k = 0.4, $\bar{\alpha}$ = 0°, σ = 180°)

The difference between the oscillation amplitude 0.3º and 0.15º are negligible. There is only small deviation for the oscillation amplitude 0.075º with other two oscillation amplitudes.
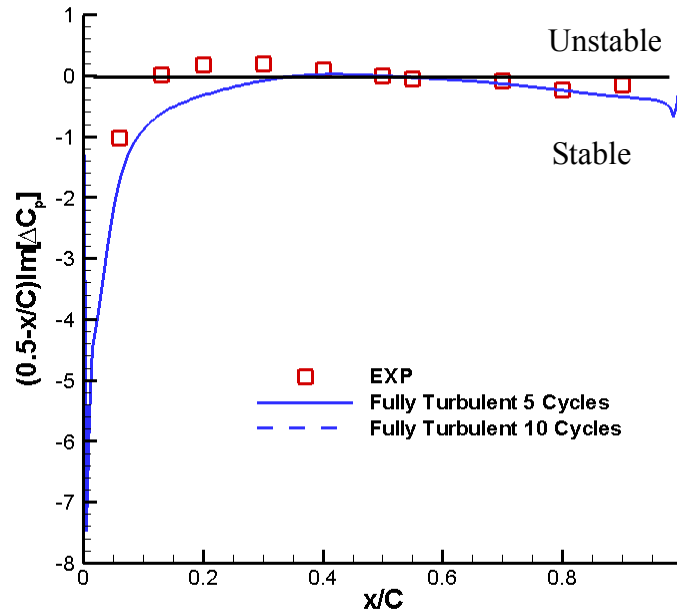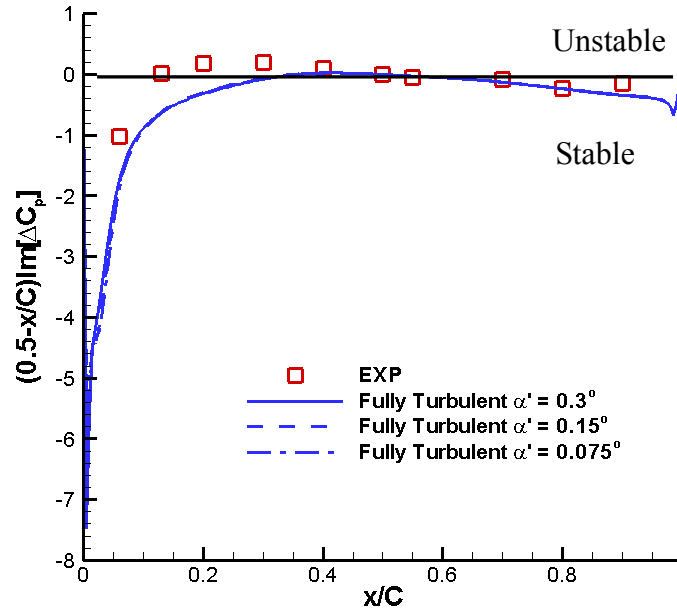

Figure 5.58 Effect of oscillation amplitude on low incidence angle work impulse for fully turbulent flow (M = 0.5, k = 0.4, $\bar{\alpha}$ = 0º, σ = 180º)

5.2.6 Unsteady Transitional flow ($\bar{\alpha}$ = 0º)

The transition predictions are performed based on the fully turbulent solution with the same chordal incidence angle, pressure ratio, and freestream Mach number. Computations are conducted on the same three grids as was used for turbulent flow. Three transition onset models along with SWG transition model are used in the transitional computations. The transition onset models are Suzen et al., Praisner and Clark, and fixed transition onset. The unsteady transitional simulation was performed with a reduced frequency of 0.4, Reynolds number of 0.9 Million, and an inlet Mach number of 0.5. The oscillation amplitude was 0.3º.

5.2.6.1 Suzen et al. transition onset model

The results from unsteady transitional flow computation using the Suzen et al. transition onset model are given this section. Figure 5.59 presents the NPHASE predicted work-per-cycle. The results indicate that the work-per-cycle is constant after the second oscillation cycle and there are small differences in the work-per-cycle with the selected grid size.

Figure 5.59 Low incidence angle work per cycle for transitional flow using the Suzen et al. transition onset model (M = 0.5, k = 0.4, $\bar{\alpha} = 0°$, σ = 180°)

Figure 5.60 shows the first harmonic pressure coefficients.   The pressure surface response is dominated by the real part of the pressure coefficient ($Re(C_p)$) forward of midchord. The suction surface pressure coefficients are influenced by the separation with a larger pressure fluctuations over the first quarter of the airfoil. The predictions are in good trendwise agreement with the experimental. The imaginary part of the pressure surface is slightly underpredicted. On the suction surface, the denser grid has lower value on the real part of the pressure distribution and higher value on the imaginary part than other two grids. This leads to the sight difference in work-per-cycle. Also, the imaginary part of the pressure distribution is higher than it is in fully turbulent solution.
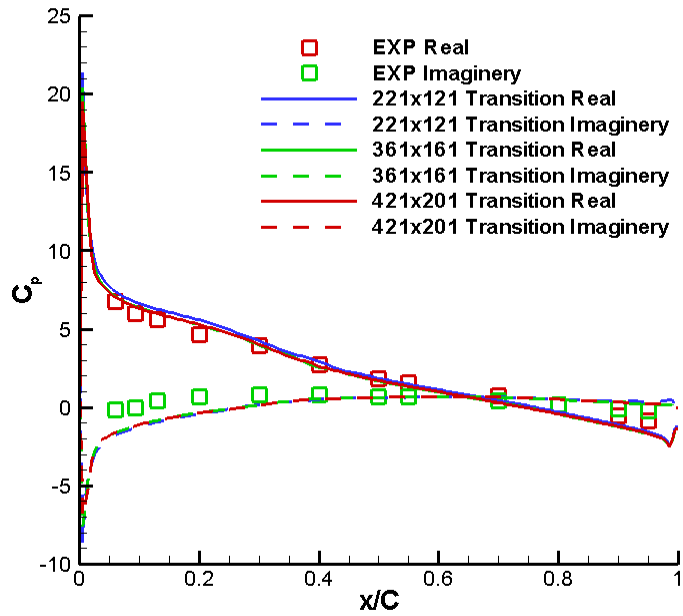
(a) Pressure Surface
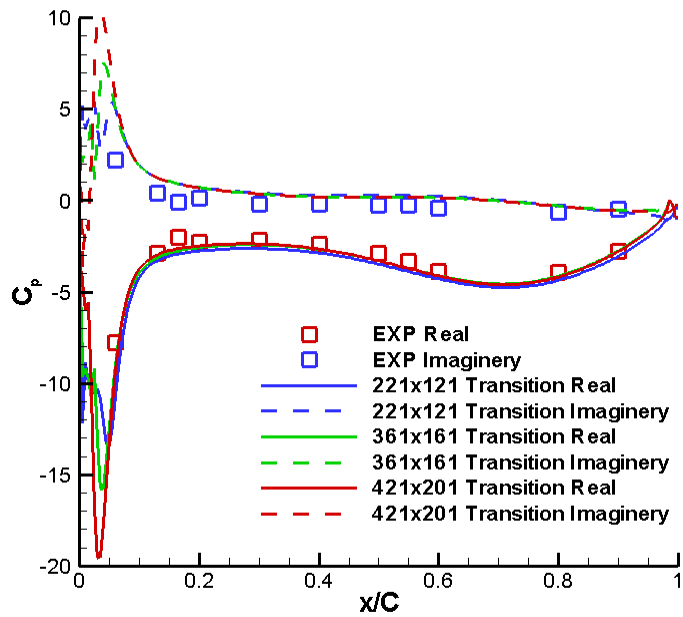
(b) Suction Surface

Figure 5.60 Low incidence angle airfoil surface unsteady pressure coefficient distribution for transitional flows using the Suzen et al. transition onset model (M = 0.5, k = 0.4, $\bar{\alpha}$ = 0º, σ = 180º)

For the transitional work impulse prediction a small plateau was found on the work impulse near the leading edge for all three grids. The prediction is slightly below the experimental data, but exhibit good trendwise agreement as presented in Figure 5.61. The plateaus were not shown in the fully turbulent solution in Figure 5.51.
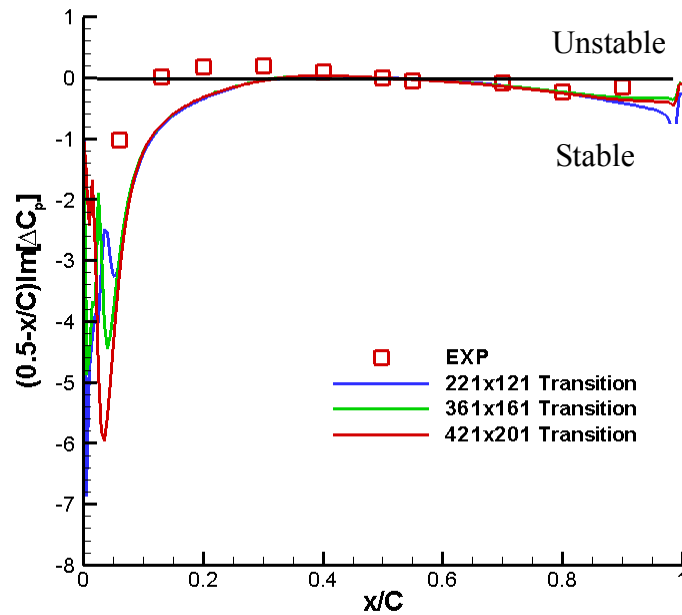
Figure 5.61 Low incidence angle work impulse for transitional flow using the Suzen et al. transition onset model (M = 0.5, k = 0.4, $\bar{\alpha}$ = 0º, σ = 180º)

5.2.6.2   Praisner and Clark transition onset model

The unsteady transitional flow computation using the Praisner and Clark transition onset model results are shown below. Figure 5.62 presents the NPHASE predicted work-per-cycle. The results indicate that the work-per-cycle is constant after the second oscillation cycle and there are small differences in the work-per-cycle with the selected grid size.
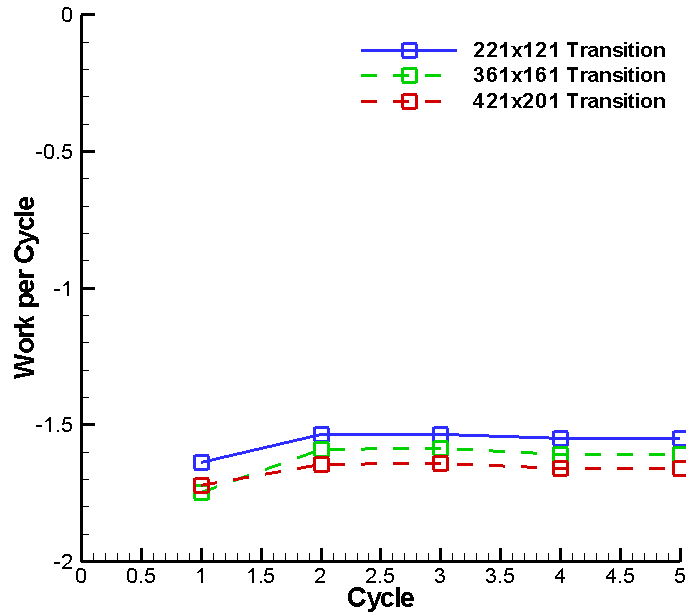
Figure 5.62 Low incidence angle work per cycle for transitional flow using the Praisner and Clark transition onset model (M = 0.5, k = 0.4, $\bar{\alpha} = 0°$, σ = 180º)

The first harmonic pressure coefficients are shown in Figure 5.63.   The pressure and suction surface pressure coefficients are similar to the Suzen et al. onset model results. The predictions show excellent trendwise agreement with the experimental data. The imaginary part of the pressure surface is a bit underpredicted. On the suction surface, the denser grid has lower value of the real part of the pressure distribution and higher value of the imaginary part than the other two grids. The suction surface peak values are closer to the leading edge than the Suzen et al. onset model due to the earlier transition onset. There are some differences in the results with grid size for the suction surface pressure coefficients in the leading edge region. Since the earlier transition onset location was predicted, the pressure distributions are close to the fully turbulent solutions.

106
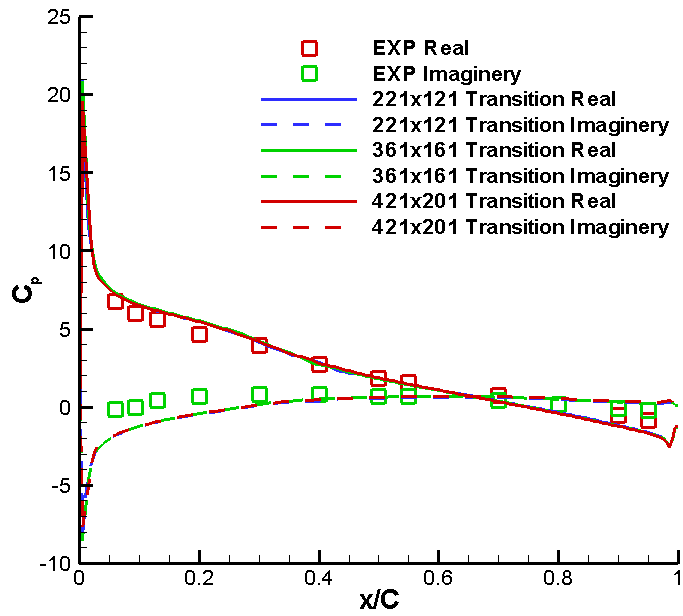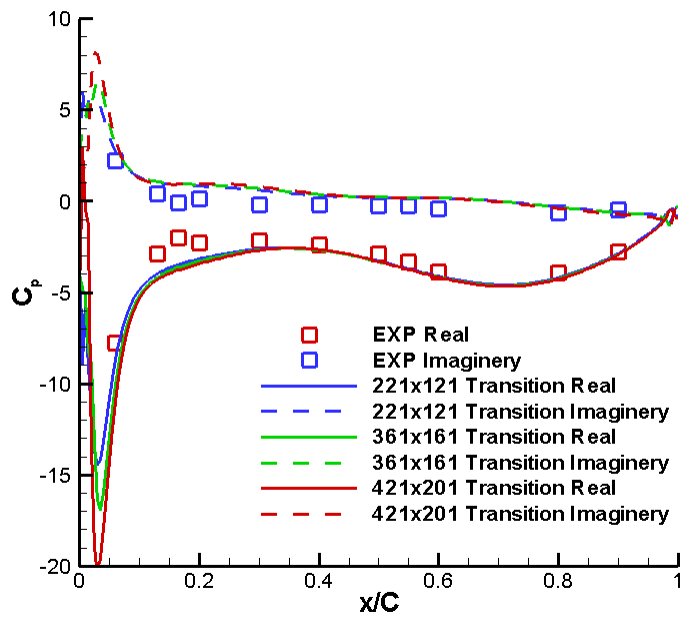
(a) Pressure Surface

(b) Suction Surface

Figure 5.63 Low incidence angle airfoil surface unsteady pressure coefficient distribution for transitional flow for the Praisner and Clark transition onset model (M = 0.5, k = 0.4, $\bar{\alpha} = 0°$, σ = 180º)

For the transitional work impulse prediction, a small plateau was found on the work impulse near the leading edge for all three grids. The prediction is slightly below the experimental data, but exhibit good trendwise agreement as shown in Figure 5.64. The plateau is smaller than it is in Suzen et al. onset model.
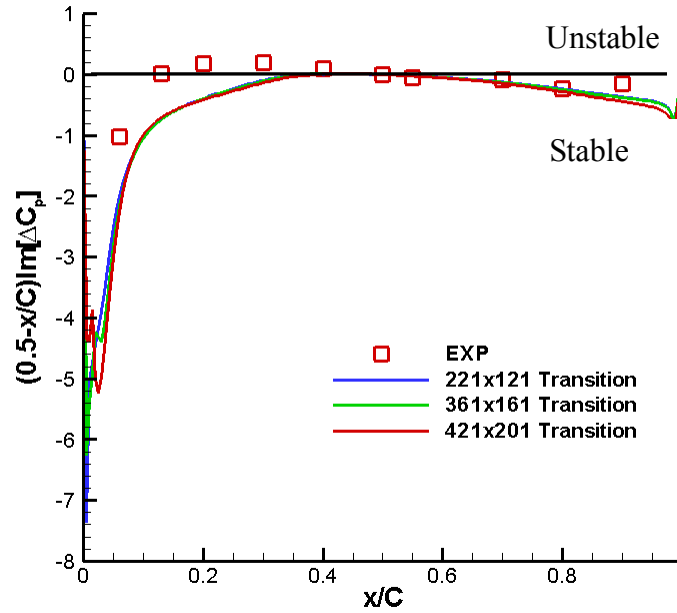
Figure 5.64 Low incidence angle work impulse for transitional flow for the Praisner and Clark transition onset model (M = 0.5, k = 0.4, $\bar{\alpha} = 0°$, σ = 180°)

5.2.6.3 Fixed transition onset

The fixed transition onset model with suction surface transition onset at 0.015C was also tested. Figure 5.65 presents the NPHASE predicted work-per-cycle. The results indicate that the work-per-cycle is constant after the second cycle and there are small differences in the work-per-cycle with the selected grid size. The changes from 221x121 grid results to 421x201 grid results are small for the fifth cycle.
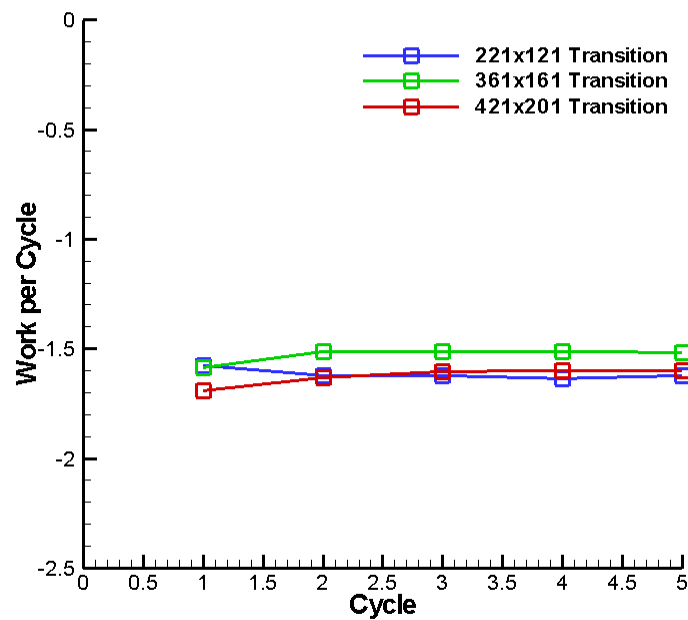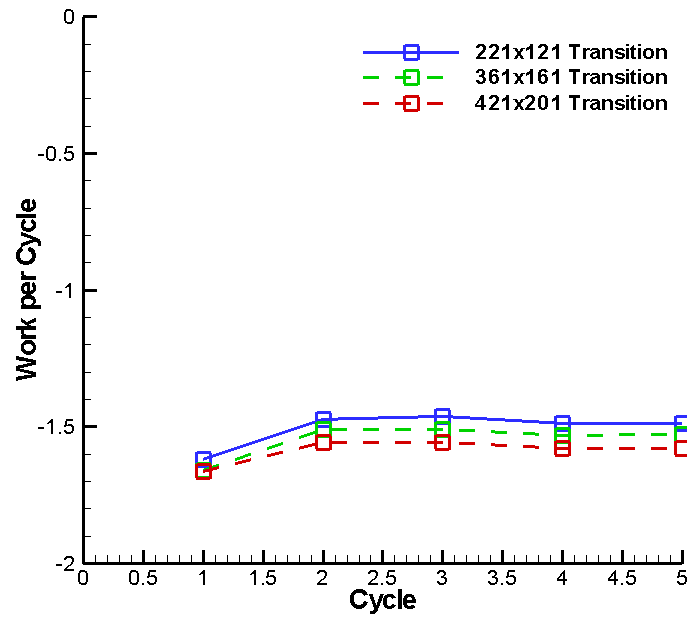
Figure 5.65 Low incidence angle work per cycle for transitional flow using the fixed transition onset model with $x_{t,ss} = 0.015C$ (M = 0.5, k = 0.4, $\bar{\alpha} = 0º$, σ = 180º)

The first harmonic pressure coefficients are shown in Figure 5.66.   The pressure coefficient distributions on the pressure surface have no difference for the three grids. The suction surface pressure coefficients have the same behavior as the other transition onset models results.
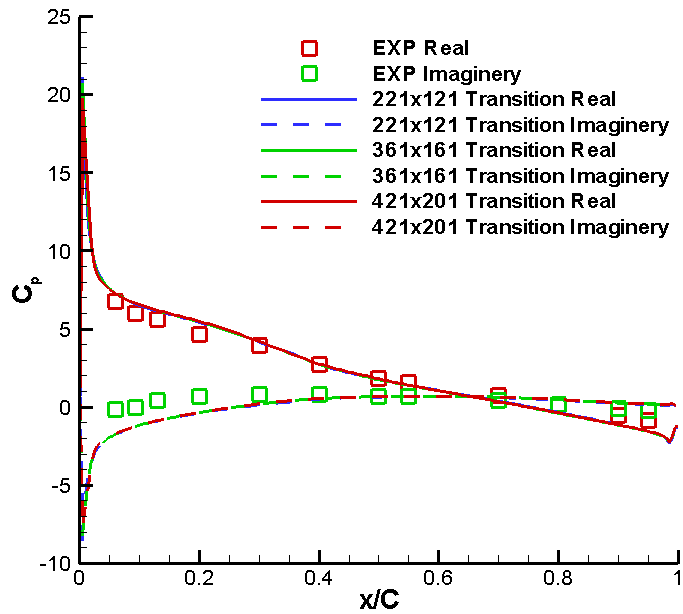
(a) Pressure Surface
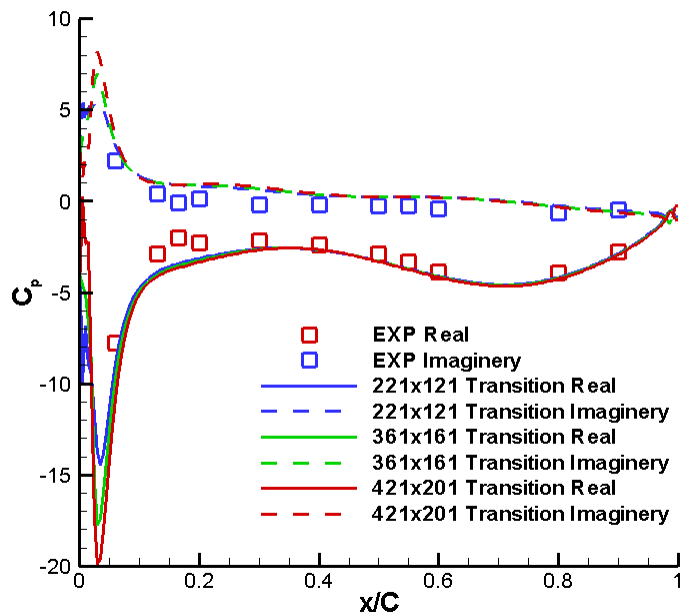
(b) Suction Surface

Figure 5.66 Low incidence angle airfoil surface unsteady pressure coefficient distribution for transitional flow using the fixed transition onset model with $x_{t,ss}$ = 0.015C (M = 0.5, k = 0.4, $\bar{\alpha}$ = 0º, σ = 180º)

110

For the transitional work impulse prediction, a small plateau was found on the work impulse near the leading edge for all three grids, as shown in Figure 5.67. The plateau is similar to the Suzen et al. onset model results due to the predicted onset location being farther downstream than the Praisner and Clark onset model and close to the Suzen et al. onset model.
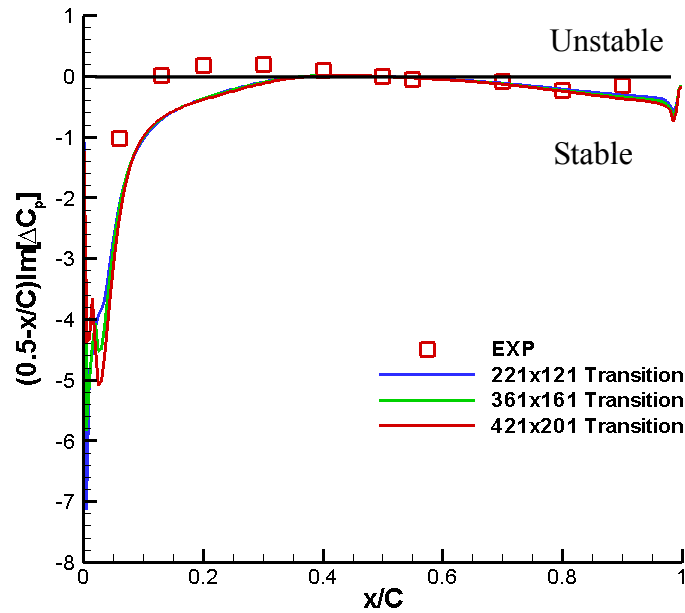
Figure 5.67 Low incidence angle work impulse for transitional flow using the fixed transition onset model with $x_{t,ss} = 0.015C$ (M = 0.5, k = 0.4, $\bar{\alpha} = 0º$, σ = 180º)

Overall, there are only small differences between the different grids for all the transition model calculations.

To illustrate the difference between fully turbulent and transition calculation, a typical onset location was selected. Fixed transition onset model with suction surface transition onset at 0.015C was compared with the fully turbulent results on 361x161 grid. Figure 5.68 presents the predicted work-per-cycle. The transitional and fully turbulent work-per-cycle are very close to each other.
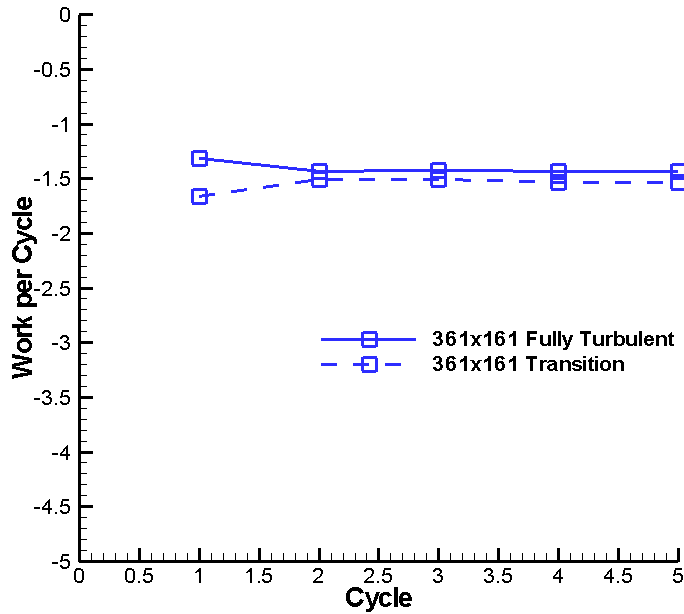
Figure 5.68 Low incidence angle work per cycle for turbulent flow and transitional flow using the fixed transition onset model with $x_{t,ss} = 0.015C$ (M = 0.5, k = 0.4, $\bar{\alpha} = 0º$, σ = 180º)

The fully turbulent and transitional first harmonic pressure coefficients are shown in Figure 5.69.   No significant change in the pressure coefficient on the pressure surface was observed for the change in the pressure surface transition onset location. The pressure distribution for transitional flow on the pressure surface is very similar to the fully turbulent solution. The suction peak on the suction surface pressure coefficients imaginary part moves more towards the downstream compared the fully turbulent. The real part of the suction surface pressure coefficients has a lower value than it was for fully turbulent flow.

112
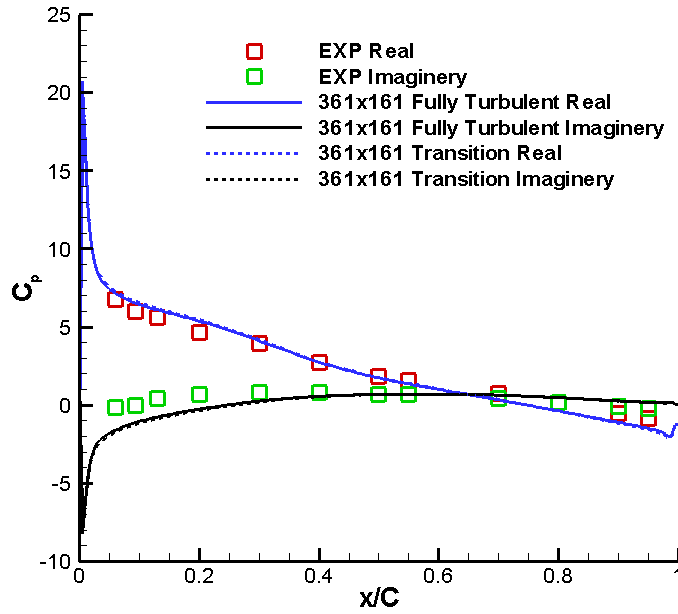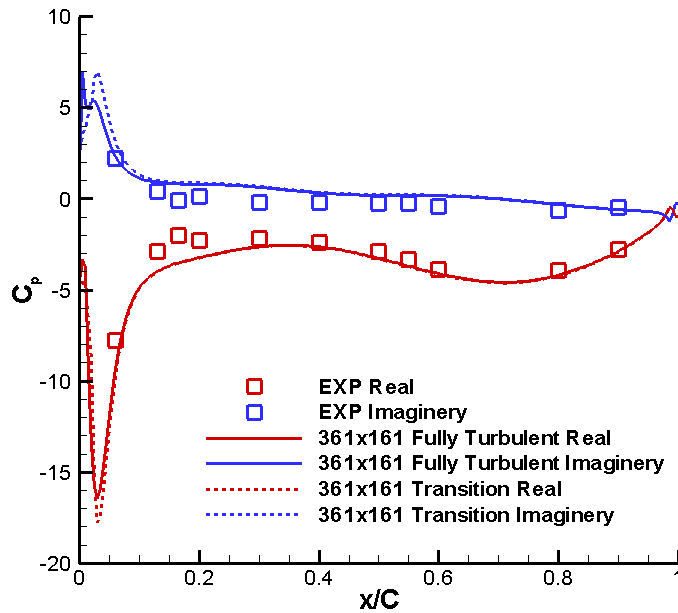
(a) Pressure Surface

(b) Suction Surface

Figure 5.69 Low incidence angle airfoil surface unsteady pressure coefficient distribution for transitional flow using the fixed transition onset model with $x_{t,ss} = 0.015C$ (M = 0.5, k = 0.4, $\bar{\alpha} = 0º$, $\sigma = 180º$)

A small plateau was found on the work impulse near the leading edge for transitional work impulse as shown in Figure 5.70, while it was not found in the fully turbulent prediction. The predictions are seen to have good trendwise agreement with the experimental data. The transition prediction is slightly more stable in the 10 to 40% chord region. Other grids also show the similar trendwise differences between fully turbulent and transitional flow.

Figure 5.70 Low incidence angle work impulse for transitional flow using the fixed transition onset model with $x_{t,ss} = 0.015C$ (M = 0.5, k = 0.4, $\bar{\alpha} = 0°$, $\sigma = 180°$)

5.2.7 Unsteady Turbulent flow ($\bar{\alpha} = 10°$)

The unsteady simulation was performed with a reduced frequency of 0.4, Reynolds number of 0.9 Million, and an inlet Mach number of 0.5. Although the time step study is important to illustrate results are time step independent. Some issues developed that appear to be generated by the highly separated flow. A grid independence study was conducted as the first attempt for the unsteady high incidence angle condition.

114

It showed promising results in that the solutions showed only a small deviation for the different grid sizes.

5.2.7.1 Grid independency study

The high incidence angle unsteady fully turbulent flow with different grid sizes was investigated. Grid sizes of 221x121 and 361x161 were used for this study. The oscillation amplitude was 0.3º with a time step of 1024 points per cycle. Figure 5.71 presents the NPHASE predicted work-per-cycle. The results indicate that the work-per-cycle is constant after the third cycle and there are small differences in the work-per-cycle with the selected grid sizes.
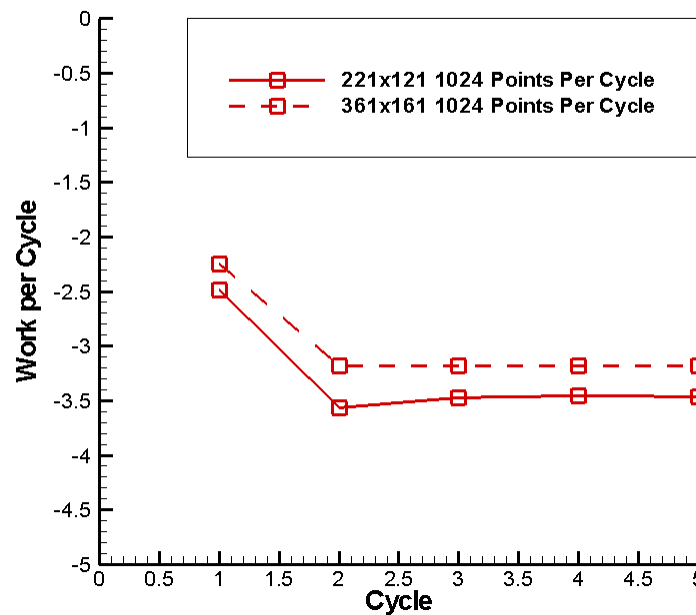
Figure 5.71 High incidence angle work per cycle for fully turbulent flow (M = 0.5, k = 0.4, $\bar{\alpha}$ = 10º, α' = 0.3º, σ = 180º)

Figure 5.72 shows the surface unsteady pressure coefficient distributions, which illustrate that changing the mean incidence angle to 10° has a dramatic effect on the suction surface unsteady pressure coefficient distributions. The pressure surface data are similar to the low incidence angle data. The calculations show trendwise agreement

with the experimental data. The suction surface imaginary part is much larger than the experimental data. The imaginary part of the pressure surface is again underpredicted relative to the experimental data. There are small differences between different grid sizes, which was reflected in the work-per-cycle calculations.
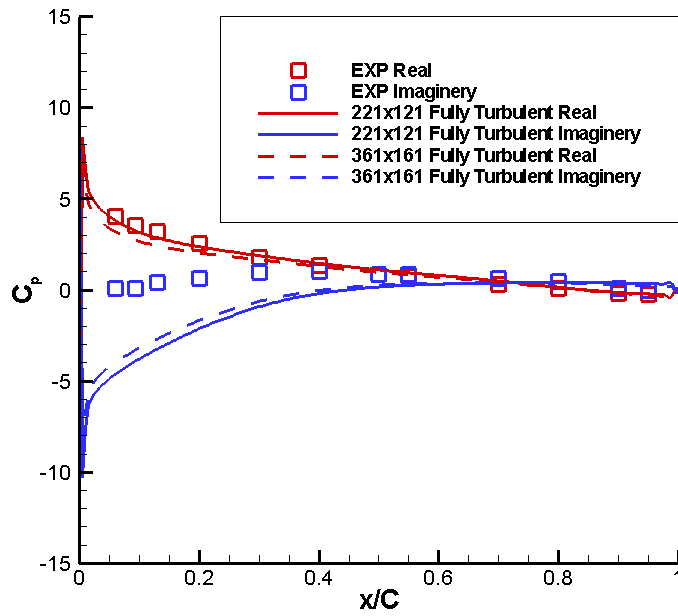
(a) Pressure Surface
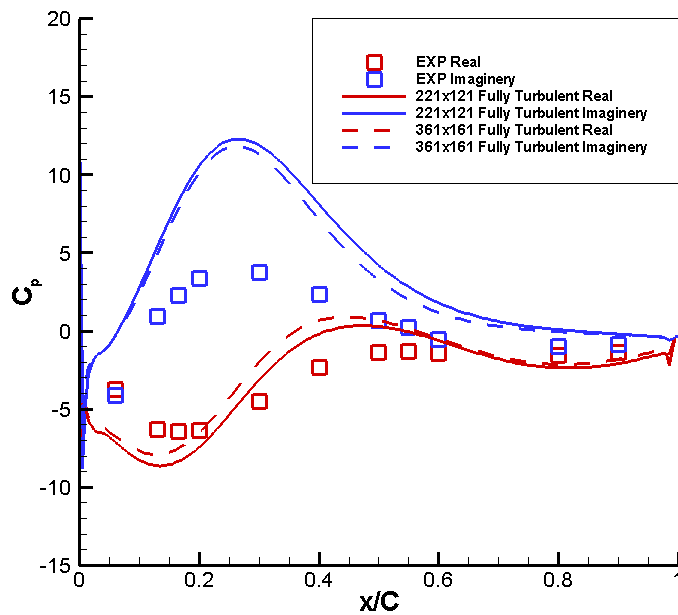
(b) Suction Surface

Figure 5.72 High incidence angle airfoil surface unsteady pressure coefficient distribution

for fully turbulent flow (M = 0.5, k = 0.4, $\bar{\alpha}$ = 10º, α' = 0.3º, σ = 180º)

117

The chordwise distribution of the work impulse is presented in Figure 5.73 for separated flow. NHASE results do not match the data very close to leading edge. The calculations show good trendwise agreements with the experimental data, but the magnitudes are larger than the experimental data in the separated flow region. This is caused by the large pressure fluctuations being predicted in the separation zone. Again, small differences noticed for the different grid sizes. This probably also tied to the poor prediction of the pressure plateau for steady flow.
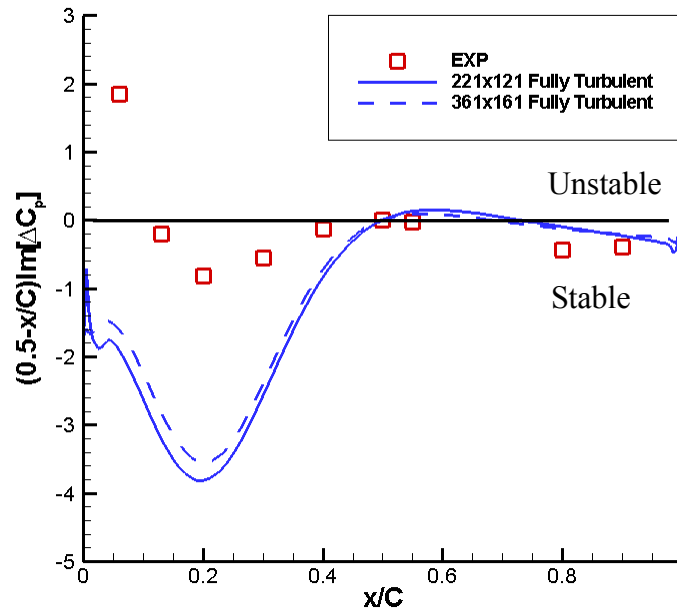
Figure 5.73 High incidence angle work impulse for fully turbulent flow (M = 0.5, k = 0.4, $\bar{\alpha}$ = 10º, α' = 0.3º, σ = 180º)

5.2.8 Unsteady Transitional flow ($\bar{\alpha}$ = 10º)

For unsteady transitional flow at the high incidence angle condition only the fixed transition onset model was considered, which will be shown in the following section.

5.2.8.1 Fixed transition onset

The steady fixed transition onset model results with suction surface transition

onset at 0.03C were shown in the previous section 5.2.4. Surface unsteady pressure coefficient distributions are shown in Figure 5.74. The pressure surface data are similar to the low incidence angle data. The suction surface pressure coefficients are affected significantly by the separation with much larger pressure fluctuations evident over the first half of the airfoil. The calculations show trendwise agreement with the experimental data. The transition results are very close to the fully turbulent solution on the pressure surface. On the suction surface imaginary part, the transition predicted a small plateau in the leading edge region which was also showed in the steady fixed transition onset results. Other than that, there are only slight differences between the transition and fully turbulent calculations. This result is consistent with the small changes found for steady flow.
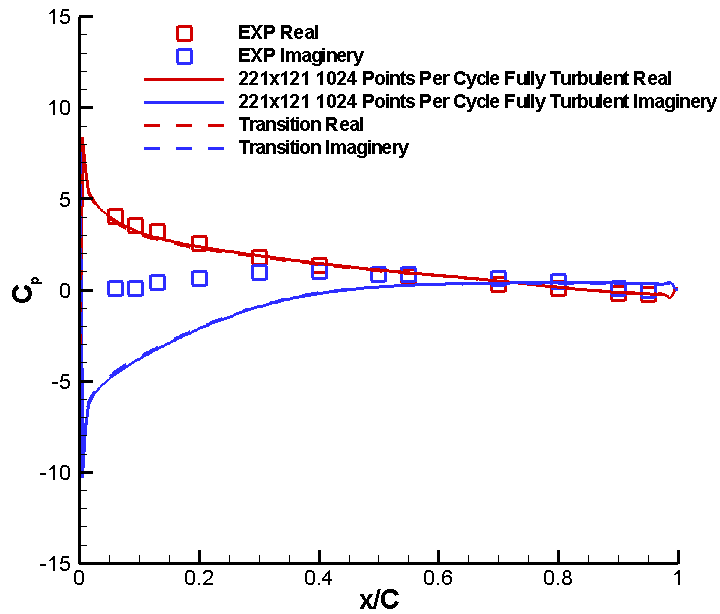
(a) Pressure Surface
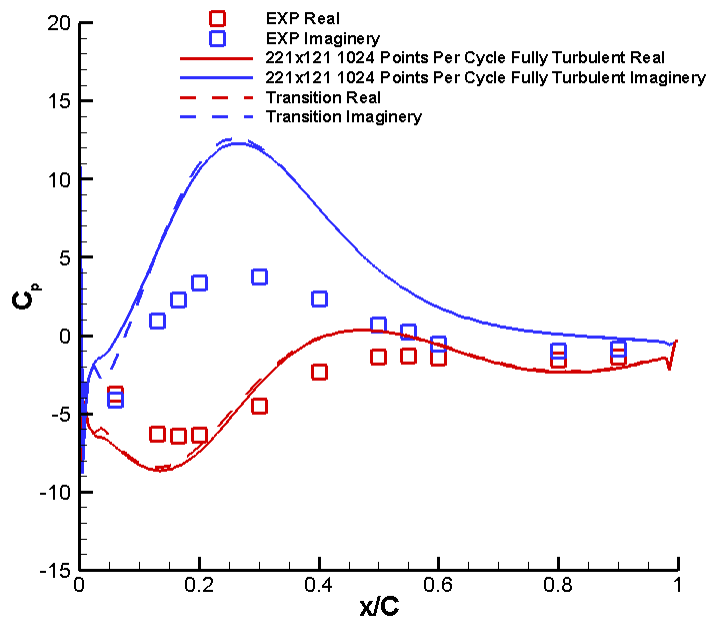
(b) Suction Surface

Figure 5.74 High incidence angle airfoil surface unsteady pressure coefficient distribution for transitional flow using the fixed transition onset model with $x_{t,ss}$ = 0.03C (M = 0.5, k = 0.4, $\bar{\alpha}$ = 10º, α' = 0.3º, σ = 180º)

The comparison of the work impulse is shown in Figure 5.75 for separated flow. The calculations show good trendwise agreement with the experimental data, but the magnitudes are more stable than the experimental data in the separated flow region. In the leading edge region, the transition result shows a slightly higher work impulse than the fully turbulent.
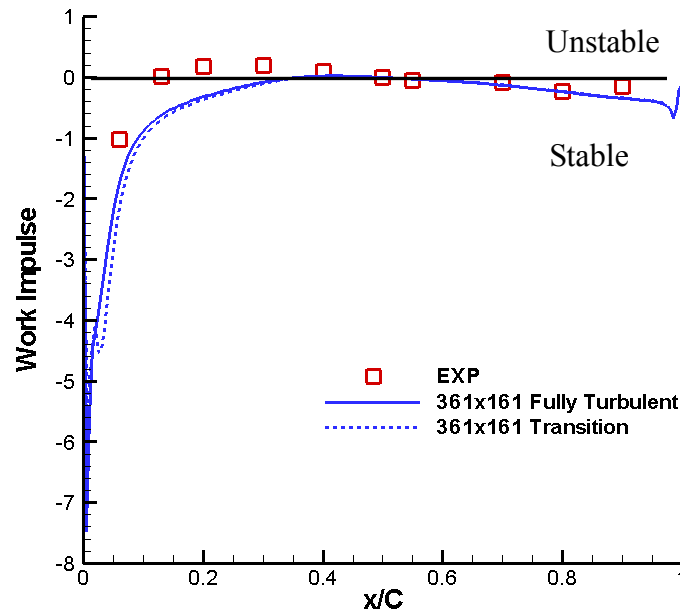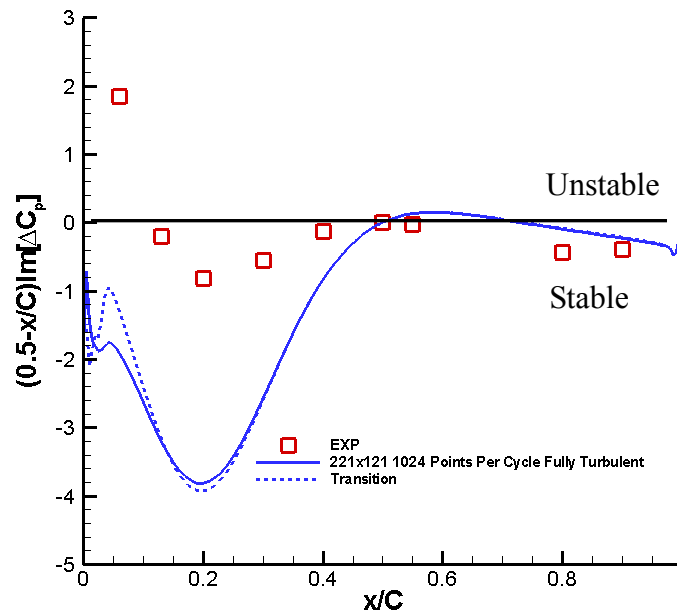

Figure 5.75 High incidence angle work impulse for transitional flow using the fixed transition onset model with $x_{t,ss} = 0.03C$ (M = 0.5, k = 0.4, $\bar{\alpha} = 10º$, α' = 0.3º, σ = 180º)

In the case of higly separated flow the correlation with the unsteady data was found to be poor in the separated flow region. This might be caused by a three-dimensional effect due to the separation bubble, or other contributing factors such as spreading half-angle, the spot propagation parameter, and spot generation rate. The predictions had large pressure fluctuations in the separation zone that did not correlate well with the experimental data. The SWG model is based on measurements in attached flows. This model is more suitable for attached flow or flow with small separation bubbles.

Chapter 6   Summary and Conclusions

6.1   Summary

In this work, the Spalart-Allmaras[39] (SA) one-equation turbulence model combined with the Solomon-Walker-Gostelow[10] (SWG) transition model were implemented into a two-dimensional Navier-Stokes solver to perform a transition study of the NASA Glenn Research Center Transonic Flutter Cascade airfoil.   The influence of transition on the NASA-GRC TFC airfoil steady pressure coefficient distribution was investigated.   Unsteady pressure distribution predictions were also performed on this airfoil to quantify the influence of transition.   Various transition onset models were incorporated with the SWG transition model to investigate the effect of the transition onset location in the transitional flow calculations.   Numerical simulation results have been correlated with measurements from the NASA-GRC TFC.

As the first step to validate the capability of the solver, classical laminar flow over a flat plate was calculated and the results were compared with the Blasius analytical solution. The results suggest that the solver is capable of resolving the laminar portion of transitional flow.

Fully turbulent flow over a flat plate was calculated using the implemented Spalart-Allmaras turbulence model. The fully turbulent boundary layer velocity profile results are compared with the experimental data correlation of Spalding.   Results show very good correlation with the experimental data within the boundary layer.   Skin friction coefficients on different grid sizes are compared with the analytical power law expression.   Simulations slightly underpredict the analytical solution due to accuracy of the turbulence model at low Reynolds numbers as well as the Mach number effect for compressible flow.

In order to conduct the transition flow calculation, the SWG transition model was implemented in the flow solver.   Transition onset models are also necessary to predict

the transition onset location. Five transition onset models were implemented into the solver: 1) Michel's criteria is used for attached flow; 2) Suzen et al.'s onset model is used for attached and separated flow; 3) Steelant and Dick's onset model is used for attached flow; 4) Praisner and Clark's onset model is used for separated flow; 5)Fixed transition onset model is used for attached and separated flow.

For flat plate transitional flow, momentum thickness Reynolds number and skin friction coefficients are compared with the experimental data by using the Spalart-Allmaras turbulence model and the SWG transition model. Different transition onset models were used to study the effect of the transition onset location. Overall the simulated flat plate prediction matched the experimental data for transitional flow. These results suggest that the flow solver with the SWG transition model can predict the transition zone and can be used to solve a more complex flow condition.

The compressor airfoil used in this investigation had a cross-section typical of modern high performance low aspect ratio fan or compressor blades in aircraft gas turbine engines. This cross-section would be found near the tip of the blade where the relative velocity is supersonic at the design point. At part speed operating conditions this portion of the blade would be subjected to high subsonic or transonic Mach numbers with large mean incidence angles. Viscous effects are of significant importance at these operating conditions due to flow separation. For these operating conditions the blade would be susceptible to subsonic/transonic stall flutter.

A previous experimental study for this particular airfoil cross-section was conducted in the NASA Transonic Flutter Cascade at the Glenn Research Center. The airfoil design originated at Pratt & Whitney and is referred to as the NASA/P&W airfoil. In the experimental investigation and also in this investigation, it was found that at high mean incidence the flow had a large separation bubble in the leading edge region, and in this region there was a contribution towards airfoil instability, i.e. flutter. In order to predict the flutter phenomena, accurate calculation of the steady and unsteady

aerodynamic loading on the turbomachinery airfoils is necessary. A transition model is also necessary. Since there are no adequate transition models for separated flow, many researchers use the SWG and other attached flow transition models for attached and separated flows. These results motivated this investigation. Hence, the SWG transition model was applied for flow with a small and large separation bubble to investigate the performance of this model.

The flow conditions used in the experimental study were a Reynolds number of 0.9 Million, an inlet Mach number of 0.5, chordal incidence angles of 0° and 10°, a reduced frequency of 0.4, and an interblade phase angle of 180°. In this study, the chordal incidence angles of 1° and 7.5° were used to match the experimental data. For unsteady simulations an oscillation amplitude of 0.3° was used.

6.2   Conclusions

From the flat plate laminar flow prediction, the flow solver was able to resolve the laminar portion of transitional flow.   This solver could also resolve the flat plate fully turbulent flow with the implemented Spalart-Allmaras turbulence model and transitional flow with the combination of the SWG transition model.   The influence of transition onset location was also investigated.   For the flat plate transitional flow, Steelant and Dick predict the transition onset closer to the leading edge than Suzen et al. The SWG transition model with Suzen et al. onset model gave the best prediction to match the experimental data. With these results, the SWG transition model combined with Steelant and Dick onset model and the Suzen et al. onset model were used to perform the transition calculations on the NASA/P&W airfoil. The Steelant and Dick onset model was only used on pressure surface and calculations were not sensitive to what was happening on the pressure surface.

For the NASA/P&W airfoil steady predictions at the low incidence angle condition, the turbulent and transitional flow predictions had good correlation with the

experimental data. A small suction surface separation bubble was predicted in the leading edge region. When the experiments were conducted, flow visualization was not done because the pressure distributions did not raise any suspicion of flow separation in the leading edge region. In the separated flow region, the transition calculations deviated substantially from the turbulent calculation. The SWG transition model predicted pressure plateaus in this area. The transition onset models estimated the transition onset point to start within the predicted separation bubble. Transition onset points that were farther downstream of the separation point resulted in a longer pressure plateau and a smaller pressure coefficient for the pressure plateau. There is no experimental data available in the transition region for the low incidence angle condition, which would indicate whether the transition solutions obtained are better than the fully turbulent solution due to instrumentation limitations caused by the airfoil thickness in this area. No changes in the pressure coefficient were found on the pressure surface for changes in the suction surface transition onset point. Additionally, little change was found between the fully turbulent pressure coefficient and the SWG predicted pressure coefficient on the pressure surface.

At the high incidence angle condition, a large suction surface separation bubble was measured and the turbulent flow calculations could not capture the pressure plateau in the leading edge region where the separation started as indicated by the experimental data. Transition calculations from the SWG transition model showed that with transition onset points within the bubble, a pressure plateau formed in the leading edge region. Oscillatory solutions were obtained when the transition onset point was too deep inside the separation bubble. The SWG transition model gave solutions that had pressure plateaus smaller in length than the experimental data and had larger pressure coefficients. The SWG model show promising results in that a pressure plateau is forming but it is smaller than exhibited by the experimental data. No effort was made to change any of the modeling coefficients within the SWG model. However, the ability to

select the transition onset point for SWG transition model was used to investigate the influence of the onset point on the predicted pressure coefficient.

For the NASA/P&W airfoil unsteady predictions at the low incidence angle condition, the fully turbulent and transition results with different transition onset models correlated well with the experimental data. No significant change in the pressure coefficient on the pressure surface was observed for the change in the pressure surface transition onset location. The pressure distribution for transitional flow on the pressure surface is very similar to the fully turbulent solution. The suction peak on the suction surface pressure coefficients imaginary part moves more towards the trailing edge compared to the fully turbulent calculations. The real part of the suction surface pressure coefficients has a lower value than it is in fully turbulent flow. A small plateau was found on the work impulse near the leading edge for transitional work impulse, while it was not shown in the fully turbulent prediction.

For unsteady predictions at the high incidence angle condition, the transition results are very close to the fully turbulent solution on the pressure surface. For the suction surface imaginary part, transition predictions exhibited a small plateau in the leading edge region which was also shown in the steady results. There are only slight differences between the transition and fully turbulent calculations, which is consistent with the small changes found for steady flow. The transition work impulse magnitudes are more stable than the experimental data in the separated flow region. In the leading edge region, the transition result shows a slightly higher work impulse than the fully turbulent. In the case of highly separated flow the correlation with the unsteady data was found to be poor in the separated flow region. This might be caused by a three-dimensional effect due to the bubble, or other contributing factors such as spreading half-angle, the spot propagation parameter, and spot generation rate. The predictions had large pressure fluctuations in the separation zone that did not correlate well with the experimental data.

Overall, the calculations with SWG transition model improved the results especially for the steady flow.

As for the transition onset models tested, the Suzen et al. transition onset model gives the best results. However, note that transition onset models are need for transition length models like the SWG method. The transition onset models can influence stability. Moreover, more experimental data are needed to improve transition onset models, particularly for separated flow.

The main conclusions for this research are listed below:

1. The SWG model has weakness in performing transition calculations with highly separated flow and it is more suitable for attached flow or flow with small separation bubbles.

2. Changes in the SWG model parameters need to be investigated for separated flow to improve the predictions.

3. To improve the transition model, more detailed data on the transition process, particularly, in separation bubbles is needed.

4. The transition onset models are also critical to predict the onset location as they can influence the transition length and stability.

6.3   Future Work

In general, transition models have been developed using only a limited range of experimental data. More detailed data on the transition process particularly in separation bubbles is necessary to improve transition models. Changes in the SWG model parameters need to be investigated for separated flow to improve the predictions. The ability of the SWG transition model to predict general flow fields particularly at off-design conditions needs to be further investigated to highlight the SWG model's range of applicability and to help direct future theoretical/numerical and experimental efforts.

Further work for flow conditions where the boundary layer is massively separated from the airfoil surface needs to be done. Also, the effects of more sophisticated turbulence models and transition models need to be studied to improve the prediction. In order to improve the transition onset models for separated flow, more experimental data are also needed in the future. In general, transition models need to be extended to consider three dimensional flow.

There are still some issues that need to be addressed in the grid distortion techniques used for large oscillation amplitudes in the NPHASE solver. As for the grid generation, the H-grid used in the computation has some advantages and disadvantages. The H-grid is easier to generate, and grid topology is easy to understand. However, it does not perform well in the highly curved region, especially in the round leading edge and trailing edge part of the airfoil. Other grids type like the O-grid or C-grid should be considered in the future.

APPENDIX

A. Matrix Formation

LHS of Equation (3.38):

$$\bar{M}_\xi^1 \Delta\tilde{v} = \frac{1}{2\Delta\xi_{i,j}}\left[\left(U_{i,j} + \left|U_{i,j}\right|\right)\Delta^n\tilde{v}_{i-1,j} - 2\left|U_{i,j}\right|\Delta^n\tilde{v}_{i,j} + \left(\left|U_{i,j}\right| - U_{i,j}\right)\Delta^n\tilde{v}_{i+1,j}\right] \tag{A.1}$$

$$\bar{M}_\xi^2 \Delta\tilde{v} = \frac{1}{\mathrm{Re}_{ref}\,\sigma\Delta\xi_{i,j}}\left\{\begin{array}{l}\left[\xi_{x_{i,j}}A2(1,1) + \xi_{y_{i,j}}A2(1,2)\right]\Delta^n\tilde{v}_{i-1,j} \\ +\left[\xi_{x_{i,j}}B2(1,1) + \xi_{y_{i,j}}B2(1,2)\right]\Delta^n\tilde{v}_{i,j} \\ +\left[\xi_{x_{i,j}}C2(1,1) + \xi_{y_{i,j}}C2(1,2)\right]\Delta^n\tilde{v}_{i+1,j}\end{array}\right\} \tag{A.2}$$

$$\bar{M}_\xi^3 \Delta\tilde{v} = -\frac{c_{b2}\tilde{v}}{\mathrm{Re}_{ref}\,\sigma\Delta\xi_{i,j}}\left\{\begin{array}{l}\left[\xi_{x_{i,j}}A3(1,1) + \xi_{y_{i,j}}A3(1,2)\right]\Delta^n\tilde{v}_{i-1,j} \\ +\left[\xi_{x_{i,j}}B3(1,1) + \xi_{y_{i,j}}B3(1,2)\right]\Delta^n\tilde{v}_{i,j} \\ +\left[\xi_{x_{i,j}}C3(1,1) + \xi_{y_{i,j}}C3(1,2)\right]\Delta^n\tilde{v}_{i+1,j}\end{array}\right\} \tag{A.3}$$

$$LHS = \Delta\tilde{v}^{**} - \left(\bar{M}_\xi^1\Delta\tilde{v}^{**} + \bar{M}_\xi^2\Delta\tilde{v}^{**} + \bar{M}_\xi^3\Delta\tilde{v}^{**}\right)\Delta\tau \tag{A.4}$$

RHS of Equation (3.38):

$$\left(M_\xi^1\right)^n = \frac{1}{2\Delta\xi_{i,j}}\left[\left(U_{i,j} + \left|U_{i,j}\right|\right)\tilde{v}_{i-1,j} - 2\left|U_{i,j}\right|\tilde{v}_{i,j} + \left(\left|U_{i,j}\right| - U_{i,j}\right)\tilde{v}_{i+1,j}\right] \tag{A.5}$$

$$\left(M_\eta^1\right)^n = \frac{1}{2\Delta\eta_{i,j}}\left[\left(V_{i,j} + \left|V_{i,j}\right|\right)\tilde{v}_{i,j-1} - 2\left|V_{i,j}\right|\tilde{v}_{i,j} + \left(\left|V_{i,j}\right| - V_{i,j}\right)\tilde{v}_{i,j+1}\right] \tag{A.6}$$

$$\left(M_\xi^2\right)^n = \frac{1}{\mathrm{Re}_{ref}\,\sigma\Delta\xi_{i,j}}\left\{\begin{array}{l}\left[\xi_{x_{i,j}}A2(1,1) + \xi_{y_{i,j}}A2(1,2)\right]\tilde{v}_{i-1,j} \\ +\left[\xi_{x_{i,j}}B2(1,1) + \xi_{y_{i,j}}B2(1,2)\right]\tilde{v}_{i,j} \\ +\left[\xi_{x_{i,j}}C2(1,1) + \xi_{y_{i,j}}C2(1,2)\right]\tilde{v}_{i+1,j}\end{array}\right\} \tag{A.7}$$

$$\left(M_{\eta}^{2}\right)^{n} = \frac{1}{\mathrm{Re}_{ref}\,\sigma\Delta\eta_{i,j}}\left\{\begin{array}{l}\left[\eta_{x_{i,j}}A2(2,1)+\eta_{y_{i,j}}A2(2,2)\right]\tilde{v}_{i,j-1}\\[4pt]+\left[\eta_{x_{i,j}}B2(2,1)+\eta_{y_{i,j}}B2(2,2)\right]\tilde{v}_{i,j}\\[4pt]+\left[\eta_{x_{i,j}}C2(2,1)+\eta_{y_{i,j}}C2(2,2)\right]\tilde{v}_{i,j+1}\end{array}\right\} \qquad (A.8)$$

$$\left(M_{\xi}^{3}\right)^{n} = -\frac{c_{b2}\tilde{v}_{i,j}}{\mathrm{Re}_{ref}\,\sigma\Delta\xi_{i,j}}\left\{\begin{array}{l}\left[\xi_{x_{i,j}}A3(1,1)+\xi_{y_{i,j}}A3(1,2)\right]\tilde{v}_{i-1,j}\\[4pt]+\left[\xi_{x_{i,j}}B3(1,1)+\xi_{y_{i,j}}B3(1,2)\right]\tilde{v}_{i,j}\\[4pt]+\left[\xi_{x_{i,j}}C3(1,1)+\xi_{y_{i,j}}C3(1,2)\right]\tilde{v}_{i+1,j}\end{array}\right\} \qquad (A.9)$$

$$\left(M_{\eta}^{3}\right)^{n} = -\frac{c_{b2}\tilde{v}_{i,j}}{\mathrm{Re}_{ref}\,\sigma\Delta\xi_{i,j}}\left\{\begin{array}{l}\left[\eta_{x_{i,j}}A3(2,1)+\eta_{y_{i,j}}A3(2,2)\right]\tilde{v}_{i,j-1}\\[4pt]+\left[\eta_{x_{i,j}}B3(2,1)+\eta_{y_{i,j}}B3(2,2)\right]\tilde{v}_{i,j}\\[4pt]+\left[\eta_{x_{i,j}}C3(2,1)+\eta_{y_{i,j}}C3(2,2)\right]\tilde{v}_{i,j+1}\end{array}\right\} \qquad (A.10)$$

$$P^{n} = \left[c_{b1}\left(1-f_{t2}\right)S\tilde{v}\right]^{n} \qquad (A.11)$$

$$D^{n} = \frac{1}{\mathrm{Re}_{ref}}\left\{\frac{c_{b1}}{\kappa^{2}}\left[\left(1-f_{t2}\right)f_{v2}+f_{t2}\right]^{n}-\left(c_{w1}f_{w}\right)^{n}\right\}\left(\frac{\tilde{v}^{n}}{d}\right)^{2} \qquad (A.12)$$

$$T^{n} = \mathrm{Re}_{ref}\left(f_{t1}\Delta U^{2}\right)^{n} \qquad (A.13)$$

$$RHS = [\left(M_{\xi}^{1}\right)^{n}+\left(M_{\eta}^{1}\right)^{n}+\left(M_{\xi}^{2}\right)^{n}+\left(M_{\eta}^{2}\right)^{n}+\left(M_{\xi}^{3}\right)^{n}+\left(M_{\eta}^{3}\right)^{n}+P^{n}+D^{n}+T^{n}]\Delta\tau \qquad (A.14)$$

where the coefficients A2, B2, C2, A3, B3, C3 are:

$$A2(1,1)=\frac{\left(\psi\xi_{x}\right)_{i-\frac{1}{2},j}}{\Delta\xi_{i-\frac{1}{2},j}} \quad B2(1,1)=-\left[A2(1,1)+C2(1,1)\right] \quad C2(1,1)=\frac{\left(\psi\xi_{x}\right)_{i+\frac{1}{2},j}}{\Delta\xi_{i+\frac{1}{2},j}} \qquad (A.15)$$

$$A2(1,2)=\frac{\left(\psi\xi_{y}\right)_{i-\frac{1}{2},j}}{\Delta\xi_{i-\frac{1}{2},j}} \quad B2(1,2)=-\left[A2(1,2)+C2(1,2)\right] \quad C2(1,2)=\frac{\left(\psi\xi_{y}\right)_{i+\frac{1}{2},j}}{\Delta\xi_{i+\frac{1}{2},j}} \qquad (A.16)$$

$$A2(2,1) = \frac{\left(\psi\eta_x\right)_{i,j-\frac{1}{2}}}{\Delta\eta_{i,j-\frac{1}{2}}} \quad B2(2,1) = -\left[A2(2,1)+C2(2,1)\right] \quad C2(2,1) = \frac{\left(\psi\eta_x\right)_{i,j+\frac{1}{2}}}{\Delta\eta_{i,j+\frac{1}{2}}} \quad \text{(A.17)}$$

$$A2(2,2) = \frac{\left(\psi\eta_y\right)_{i,j-\frac{1}{2}}}{\Delta\eta_{i,j-\frac{1}{2}}} \quad B2(2,2) = -\left[A2(2,2)+C2(2,2)\right] \quad C2(2,2) = \frac{\left(\psi\eta_y\right)_{i,j+\frac{1}{2}}}{\Delta\eta_{i,j+\frac{1}{2}}} \quad \text{(A.18)}$$

$$A3(1,1) = \frac{\xi_{x_{i-\frac{1}{2},j}}}{\Delta\xi_{i-\frac{1}{2},j}} \quad B3(1,1) = -\left[A3(1,1)+C3(1,1)\right] \quad C3(1,1) = \frac{\xi_{x_{i+\frac{1}{2},j}}}{\Delta\xi_{i+\frac{1}{2},j}} \quad \text{(A.19)}$$

$$A3(1,2) = \frac{\xi_{y_{i-\frac{1}{2},j}}}{\Delta\xi_{i-\frac{1}{2},j}} \quad B3(1,2) = -\left[A3(1,2)+C3(1,2)\right] \quad C3(1,2) = \frac{\xi_{y_{i+\frac{1}{2},j}}}{\Delta\xi_{i+\frac{1}{2},j}} \quad \text{(A.20)}$$

$$A3(2,1) = \frac{\eta_{x_{i,j-\frac{1}{2}}}}{\Delta\eta_{i,j-\frac{1}{2}}} \quad B3(2,1) = -\left[A3(2,1)+C3(2,1)\right] \quad C3(2,1) = \frac{\eta_{x_{i,j+\frac{1}{2}}}}{\Delta\eta_{i,j+\frac{1}{2}}} \quad \text{(A.21)}$$

$$A3(2,2) = \frac{\eta_{y_{i,j-\frac{1}{2}}}}{\Delta\eta_{i,j-\frac{1}{2}}} \quad B3(2,2) = -\left[A3(2,2)+C3(2,2)\right] \quad C3(2,2) = \frac{\eta_{y_{i,j+\frac{1}{2}}}}{\Delta\eta_{i,j+\frac{1}{2}}} \quad \text{(A.22)}$$

where $\psi = v + \left(1+c_{b2}\right)\tilde{v}$.

BIBLIOGRAPHY

[1]Emmons, H.W., 1951, "The Laminar-Turbulent Transition in a Boundary Layer - Part I", J. of Aerospace Science, 018(7), pp. 490-498.

[2]Mitchner, M., 1954, "Propagation of Turbulence from an Instantaneous Point Disturbance," Journal of Aeronautical Sciences, Vol. 21, pp. 350-351.

[3]Schubauer, G.B. and Klebanoff, P.S., 1955, "Contribution to the Mechanism of Boundary-Layer Transition," NACA TN 3498.

[4]Tani, I. and Hama, F.R., 1953, "Some experiments on the effect of a single roughness element on boundary-layer transition," J. aero. Sci.20, 289.

[5]Hama, F. R., Long, J. D. and Hegarty, J. C., 1957, "On transition from laminar to turbulent flow," Journal of Applied Physics, 28, 388–394

[6]Narasimha, R., 1985, "The Laminar-Turbulent Transition Zone in the Boundary Layer," Progress in Aerospace Sciences, Vol. 22, pp. 22-80.

[7]Chen, K.K., and Thyson, N.A., 1971, "Extension of Emmons' Spot Theory to Flows on Blunt Bodies," AIAA Journal, Vol. 18, No. 3, pp. 490-498.

[8]Ekaterinaris, J.A., Chandrasekhara, M.S. and Platzer, M.F., 1995, "Analysis of Low Reynolds Number Airfoil Flows", Journal of Aircraft, Vol. 32, No. 3, pp. 625-630.

[9]van Dyken, R.D., Ekaterinaris, J.A., Chandrasekhara, M.S., and Platzer, M.F., 1996, "Analysis of Compressible Light Dynamic Stall Flow at Transitional Reynolds Numbers", AIAA Journal, Vol. 34, No. 7, pp. 1420-1427.

[10]Solomon, W.J., Walker, G.J. and Gostelow, J.P., 1996, "Transition Length Prediction for Flows with Rapidly Changing Pressure Gradients," ASME Journal of Turbomachinery, Vol. 118, pp. 744-751.

[11]Sanz, W. and Platzer, M.F., 1998, "On the Navier-Stokes Calculations of Separation Bubbles with a New Transition Model," ASME Journal of Turbomachinery, Vol. 120, pp. 36-42.

[12]Sanz, W., and Platzer, M.F., 1997, "On the Calculation of Laminar Separation Bubbles

Using Different Transition Models", ASME Paper 97-GT-453.

[13]Abu-Ghannam, B.J.and Shaw, R., 1980，"Natural transition of boundary layers – the effect of turbulence, pressure gradient and flow history," J. Mech. Eng. Sci. 22 (5), pp. 213–228.

[14]Mayle, R. E., 1991, "The Role of Laminar-Turbulent Transition in Gas Turbine Engines," ASME Journal of Turbomachinery, Vol. 113, pp. 509-537

[15]Calvert, W.J., 1994, "An Inviscid-Viscous Method to Model Leading Edge Separation Bubbles," ASME Paper 94-GT-247.

[16]Choi, D.H. and Kang, D.J., 1991, "Calculation of Separation Bubbles Using a Partially-Parabolized Navier-Stokes Procedure," AIAA J., Vol. 29, pp.1266-1272.

[17]Sanz, W. and Platzer, M.F., 2002, "On the Numerical Difficulties in Calculating. Laminar Separation Bubbles," ASME Paper No. GT-2002-30235.

[18]Thermann, H., Müller, M., and Niehuis, R., 2001, "Numerical Simulation of the Boundary Layer Transition in Turbomachinery Flows," ASME Paper No. 2001-GT-0475.

[19]Walker, G. J., Subroto, P. H. and Platzer, M. F., 1988, "Transition modeling effects on viscous/inviscid interaction analysis of low reynolds number airfoil flows involving laminar separation bubbles," ASME 88-GT-32.

[20]Sieger, K., Schiele, R., Kaufmann, F., Wittig, S. and Rodi, W., 1995, "A Two-Layer. Turbulence Model for the Calculation of Transitional Boundary-Layers", ERCOFTAC Bulletin, 24, pp. 21-25.

[21]Suzen, Y.B., P.G. Huang, L.S. Hultgren, and D.E. Ashpis, 2003, "Predictions of Separated and Transitional Boundary Layers Under Low-Pressure Turbine Airfoil Conditions Using an Intermittency Transport Equation," Journal of Turbomachinery, 125, No. 3, pp. 455-464.

[22]Steelant, J., and Dick, E., 1996, "Modelling of Bypass Transition With Conditioned Navier-Stokes Equations Coupled to an Intermittency Transport Equation," Int. J. Numer. Methods Fluids, 23, pp. 193–220.

[23]Cho, J. R., and Chung, M. K., 1992, "A k-ε-γ Equation Turbulence Model," J. Fluid Mech., 237, pp. 301–322.

[24]Hultgren, L. S., and Volino, R. J., 2000, "Separated and Transitional Boundary Layers Under Low-Pressure Turbine Airfoil Conditions," NASA TM, in preparation.

[25]Menter, F.R., Esch, T., and Kubacki, S., 2002, "Transition Modelling Based on Local Variables," Engineering Turbulence Modeling and Experiments, W.Rodi and N. Fueyo (Editors), Elsevier Science Ltd.

[26]Menter, F.R., Langtry, R.B., Likki, S.R., Suzen, Y.B., Huang, P.G., and Voelker, S., 2006, "A Correleation-Based Transition Model Using Local Variables," ASME Journal of Turbomachinery, Vol. 128, pp. 413-434, July.

[27]De Palma, P., 2002, "Accurate numerical simulation of compressible turbulent flows in turbomachinery," AIAA Journal, Vol. 40 No.4, pp.702-8.

[28]Langry, R.B. and Sjolander, S.A., 2002, "Prediction of Transition for Attached and Separated Shear Layers in Turbomachinery," AIAA Paper No. 2002-3641.

[29]Whitlow, D., Capece, V.R., Jones, K.D., Platzer, M.F., Navier-Stokes Computations of the Flow through the NASA GRC Transonic Flutter Cascade, AIAA 2006-4455, 2006

[30]Buffum, D.H. and Fleeter, S., 1990, "Aerodynamics of a Linear Oscillating Cascade," NASA Technical Memorandum 10350.

[31]Buffum, D.H., Capece, V.R., King, A.J. and El-Aini, Y.M., 1996, "Experimental Investigation of Unsteady Flows at Large Incidence Angles in a Linear Cascade," AIAA paper No. 96-2823.

[32]Buffum, D.H., Capece, V.R., King, A.J. and El-Aini, Y.M., 1998, "Oscillating Cascade Aerodynamics at Large Mean Incidence, " ASME Journal of Turbomachinery, Vol. 120, No. 1, pp. 122-131; also NASA TM-107247.

[33]Suzen, Y.B., and Huang, P.G., 2000, "Modeling of Flow Transition Using an Intermittency Transport Equation," Journal of Fluids Engineering, 122, 273-284.

[34]Menter, F.R., Esch, T. and Kubacki, S., "Transition Modeling Based on Local Variables," 5th International Symposium on Engineering Turbulence Modelling and Measurements, Mallaorca, Spain. 2000

[35]Schlichting, H., 1979, Boundary Layer Theory, McGraw-Hill, 7th edition.

[36]Klebanoff, P.S. and Tidstrom, K.D., Sargent, L.M., 1962, "The Three-Dimensional

Nature of Boundary Layer Instability", Journal of Fluid Mechanics, Vol. 12, pp. 1-24

[37]Malkiel, E. and Mayle, R.E., 1996, "Transition in a Separation Bubble," ASME Journalof Turbomachinery, Vol. 118, pp. 752-759.

[38]Savill, A.M., 2002, "New Strategies in Modelling By-Pass Transition," Closure Strategies for Turbulent and Transitional Flows, edited by B.E. Launder and N.D. Sandsam, Cambridge University press, pp. 464-492.

[39]Spalart, P.R., and Allmaras, S.R., 1994, "A One Equation Turbulence Model for Aerodynamic Flows," La Recherche Aerospatiale, No. 1, pp. 5-21.

[40]Gostelow, J.P., Melwani, N. and Walker, G.J., 1996, "Effects of Streamwise Pressure Gradient on Turbulent Spot Development," ASME Journal of Turbomachinery, Vol. 118, pp. 737-743.

[41]Michel, R., 1951, "Etude de la transition sur les profiles d'aile; establishement d'un critere de determination de point de transition et calcul de la trainee de profile incompressible," ONERA Rep. 1/1578A.

[42]Steelant, J. and Dick, E., 2001, "Modeling of Laminar Turbulent Transition for High Free-Stream Turbulence," Journal of Fluids Engineering, Vol. 123, pp. 22-30.

[43]Praisner, T., and Clark, J., 2004, "Predicting Transition in Turbomachinery. Part I: A review and new model development," ASME paper no. IGTI-2004-54108.

[44]Baldwin, B.S. and Lomax, H., 1978, "Thin Layer Approximation and Algebraic Model for Separated Turbulent Flows," AIAA Paper No. 78-257.

[45]Cebeci, T. and Smith, A.M.O., Analysis of Turbulent Boundary Layers, Academic Press, N.Y., 1974

[46]Chima, R.V., Giel, P.W., and Boyle, R.J. "An Algebraic Turbulence Model For Three-Dimensional Viscous Flows," NASA-TM-105931, January, 1993.

[47]Krist, S. L. and Biedron, R. T. and Rumsey, C. L., "CFL3D User's Manual (Version 5.0)," NASA TM-1998-208444, June 1998.

[48]Wilcox, D.C. (2004), Turbulence Modeling for CFD, ISBN 1-928729-10-X, 2nd Ed., DCW Industries, Inc.

[49]Swafford, T.W., Loe, D.H., Huff, D.L., Huddleston, D.H., and Reddy, T.S.R., 1994, "The Evolution of NPHASE: Euler/Navier-Stokes Computations of Unsteady Two-Dimensional Cascade Flow Fields," AIAA Paper No. AIAA-94-1834

[50]Ayer, T.C. and Verdon, J.M., 1994, "Numerical Unsteady Aerodynamic Simulation for Blade Forced Response," Report WL-TR-95-2011.

[51]White, F.M., "Viscous Fluid Flow", McGrawHill, 1991.

[52]D.B. Spalding, A single formula for the law of the wall, ASME J. Appl. Math. 28 (3) (1961) 455–458.

[53]Carta, F.O., "Aeroelasticity and Unsteady Aerodynamics," in The Aerothermodynamics of Aircraft Gas Turbine Engines, Gordon C. Oates, Editor, AFAPL-TR-78-52, pp. 22-1 – 22-54, 1978.

[54]Savill, A.M., 1993 "Some recent progress in the turbulence modeling of by-pass transition", In: R,M,C, So, C.G.Speziale and B.E.Launder, Eds.: Near-Wall Turbulent Flows, Elsevier, pp.829-848.

Qian Zhang

Date of Birth: 11/16/1975

Birthplace: Jinan, Shandong Province, P. R. China

Education

2001 M.S. in Fluid Machinery and Fluid Power Engineering

Xi'an Jiaotong University, P. R. China

1998 B.S. in Fluid Machinery and Fluid Power Engineering

Xi'an Jiaotong University, P. R. China

Scholastic and professional honors

2002 – 2008   University of Kentucky Graduate School Scholarship

1999   Excellent Graduate Student Scholarship

1999   A-level Xin Xing Company scholarship

1998   Excellence Graduation Project of Xi'an Jiaotong University

1997   Fu Sheng Company Scholarship, 1997

1996   Prof. Zhaolin Zhong Scholarship of Xi'an Jiaotong University

1995 – 1997   Excellent Undergraduate student

1995 – 1997   A-level scholarship of Xi'an Jiaotong University

Professional Positions

2009 – 2010   Research Assistant, University of Kentucky

2003 – 2008   Research Assistant and Teaching Assistant, University of Kentucky

2002 – 2003   Research Assistant, University of Kentucky

1998 – 2001   Research Assistant, Xi'an Jiaotong University

Professional Publications

Zhang, Q., Hariharan, V., and Capece, V., "Computational Investigation of a Transonic Flutter Cascade," AIAA-2008-4701, 44th AIAA/ASME/SAE/ASEE Joint Propulsion Conference & Exhibit, Hartford, CT, July 2008.

Zhang, Q., Whitlow, D., and Capece, V., "Steady Viscous Flow Solution of a Turbomachine Cascade," AIAA Paper 2004-0198, 42nd AIAA Aerospace Sciences Meeting and Exhibit, Reno, NV, January 2004.

Professional Presentations and Abstracts

Zhang, Q., and Capece, V., "Viscous Flow Calculation of a Compressor Cascade at Low Mach Number," 33rd Annual Dayton-Cincinnati Aerospace Science Symposium, Dayton, OH, March 4, 2008.

Zhang, Q., and Capece, V., "Steady and Unsteady Simulation of a Transonic Flutter Cascade," 32nd Annual Dayton-Cincinnati Aerospace Science Symposium, Dayton, OH, March 6, 2007.

Zhang, Q., and Capece, V., "Steady and Unsteady Aerodynamic Flow Simulation of a Compressor Airfoil," 31st Annual Dayton-Cincinnati Aerospace Science Symposium, Dayton, OH, March 7, 2006.

Zhang, Q., and Capece, V., "Computation of Oscillating Airfoil Unsteady Aerodynamics for Stalled and Unstalled Flow," 1st Dayton Engineering Sciences Symposium, Dayton, OH, October 31, 2005.

Zhang, Q., Whitlow, D., and Capece, V., "Computation of Compressor Airfoil Aerodynamics for Stalled and Unstalled Flow," 30th Annual Dayton-Cincinnati Aerospace Science Symposium, Dayton, OH, March 8, 2005.

Zhang, Q., Whitlow, D., and Capece, V., "Steady Flow Simulation of a Transonic Compressor Cascade," 29th Annual Dayton-Cincinnati Aerospace Science Symposium,

Dayton, OH, March 9, 2004.

Professional Activities

Member: American Institute for Aeronautics and Astronautics (AIAA).

                American Society of Mechanical Engineers (ASME)

Volunteer

Volunteer in the welcome week activities of Office of International Affair (OIA) 2004, 2005

Qian Zhang